

Integrated CFD Modelling for Nozzle Design for Fog Generation

Yankang Tian

This Thesis is submitted to the Department of Design, Manufacture and Engineering Management,
University of Strathclyde, for the degree of Doctor of Philosophy

This thesis is the result of the author's original research. It has been composed by the author and has not been previously submitted for examination which has led to the award of a degree.

The copyright of this thesis belongs to the author under the terms of the United Kingdom Copyright Acts as qualified by the University of Strathclyde Regulation 3.50. Due acknowledgement must always be made of the use of any material contained in, or derived from, this thesis.

Signed:

Date:

Acknowledgements

It has been a long journey for me to finish this PhD project. As I work all the way through to the completion of this thesis, many people have offered their supports and encouragements. Hence, I would love to take this opportunity to express my sincere gratitude to those who assisted me in various ways.

Foremost, I would like to convey my heartfelt thanks to my supervisor Professor Yi Qin. As a supportive and generous mentor, Professor Qin not only teaches all his students patiently with his immense knowledge and gives us supports and guidelines with no reservation, he also provides precious opportunities for us to get involved in domestic and European projects, which broaden our horizon by working with some world-famous companies and institutes. From him, I not only learnt the wisdom for conducting academic research, but I also learnt his selfless attitude towards contribution to knowledge.

Besides, I also want to thank Dr. Jie Zhao, Dr. Quanren Zeng, Yihui Zhao, and Dr. Wenlong Chang. As they are more experienced researchers in the Centre for Precision Manufacturing in University of Strathclyde, they gave me useful help and advices both in life and in academic study, especially at the beginning of my project when I felt clueless. I would like to thank Dr. Kunlan Huang as she often shared some inspiring thoughts on conducting high-quality research with me, which caused my interest in advanced micro forming technology. I am thankful for Dr. Senyong Chen, Dr. Hao Wu, Shuai Miao, Yihong Yang, Xinyu Yang, Mutian Li, Dr. Wenbin Zhong, Dr Yukui Cai, Bo Chen, Song Yang, Dr. Zhenhai Xu, Dr. Zhiyuan Yu, Dr. Lu Hao, Dr. Xiaoyu Liu, Dr. Wei Yao, Jingyu Xu, Hongying Jiang, Liyuan Zhuang, Ovidiu Spatacian-Tarnu, Lynn Sutherland, Roy Sutherland, Llerena Aguilar Francisco José, Martín Pérez Tania, and many others that I have met. They are helpful colleagues and

Acknowledgements

kind hearted friends. Also I would not forget the helps from Arthur Lan Kuan Yip who was a talented young man but unfortunately passed away in 2014. His dependable personality and outstanding skills in doing research has always been a role model to me.

I would like to thank my families from whom I gain unlimited supports. I want to thank my girlfriend Yanling Ye who has been standing by me persistently. Thanks to my mother Jianling Li and my father Hualin Tian for giving birth to me in the first place. Enormous appreciations are due to my mother for her constant support and understanding without which I am sure I would not made it to finish my study.

Finally I want to acknowledge the funding from the FP7 framework programme of European Commission under grant n° 312804. for the work reported in this thesis.

Abstract

Sprays, as dynamic droplet/particle clouds of functional substances, are widely used in industry, agriculture, and our daily lives. Sprays are different depending on the situations in which they are used and are characterized by pattern, capacity, impact, angle and drop size. Each application has its own requirements for spray characteristics and these requirements are demanding continuing development of atomization systems. Improvement of spraying systems which use a nozzle to convert bulk liquid into dispersed droplets requires knowledge of the atomization process. Although great effort has been dedicated to study, describe, and predict spray generation, flow evolution from continuous stream to separated droplets is still beyond full understanding. What is more, internal nozzle flow and initial breakup that decide the characteristics of far-field spray take place inside enclosed injector, this makes it challenging for non-invasive measurement.

At the beginning of this study, available nozzle designs and their performances, and commonly used approaches for modelling fluid flows were reviewed. It is emphasised that there is currently a lack of detailed design principles for sprays with a fine droplet and high flow rate, this type has a great potential for wide application. However, this remains a challenge for advanced nozzle design. To overcome difficulties in the nozzle design, a development workflow is planned in detail. Requirement-oriented nozzle optimization and an integrated CFD model establishment are two closely related components in this study. Numerical results help the justification and dimension selection for nozzle design while physical tests on the nozzle help to validate the CFD model. Architecture for integrated CFD modelling is discussed including the steps for bridging the knowledge gap between different numerical theories.

CFD-aided advanced nozzle design and optimization actions are conducted. With parametric modelling a large number of nozzle dimensions can be tested numerically, this largely reduces the development cycle and cost compared to real part fabrication and physical testing. The first detailed design of a nozzle is achieved based on the results from CFD modelling.

The designed nozzle was fabricated and then tested in a fog dynamic lab. The results of flow rates, spray angles, and droplet sizes were recorded. These results are used to validate the proposed integrated CFD model.

Design of the nozzle was improved by requirement-driven optimization. Virtual testing based on valid integrated CFD modelling is used to study the optimized nozzle design.

As an important achievement of this study, a multi-fluid fogging nozzle was designed. Numerical evaluation using integrated CFD modelling shown that the nozzle could generate sprays with flow rate up to 0.53 L/s and droplets ranging mostly from 2 μm to 5 μm . The designed nozzle was manufactured and tested in laboratory in Spain. Data obtained from experiments successfully validates the performance predicted by simulations. Being capable to generate spray with high flow rate and fine droplets, this multi-fluid nozzle design shows its strong potential for fogging applications such as firefighting, pest management, and dust suppression.

Research Output

Publications:

1. Y. Tian, L. Wang, G. Anyasodor, & Y. Qin, (2018), “Numerical study of the induction heating of aluminium sheets for hot stamping” Paper presented at The 5th International Conference On New Forming Technology, Bremen, Germany.
2. Q. Zeng, Y. Tian, Z. Xu, & Y. Qin, (2018), “Simulation of thermal behaviours and powder flow for direct laser metal deposition process”, Paper presented at The 5th International Conference On New Forming Technology, Bremen, Germany.
3. Q. Zeng, Y. Qin, & Y. Tian (2018), “Modelling of powders dynamics for 3D printing of metal powders deposition”, Abstract from Strathwide 2018, Glasgow, United Kingdom.
4. Y. Tian, Y. Zhao, D. Melville, & Y. Qin, “Numerical study on nozzle-field cooling of heated aluminium blanks for hot-stamping”. *Procedia Manuf.* 15, 1134–1141 (2018).
5. Q. Zeng, Y. Tian, Y. Qin, J. Lee, & D. Balint, (Accepted/In press), “On the modelling of powder flow, material addition and thermal behaviours in LENS process.” Abstract from 8th EASN-CEAS International Workshop on Manufacturing for Growth & Innovation, Glasgow, United Kingdom.
6. Q. Zeng, Y. Tian, Z. Xu and Y. QIN, “Numerical modelling of the gas-powder flow during the laser metal deposition for additive manufacturing”, accepted for publication in the *Proc. of ICMR2017*, Sept. 2017, Greenwich, UK.
7. Q. Zeng, Z. Xu, Y. Tian and Y. Qin, “Advancement in additive manufacturing and numerical modelling considerations of direct energy deposition process”,

- Proc. of the 14th ICMR, pp. 104-109, 2016, <http://dx.doi.org/10.3233/978-1-61499-668-2-104>.
8. Q. Zeng, Z. Xu, Y. Tian and Y. Qin, “Thermal behaviors simulation for laser metal deposition of TiAl powders” Abstract from EuroMAT 2017, Thessaloniki , Greece.
 9. X. Wang, Y. Qin, J. Li, Y. Tian, & Z. Yang, “Static contact statuses between conical silos and granular materials and its influential factors”, Nongye Gongcheng Xuebao/Transactions of the Chinese Society of Agricultural Engineering, 31(16), 65-70, 2015, DOI: 10.11975/j.issn.1002-6819.2015.16.010

European Patent:

Title: ATOMIZING NOZZLE, Applicant: Universidad de Alcalá de Henares et al., Application number: EP17382233.9, Designation of inventors: PÉREZ DÍAZ Mr. José Luis, QUIÑONES DÍEZ Mr. Javier, QIN Mr. Yi, TIAN Mr. Yankang, HORNIG Mr. Wolfgang.

Contents

Acknowledgements	i
Abstract	iii
Research Output	v
Contents	vii
List of Figures	xi
List of Tables	xv
Nomenclature	xvii
Chapter 1 Introduction	1
1.1 Background.....	1
1.2 Aims and Objectives	2
1.3 Methodology.....	3
1.4 Structure of the Thesis	4
Chapter 2 Literature Review	6
2.1 Nozzle Design.....	6
2.1.1 Spray Characteristics	6
2.1.2 Classification of Atomizers.....	10
2.1.3 Patent Review.....	16
2.1.4 Design Review	18
2.2 Challenges in Advanced Nozzle Design	23

2.3 Nozzle Design Procedures.....	25
2.4 Summary	27
Chapter 3 CFD Modelling of Multi-Phase Atomization	29
3.1 Basics of Computational Fluid Dynamics (CFD).....	29
3.2 Models for Turbulent Fluctuation.....	31
3.2.1 $k - \epsilon$ Model	31
3.2.2 $k - \omega$ Model	35
3.2.3 Large Eddy Simulation (LES) Model.....	37
3.3 Models for Multiphase Fluid Flow	38
3.3.1 Volume of Fluid (VOF) Model	39
3.3.2 Mixture Model.....	40
3.3.3 Eulerian Multiphase Model.....	42
3.3.4 Discrete Phase Model (DPM)	43
3.4 Models for Droplet Breakup, Collision, and Coalescence	44
3.4.1 Models for Droplet Breakup	44
3.4.2 Models for Collision and Droplet Coalescence.....	51
3.5 Summary of CFD Models and Challenges for Modelling Atomization	52
Chapter 4 CFD-Aided Nozzle Development	61
4.1 Research Development Workflow	61
4.2 Requirements for the Nozzle Design	63
4.3 Architecture of CFD Model.....	64
4.4 Summary	69
Chapter 5 Design of Multi-Fluids Atomizer	71
5.1 Nozzle Design Concepts	71
5.2 Numerical Evaluation of Nozzle Concepts	74
5.3 Results of Concept Evaluation	78
5.3.1 Concept A	78

5.3.2 Concept B.....	81
5.3.3 Concept C.....	83
5.3.4 Concept D	85
5.3.5 Concept E.....	87
5.3.6 Concept F.....	89
5.4 Initial Nozzle Design	93
5.5 Development of Third-Component Mixing Concept.....	94
5.6 Numerical Optimization of Design Dimensions.....	98
5.7 Numerical Investigation of Nozzle Size Effect	107
5.8 Summary	109
Chapter 6 Atomization Tests and Model Validation	111
6.1 Detailed Design of the Atomizer	111
6.1.1 Design for Manufacturing and Assembly	111
6.1.2 Manufacturing of Nozzle Components.....	115
6.1.3 Redesign of Nozzle Components	116
6.2 Spray Dynamic Experiments of Atomizer	119
6.2.1 Experimental Setup.....	119
6.2.2 Experimental Investigation	121
6.3 CFD Model Validation and Error Analysis.....	126
6.4 Summary	132
Chapter 7 Design Optimization and Virtual Testing	134
7.1 Nozzle Design Optimization	134
7.2 Virtual Testing of Optimized Nozzle Design.....	137
7.3 Summary	140
Chapter 8 Conclusions and Future Work	141
8.1 Conclusions	141
8.2 Summary of Contributions to Knowledge.....	143

8.2.1 CFD Models for Multiphase Atomization	143
8.2.2 Nozzle Design and Design Approach.....	144
8.3 Future Work.....	144
8.3.1 To Improve the Optimization Approach.....	144
8.3.2 To Optimize the Third Component Mixing Concept	145
8.3.3 To Reduce the Nozzle Components	145
References	146
Appendix	155
Appendix A - Additional Results from Product Review	155
Appendix B - Experimental Data for Particle Distribution.....	158

List of Figures

Figure 1.1 Structural map of this thesis.....	5
Figure 2.1 Spray patterns.....	8
Figure 2.2 Relation between spray angle and theoretical coverage.....	9
Figure 2.3 Classification of different nozzles based on atomizing mechanisms.....	11
Figure 2.4 Configurations of different hydraulic nozzle designs.....	12
Figure 2.5 Configurations of different twin-fluid nozzle designs.....	14
Figure 2.6 Flow rates produced by various nozzles with different water pressure.....	20
Figure 2.7 Mean droplet sizes produced by single fluid axial full cone nozzle with different flow rates.....	21
Figure 2.8 Mean droplet sizes produced by twin fluid full cone nozzle with different flow rates.....	22
Figure 2.9 Performance of single fluid nozzle and twin fluid nozzle.....	23
Figure 2.10 Effect of droplet size for trapping particles.....	24
Figure 4.1 Workflow for developments of advance nozzle design and CFD model.....	62
Figure 4.2 General requirements for the spray generated by the designed nozzle.....	64
Figure 4.3 Numerical architecture of the proposed CFD model for studying the atomization process.....	66
Figure 5.1 Selected nozzle configurations.....	73
Figure 5.2 (a) 3D geometry and boundary conditions for Concept A. (b) Mesh for simulation of concept A.....	75
Figure 5.3 Numerical results of concept A: (a) volumetric distribution of water and streamlines of air velocity; (b) tracking of water droplets and their SMD values; (c) spatial distribution of droplet number and	

mean droplet size; (d) histogram presenting diameter of droplets exiting the outlet of calculation domains.	79
Figure 5.4 Numerical results of concept B: (a) volumetric distribution of water and streamlines of air velocity; (b) tracking of water droplets and their SMD values; (c) spatial distribution of water droplet number and mean droplet size; (d) histogram presenting diameter of droplets exiting the outlet of calculation domains.	82
Figure 5.5 Numerical results of concept C: (a) volumetric distribution of water and streamlines of air velocity; (b) tracking of water droplets and their SMD values; (c) spatial distribution of water droplet number and mean droplet size; (d) histogram presenting diameter of droplets exiting the outlet of calculation domains.	84
Figure 5.6 Numerical results of concept D: (a) volumetric distribution of water and streamlines of air velocity; (b) tracking of water droplets and their SMD values; (c) spatial distribution of water droplet number and mean droplet size; (d) histogram presenting diameter of droplets exiting the outlet of calculation domains.	86
Figure 5.7 Numerical results of concept E: (a) volumetric distribution of water and streamlines of air velocity; (b) tracking of water droplets and their SMD values; (c) spatial distribution of water droplet number and mean droplet size; (d) histogram presenting diameter of droplets exiting the outlet of calculation domains.	88
Figure 5.8 Numerical results of concept F: (a) volumetric distribution of water and streamlines of air velocity; (b) tracking of water droplets and their SMD values; (c) spatial distribution of water droplet number and mean droplet size; (d) histogram presenting diameter of droplets exiting the outlet of calculation domains.	90
Figure 5.9 Modularisation of the initial nozzle design.....	93
Figure 5.10 Exploded view of the initial nozzle design	94
Figure 5.11 Third-component mixing concepts.....	95
Figure 5.12 Modular nozzle designs with third - component mixing concepts.....	96
Figure 5.13 Numerical results of CFD simulations for different third-component mixing concepts.....	98
Figure 5.14 Modular nozzle design with third-component mixing concept.....	98

Figure 5.15 Design Parameters (DPs) projected on internal volume of nozzle assembly	101
Figure 5.16 The numerical results of the parametric study	105
Figure 5.17 Numerical results of design with optimized parameter: (a) volumetric distribution of water and streamlines of air velocity; (b) tracking of water droplets and their SMD values; (c) spatial distribution of water droplet number and mean droplet size; (d) histogram presenting diameter of droplets exiting the outlet of calculation domains.	106
Figure 5.18 Numerical results of half size nozzle: (a) volumetric distribution of water and streamlines of air velocity; (b) tracking of water droplets and their SMD values; (c) spatial distribution of water droplet number and mean droplet size; (d) histogram presenting diameter of droplets exiting the outlet of calculation domains.	108
Figure 5.19 Detail design of multi-fluid atomization nozzle.....	109
Figure 6.1 Static axial internal pressure design of O – Ring [84].....	112
Figure 6.2 Selections of static axial seals and radial seals in the nozzle design	113
Figure 6.3 Manufacture of swirl insert and nozzle insert.....	115
Figure 6.4 Problems occurred when producing nozzle components.....	116
Figure 6.5 Updates of sealing mechanism and housing design in the nozzle design	117
Figure 6.6 Design modification made on nozzle insert.....	118
Figure 6.7 Assembly of the designed nozzle	118
Figure 6.8 (a) Image inside the main test room for atomization experiments; (b) auxiliary equipment for supporting fog dynamic experiments in the second container	119
Figure 6.9 Graph showing the relationship between water pressure and water flowrate at different air pressures	123
Figure 6.10 Histograms for particle distributions	126
Figure 6.11 Direct comparison between experimental and numerical results of water flowrates	128
Figure 6.12 Direct comparison between experimental and numerical results of spray angles	129
Figure 6.13 Histogram for numerical results of droplet distributions.....	131

Figure 7.1 Structural Analysis of the Original Nozzle	135
Figure 7.2 Internal structure of the optimized nozzle design	136
Figure 7.3 Redesign of the swirl insert.....	137
Figure 7.4 Numerical results of optimized nozzle: (a) volumetric distribution of water and streamlines of air velocity; (b) tracking of water droplets and their SMD values; (c) spatial distribution of water droplet number and mean droplet size; (d) histogram presenting diameter of droplets exiting the outlet of calculation domains	138
Figure 7.5 Performance of optimized nozzle in the map of flow rate vs droplet size	139
Appendix A.1 Nozzle data collected from manufacture's websites	155
Appendix A.2 Mean droplet sizes produced by single fluid axial hollow cone nozzle with different flow rates	156
Appendix A.3 Mean droplet sizes produced by single fluid tangential full cone nozzle with different flow rates	156
Appendix A.4 Mean droplet sizes produced by single fluid tangential hollow cone nozzle with different flow rates	157
Appendix A.5 Mean droplet sizes produced by twin fluid hollow cone nozzle with different flow rates	157

List of Tables

Table 2-1 Review of nozzle-related patents	17
Table 2-2 List of reviewed nozzle designs	19
Table 3-1 Models for Turbulent Fluctuation	54
Table 3-2 Models for Multiphase Fluid Flow	56
Table 3-3 Models for Droplet Breakup, Collision, and Coalescence.....	58
Table 5-1 CFD models and boundary conditions for numerical evaluation of nozzle concepts.....	76
Table 5-2 Material properties of air and water	77
Table 5-3 Statistics information of spray generated by Concept A	80
Table 5-4 The distribution of pressure and velocity at the interface for the two models	80
Table 5-5 Statistics information of spray generated by Concept B	83
Table 5-6 Statistics information of spray generated by Concept C	85
Table 5-7 Statistics information of spray generated by Concept D	87
Table 5-8 Statistics information of spray generated by Concept E.....	89
Table 5-9 Statistics information of spray generated by Concept F.....	91
Table 5-10 Summary of numerical results from different design concepts	91
Table 5-11 Evaluation table of nozzle design concepts	92
Table 5-12 Design parameters of different nozzle components	99
Table 5-13 List of Design Parameters (DPs) and their design points	102
Table 5-14 List of numerical results studying the effect of design parameters on nozzle performance	103
Table 5-15 Optimized parameters for nozzle design	105
Table 5-16 Statistics information of spray generated by design with optimized parameter	107

Table 5-17 Statistics information of spray generated by half size nozzle	108
Table 6-1 Material selection for different nozzle components	114
Table 6-2 Flow rates of water generated at different combinations of operating pressures	122
Table 6-3 Graphical records for spray angles	123
Table 6-4 Results of particle distributions	125
Table 6-5 Flow rate predicted by proposed simulation system	127
Table 6-6 Numerical results of spray angles	128
Table 6-7 Numerical results of droplet distribution	130
Table 7-1 Statistics information of spray generated by optimized nozzle design	139

Nomenclature

A_0, A_s	Model constants in realizable $k - \epsilon$ model	C_d	Constant for TAB model
A_i	Area of the i th face composing the coupling plane	C_k	Constant for TAB model
B	Breakup constant	C_s	Theoretical coverage of spray
B_o	Constant for wave model	C_v	Constant for solving turbulent viscosity
b	Offset of centre of collector droplet	C_τ	Rayleigh-Taylor breakup time constant
b_{crit}	Critical offset of centre of collector droplet	C_μ	Constant relating to turbulent viscosity μ_t
C_2	Constant for solving turbulence kinetic energy	c_l	Mass fraction of phase l
C_{1w}, C_{2w}	Integration constant	D	Fluid domain
$C_{1\epsilon}$	Constant for solving turbulence dissipation rate ϵ	d	Damping coefficient for TAB model
$C_{2\epsilon}$	Constant for solving turbulence dissipation rate ϵ	D_{30}	Volume mean diameter of droplets
$C_{3\epsilon}$	Constant for solving turbulence dissipation rate ϵ	D_{32}	Sauter mean diameter of droplets
C_F	Constant for TAB model	D_i	Representative diameter of sampled droplets
C_L	Levich constant	D_{10}	Arithmetic mean diameter of droplets

Nomenclature

D_s	Spray distance	\vec{g}	Gravitational acceleration
D_{10}	Arithmetic mean diameter of droplets	I	Unit tensor
D_s	Spray distance	I_0, I_1	Modified Bessel functions of the first kind
d_0	Reference nozzle diameter	K	Ratio of the total energy in distortion and oscillation to the energy in the fundamental mode
d_p	Particle diameter	K_0, K_1	Modified Bessel functions of the second kind
E_{child}	Energy of child droplets	K_{ln}	Interphase momentum exchange coefficient
E_{parent}	Energy of the parent droplet	K_{RT}	Wave number
F	Blending function in SST $k - \omega$ model	k	Turbulent kinetic energy
\vec{F}	External body force	k_w	Wave number
F_d	Force coefficient for TAB model	k_d	Spring constant coefficient for TAB model
f_n	The n^{th} fluid's volume fraction in a cell of interest	L	Length of the modelled liquid core
G	Filter function	M	Total mass flow rate of water
G_b	Turbulence kinetic energy due to buoyancy	M_i	Mass flow on the i th face composing the coupling plane
G_k	Turbulent kinetic energy due to mean velocity gradients	\dot{m}	Mass transfer
G_ω	Generation of ω	m	Mass of particle
g_t	Acceleration of droplet in its travelling direction	N_i	Number of sampled droplets

n	Exponent related to the nozzle design for spray capacity calculation	S_m	Mass source in the continuity equation
\bar{n}	Mean expected number of collisions of collector	S_ϵ	User-defined source terms for ϵ
n_s	Number of collisions between a collector and other droplets	S_ω	User-defined source terms for ω
Oh	Ohnesorge number	Ta	Taylor number
P	Spraying pressure	T	Absolute temperature
p_{gauge}	Facet-averaged value of gauge pressure	t_{bu}	Droplet breakup time
p_{i1}, p_{i2}	Gauge pressures of cells connected by the same face	u_1	Axial perturbation velocity for liquid
p	Static pressure	u_{rel}	Relative velocity
Q	Spray flow rate	\vec{u}	Fluid phase velocity
R	Universal gas constant	\vec{u}_p	Particle velocity
Re	Relative Reynolds number	\vec{u}_i	Water velocity on the i th face composing the coupling plane
\vec{R}_{ln}	Interaction force between phases	V	Volume of ideal gas
R_k	Constant for solving turbulent viscosity	v_1	Radial perturbation velocity for liquid
r	Radius of droplet at its undisturbed position	\vec{v}	Velocity vector
r_{32}	Sauter mean radius	$\vec{v}_{dr,l}$	Drift velocity for the secondary phase l
r_c	Critical radius	\vec{v}_{ln}	Interphases velocity
S	Strain rate magnitude	\vec{v}_m	Mass-averaged velocity
S_k	User-defined source terms for k	\vec{v}_s	Velocity of secondary phase

Nomenclature

\vec{v}_p	Velocity of primary phase	a	Radius of liquid jet
We	Droplet Weber number	α_k	Effective Prandtl number for k
We_{cr}	Critical Weber number	α_s	Spray angle
x	Displacement of the droplet equator from its spherical (undisturbed) position	α_ϵ	Effective Prandtl number for ϵ
Y_k	Dissipation of k	α^*	Coefficient for low-Reynolds-number correction
Y_M	Contribution of the fluctuating dilatation	β	Constant for RNG model
Y_ω	Dissipation of ω	Γ_k	Effective diffusivity of k
Y	A random number between 0 and 1	Γ_ω	effective diffusivity of ω
		η	Arbitrary axisymmetric surface displacement
		η_0	Constant for RNG model
		μ	Molecular viscosity
		μ_l	Droplet viscosity
		μ_t	Turbulent viscosity
		μ_{eff}	Effective viscosity
		ρ	Density of fluid
		ρ_g	densities for gas
		ρ_l	densities for liquid
		ρ_m	densities for mixture
		ρ_p	densities for particle
		σ	Droplet surface tension
		σ_k	Turbulent Prandtl number for k
		σ_l	Liquid surface tension
		σ_{ij}	Stress tensor due to molecular viscosity

σ_ϵ	turbulent Prandtl number for ϵ
τ_{RT}	Breakup time
τ_r	Particle relaxation time
τ_{ij}	Subgrid-scale stress
$\bar{\tau}$	Stress tensor
ϕ_1	Velocity potential
$\bar{\phi}$	Filtered variable
ψ_1	Stream function
Ω	Maximum growth rate
$\overline{\Omega_{ij}}$	Mean rate-of-rotation tensor
Ω_{RT}	Frequency of the fastest growing wave
ω	Specific dissipation
ω_d	Droplet oscillation frequency
ω_k	Angular velocity
ω_w	Growth rate
Λ	Wavelength
$\langle \xi \rangle$	User-specified parameter
ϵ	Turbulence dissipation rate

Chapter 1

Introduction

1.1 Background

The study of multiphase atomization involving internal flow and mixture, initial breakup, and far-field spray remains one of the biggest problems in fluid mechanics. Different kinds of atomization processes are frequently used in various aspects of production activities and our daily lives. Cleaning, coating, cooling and substance distributing are some of the typical applications of sprays. New requirements for sprays with higher flow rate, smaller droplet size, or wider spray angle have emerged as technology develops, which induces continuous interest to both academic researchers and practising engineers. In order to overcome challenges in advanced nozzle design, various investigations have been conducted to study the mass transfer process from bulk liquid jet to small droplets. However, the liquid-gas dispersion flow is still not fully understood since factors such as turbulence, multiphase interaction, flow oscillation, and large fluid deformation strongly influence the flow of fluid thus making this problem highly complex.

Computational fluid dynamics (CFD) is a practical method for describing jet disintegration [1]–[3]. To describe multiphase interaction and atomization, two main kinds of mathematical framework have been formulated, namely Eulerian-Lagrangian and Eulerian-Eulerian. The Eulerian-Eulerian method treats phases as different continua [4]. This method has been used to study multiphase interactions and movements in a wide range of flow regimes. It is competent for modelling internal

nozzle flow and, in some cases, initial droplet breakup. However, far-field droplet dynamics is beyond the modelling capacity of this method since it is only valid when dispersed-phase volume fractions exceed 10 % [5]. Volume fraction represents the ratio of volume occupied by secondary phase to the volume of the computational grid cell. In the Discrete Phase Method (DPM) which is based on a Eulerian-Lagrangian framework, particle-particle and particle-continuum behaviour is calculated by solving the standard Eulerian Navier-Stokes equations for the continuous phase and trajectory tracking for the discrete phase [6], [7]. However, the discrete phase formulation assumes that the particle/droplet is present at a very low volume fraction which is usually less than 10-12 %. In this case, the model is not suitable for studying dense particle distribution at initial atomization or internal flow where the volume fraction of the discrete phase is significantly higher than 12%.

The challenges in this research lie in understanding the multiphase interaction inside the nozzle body and then improve the nozzle performances in producing fine droplets at high flow rate by optimizing the nozzle design. The strong interaction between air and water happens inside an enclosed nozzle body, which makes it impossible to conduct non-invasive measurement. The conventional nozzle design method requires repeated experiments until the empirical formula can be established for correlating the nozzle performances with the design parameters. This method is time-consuming and costly. The CFD modelling method provides an effective tool for studying nozzle internal flow and external droplet movement. However, as it was previously presented, there is a big difference between the two multiphase-flow theories and it remains a challenging topic for modelling the whole atomization process which considers the effect of nozzle internal geometry on the characteristics of generated spray.

1.2 Aims and Objectives

The primary aim of this study is to overcome challenges in advanced nozzle design for the spray of small droplets at high flow rates based on computational fluid dynamics and fog dynamic experiments. It also aims to establish a modelling system for simulating the whole spraying process by bridging the gap between different numerical theories.

In order to achieve final goal of the study, the following objectives are defined:

1. To establish a CFD modelling system for studying far-field spray dynamics affected by internal nozzle flow and initial breakup;
2. To perform CFD-aided nozzle design investigation and optimization targeting sprays with a high flow rate and small droplet size;
3. To conduct experiments on a developed nozzle design and record flow rates, spray angles, and droplet distributions of sprays generated at different pressures;
4. To compare results obtained by experiments and numerical modelling and validate and improve the established CFD modelling system;
5. To optimise the nozzle design by analysis of the nozzle internal flow and verify the new design through validated virtual testing.

1.3 Methodology

In order to achieve the final goals and objectives of this study, the following methodology was used:

- a) **Review on nozzle designs** focusing on different nozzle configurations, characteristics of generated sprays, and challenges for improving nozzle design;
- b) **Study of the CFD modelling method** for multiphase atomization especially on theories and drawbacks for turbulence, multiphase flow, and droplet dynamics;
- c) **CFD-aided nozzle development** with concept generation and justification, dimension selection, and nozzle size effects investigation;
- d) **Experiments on nozzle design and model validation** including measurement of spray characteristics and comparisons between numerical and experimental results;
- e) **Requirement-driven design optimization and virtual testing** that optimise nozzle design by analysing internal flows based on CFD simulation and testing the optimized nozzle using the validated modelling system;
- f) **Drawing conclusions** from the research and making recommendations for future work.

1.4 Structure of the Thesis

This thesis has eight chapters. Figure 1.1 shows the main chapters in this thesis and their dependences. Chapters in this thesis are organised as follows:

Chapter 1 introduces the background, aim, objectives and structure of the research.

Chapter 2 presents results from the literature review including parameters for spray characterization and atomization technology. This is followed by a patent review focusing on the most advanced nozzle designs and a design review in which commonly used nozzles are studied and depicted. After concluding nozzle performance regarding flow rate and droplet size, challenges for advanced nozzle design are revealed. Finally a procedure for designing nozzles is described.

Chapter 3 shows CFD modelling technologies for studying multiphase atomization. Fundamentals of Computational Fluid Dynamics are introduced. This is followed by descriptions of different algorithms for simulating turbulence, multiphase interaction, and droplet dynamics. Theories behind models are studied so that advantages and limitations can be concluded. This is extremely useful for recognizing challenges in CFD calculations.

Chapter 4 illustrates the development of the workflow for advanced nozzle design and the CFD modelling method. It shows the relationship between the steps and the final goals of the study. Requirements for the advanced nozzle design are also specified in this chapter together with the introduction of an architecture for the CFD modelling system.

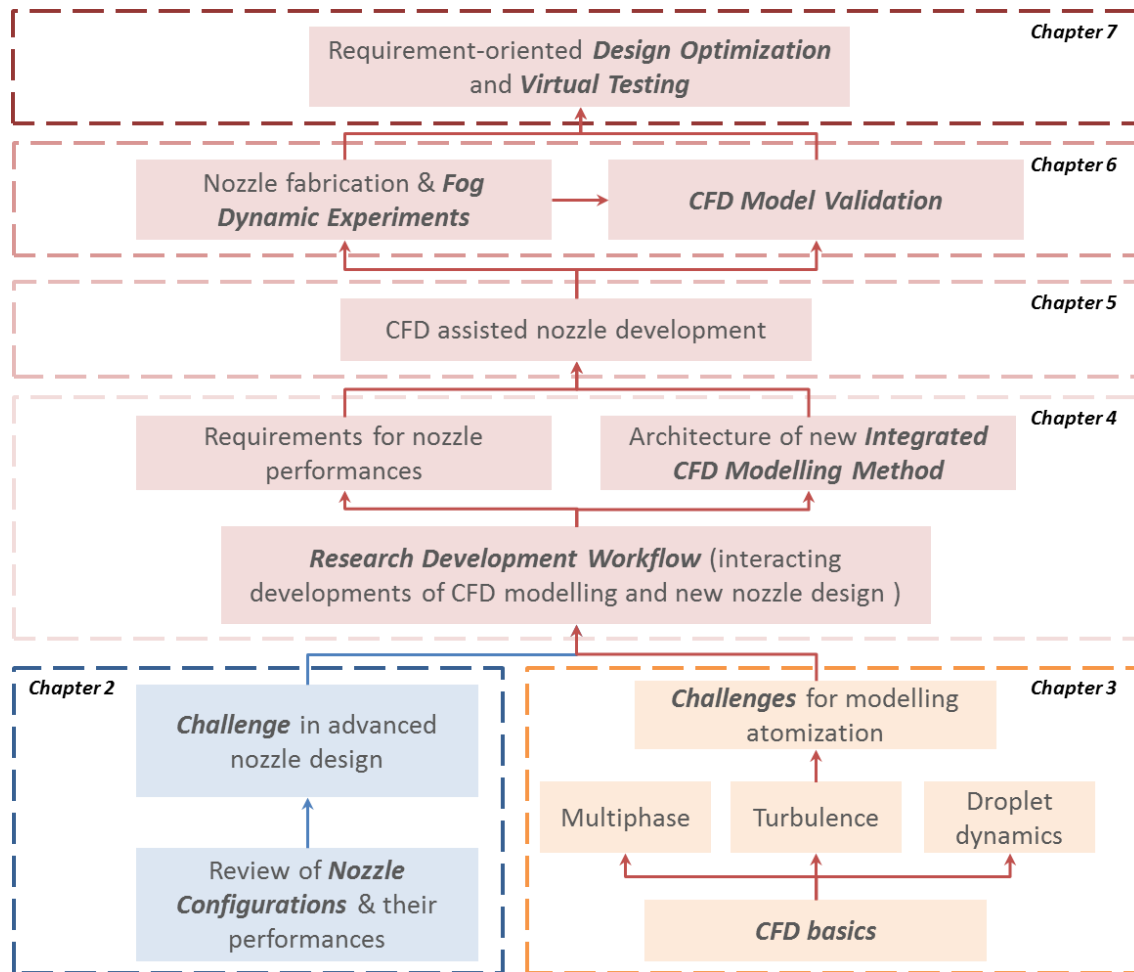


Figure 1.1 Structural map of this thesis

Chapter 5 details the step-by-step design development process with the aids of the CFD modelling system.

Chapter 6 presents the detail design of nozzle components for assembly and sealing, experiments on the manufactured nozzle with different operating pressures, and model validation by comparing numerical results to experiments.

Chapter 7 describes the requirement driven design optimization after a structural analysis on internal flow-field conditions. The nozzle is optimized for better flow rate performance. The improved nozzle design is virtually tested by using the proposed CFD modelling system.

Chapter 8 concludes the work by describing the achievements of the project and considers possible future work.

Chapter 2

Literature Review

This chapter presents the results of the literature review regarding nozzle designs and their performance. The main information gathered here includes:

- **Spray characteristics** such as spray pattern, capacity, spray impact, spray angle, and droplet size, these are used to define the nozzle performance. .
- **Categorization of nozzles** based on mechanisms for converting bulk fluid into small droplets.
- **Patent review and design review** based on gathered information on nozzle designs and their performances.
- **Challenges in advanced nozzle design** based on the gap between requirements specified by fog applications and the performance of existing nozzle design.
- **Nozzle design procedure** which shows the connection between advanced nozzle design and CFD modelling techniques.

2.1 Nozzle Design

2.1.1 Spray Characteristics

A spray is defined as a dynamic droplet cloud penetrating the surrounding medium [8]–[10]. It is usually a spray nozzle or atomizer that converts the bulk liquid into dispersed droplets. The spray nozzles with different features have wide applications in different areas including diesel engineering, agricultural irrigation, food industry and ink-jet printing. Atomisers can be seen as having three main purposes: to enlarge the

contact surface between a liquid and the surrounding medium, to apply impact force on a target, and to spread liquid over an area. Different applications require different characteristics for the produced spray. Spray pattern, capacity, spray impact, spray angle along with coverage, mean droplet size and droplet distribution are the overall characteristics of a spray [8], [9].

Spray Pattern is also described as the spatial shape of the droplet cloud existing in its surrounding environment. It is an important attribute determining the atomizer performance and spray applications [8]. There are 5 main types of spray patterns, these are solid stream, hollow cone, full cone, flat spray and multiple plume spray. Figure 2.1 shows the appearances of different spray patterns and the ideal cross-sectional shapes of them.

Full cone spray and hollow cone spray are the most commonly used spray patterns in industry [9], [11]. Full cone sprays feature uniform droplet distributions in a round, oval or square shaped area while hollow cone sprays distribute the droplets as circular rings and have good atomization of liquid at low pressure[11]. Typical applications utilising these two kinds of sprays include chemical reactors, cooling, dust control and washing.

Flat fan sprays are usually achieved by adopting special orifice designs in nozzles. Orifices featured elliptical or round exits and external V-shaped grooves produce triangular sprays with rectangular or elliptical cross-sections [9], [11]. Discharge angles of the triangular sprays are determined mainly by orifice designs and operating conditions [9]. This kind of sprays has some unique applications such as cleaning with no overlap in spray area.

Solid stream sprays are a kind of sprays that can apply high impact on the targeting area. Cleaning or water jet cutting are usually facilitated by the great pressure produced by these types of sprays. Multiple plume sprays are produced by a single nozzle with multiple orifices. They are useful in automotive injectors.

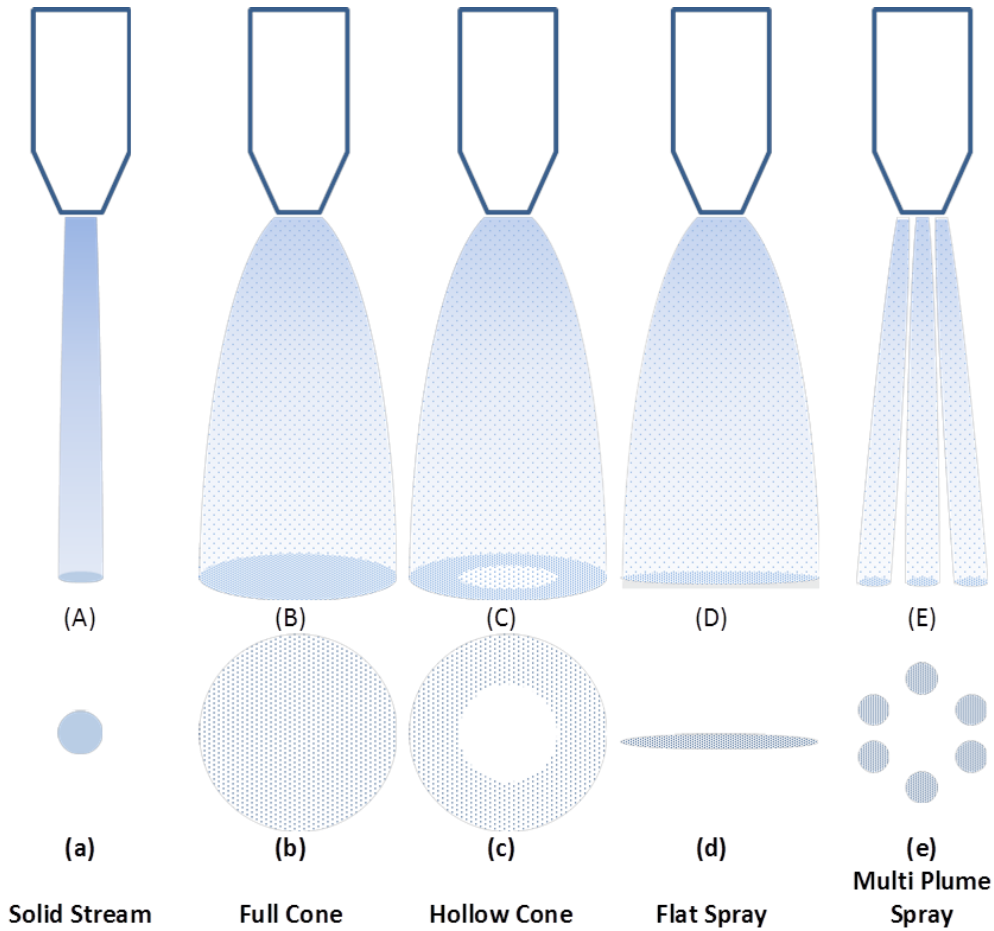


Figure 2.1 Spray patterns

Capacity represents the volume or mass weight discharged from the spray in a specific period of time. This property is affected by the internal designs of nozzles and the spraying pressure. The relationship between flow rate and pressure is [12]:

$$\frac{Q_1}{Q_2} = \frac{(P_1)^n}{(P_2)^n} \quad (1)$$

where Q is the flow rate (capacity), P represents liquid pressure and n is an exponent related to the nozzle design.

Spray Impact indicates the pressure of a spray applied to its target surface [11]. It depends on the volumetric flow rate, pressure drop, nozzle design and the distance between the nozzle and the target surface. As mention above, solid stream sprays have high spray impacts on surface. Impacts of sprays can be measured by using force sensors [8].

Spray Angle and Coverage is another important characteristic of sprays especially for applications like coating where over-spraying of coated materials should be avoided. The relationship between spray angle α_s and theoretical coverage C_s is shown in

Figure 2.2. Assuming the spray angle remains unchanged along the spray distance, this relationship can be formulated as equation (2) where D_s is the spray distance. It can be easily seen that the theoretical coverage area increases with increasing spray distance. However, in practice, spray angle collapses as the spray distance increases. This is because the velocity of droplets is slowed down by the drag force induced by the surrounding stagnating air. It is also very difficult to accurately define and measure the spray angle since sprays usually have curved and unclear edges [8]. Goniometers, needle probes equipped with linear displacement transducers and projectors for back-lighting spray images are typical technologies for quick inspections of spray angles. Discharge angles of sprays are closely related to nozzle capacities, spraying pressures and liquid properties.

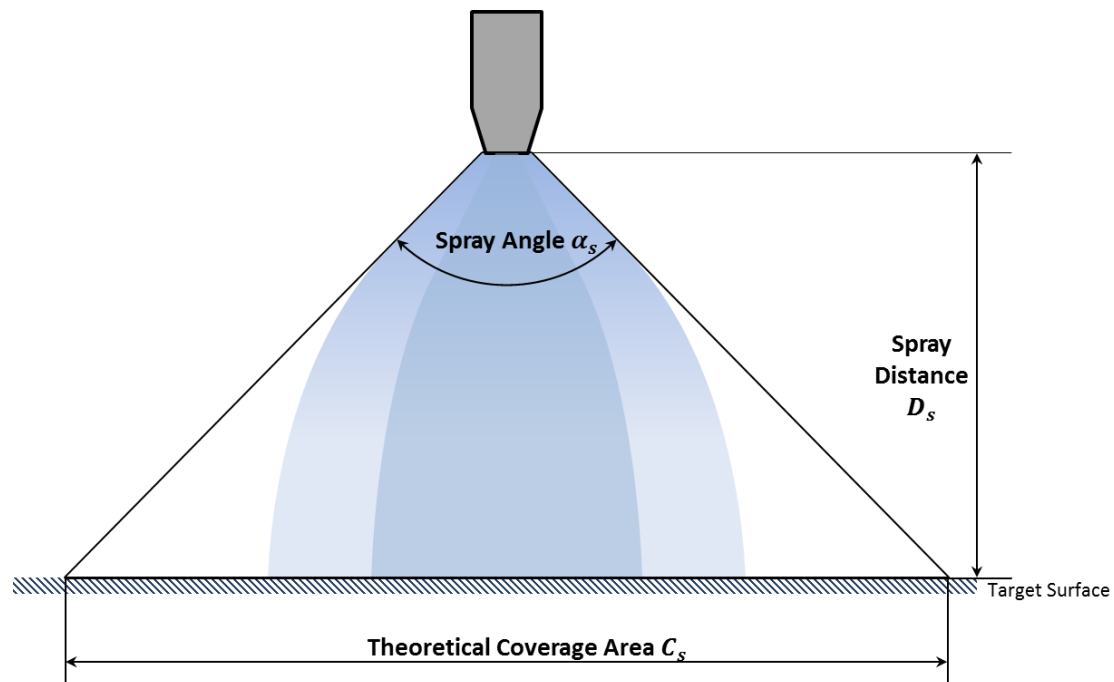


Figure 2.2 Relation between spray angle and theoretical coverage

$$C_s = 2D_s \tan(\alpha_s/2) \quad (2)$$

Spray Drop Size describes sizes of droplets produced by nozzles. Usually a liquid spray contains droplets of a wide range of sizes and it is necessary to use a statistical parameter to represent the averaged droplet size property. Arithmetic mean diameter, D_{10} , volume mean diameter, D_{30} , and Sauter mean diameter, D_{32} are some of the characteristic diameters used for indicating mean droplet sizes. Among these the Sauter Mean Diameter (SMD) is the most popular and can be seen in nearly all catalogues provided by atomizer manufacturers. Equation (3) shows the equation for

calculating the SMD where N_i and D_i are the number and representative diameters of sampled droplets. Equation (3) calculates the ratio between total volumes to total surface area of all the drops. And it is equal to the diameter of a droplet with the same volume-to-surface area ratio.

$$D_{32} = \frac{\sum_{i=1}^k (N_i D_i^3)}{\sum_{i=1}^k (N_i D_i^2)} \quad (3)$$

Laser diffraction, optical imaging and Phase Doppler are the most popular non-intrusive drop size measurement methodologies. Laser diffraction [13] uses the principle of Fraunhofer diffraction to determine droplet sizes [8]. This method has a potential measurement range from 1.2 μm to 1800 μm . Phase Doppler [14], known as PDPA, is a single-particle measurement method. This method is usually used in dense sprays where a sufficient number of drops can be measured in a small sample volume to eliminate the effect of random fluctuations [8]. The measurement range is reported to be between 1 μm and 8000 μm . An optical imaging method has good performance in measuring relatively large droplets (> 500 microns) in medium to low density sprays. Due to the wavelength of light, this method has a size limit for measurement of small droplets.

Droplet distribution is a Probability Density Function of droplet diameters at the place of interest and it is usually presented graphically as the droplet sizes versus the percentages of droplet number, volume or cumulative volume among all sampled droplets.

2.1.2 Classification of Atomizers

There is a wide variety of spray nozzles available in the market and as they target different applications, each of the nozzles has a specific range of flow rate and droplet size [11]. Classifications of atomizers also vary based on different criteria. The most frequently used criteria are the atomizing mechanisms, spray patterns, flow rates and droplet sizes [11]. Figure 2.3 shows the main kinds of nozzles according to different atomizing mechanisms. A single nozzle design usually adopts more than one kind of atomizing mechanism to achieve its required performance so it may belong to more than one of the listed categories.

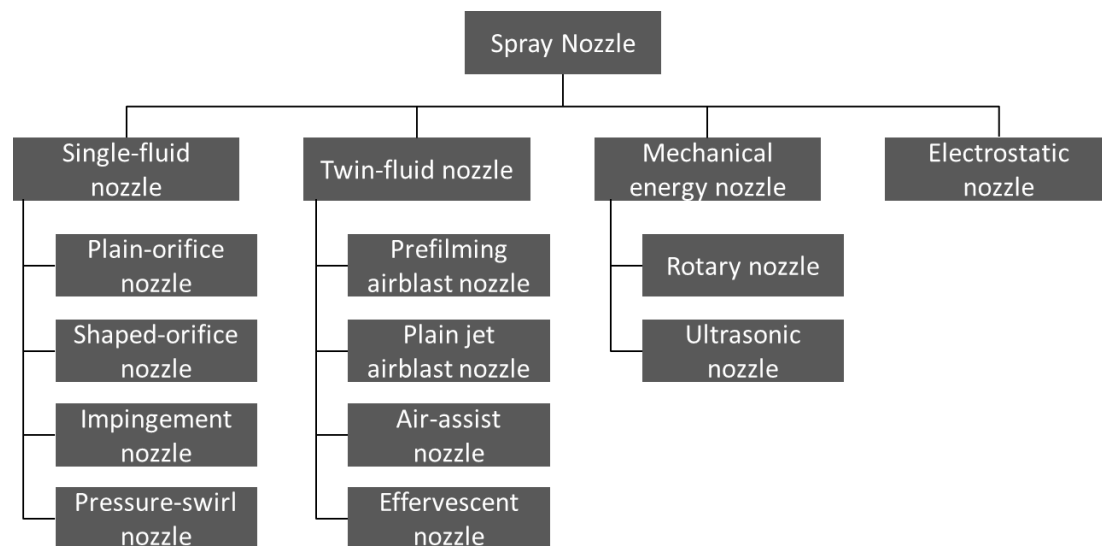


Figure 2.3 Classification of different nozzles based on atomizing mechanisms

Single-Fluid Nozzle or hydraulic nozzle is the most widely used type of nozzle. Nozzles in this category mainly use pressurized liquid and have nozzle geometries designed to obtain the required liquid kinetic energy that allows the liquid flow to be broken into small droplets [11]. With different configurations, it is possible for hydraulic nozzles to produce all the spray patterns listed above [11]. For a single hydraulic nozzle, increasing the spray pressure leads to more liquid flowing through the orifice and finer droplets. Key features for designing single-fluid nozzles include nozzle geometries, shapes and arrangements of nozzle orifices and feeding inlets. Figure 2.4 shows typical configurations of different single-fluid nozzle designs.

Plain-orifice nozzles are the simplest single fluid nozzles which use hydraulic pressure to break the fluid flows. This kind of nozzle can be used for producing a solid stream of liquid with high impact [8]. Under very high spraying pressures it can also achieve fine atomization of materials. A key consideration for the design of a plain-orifice nozzle is the length of discharge orifice [11]. The configuration of a shaped-orifice nozzle is very similar to a plain-orifice nozzle. The main difference between these two types of nozzles lies in the orifice designs. The shaped-orifice nozzles have special inlet and outlet profiles which enable them to produce oval or flat fan spray patterns. Another variation of the hydraulic nozzle is the impingement nozzle. An impingement nozzle also uses hydraulic pressures to insert kinetic energy into the liquid. However, rather than directly discharging the liquid, the pressurized materials hit the deflector plate after they exit from the nozzle orifice, leading to the formation of sheets which breaks up into droplets [11]. Varying the shapes of the

deflector plates can achieve different spray patterns, droplet sizes and spray angles [8]. For example, impingement nozzles with deflector plates of spiral shapes can produce sprays of full-cone or hollow-cone patterns [8]. The last type of usual-seen single-fluid nozzles is the pressure-swirl nozzle which has the potential to produce fine drops. Liquid fed into a pressure-swirl nozzle is forced to rotate inside the nozzle chamber and, once it is discharged, a liquid sheet forms induced by the centrifugal force imparted into the liquid [8], [11]. These nozzles can produce full-cone or hollow-cone sprays and they are widely used for spray drying, gas cooling and dust control [8], [11].

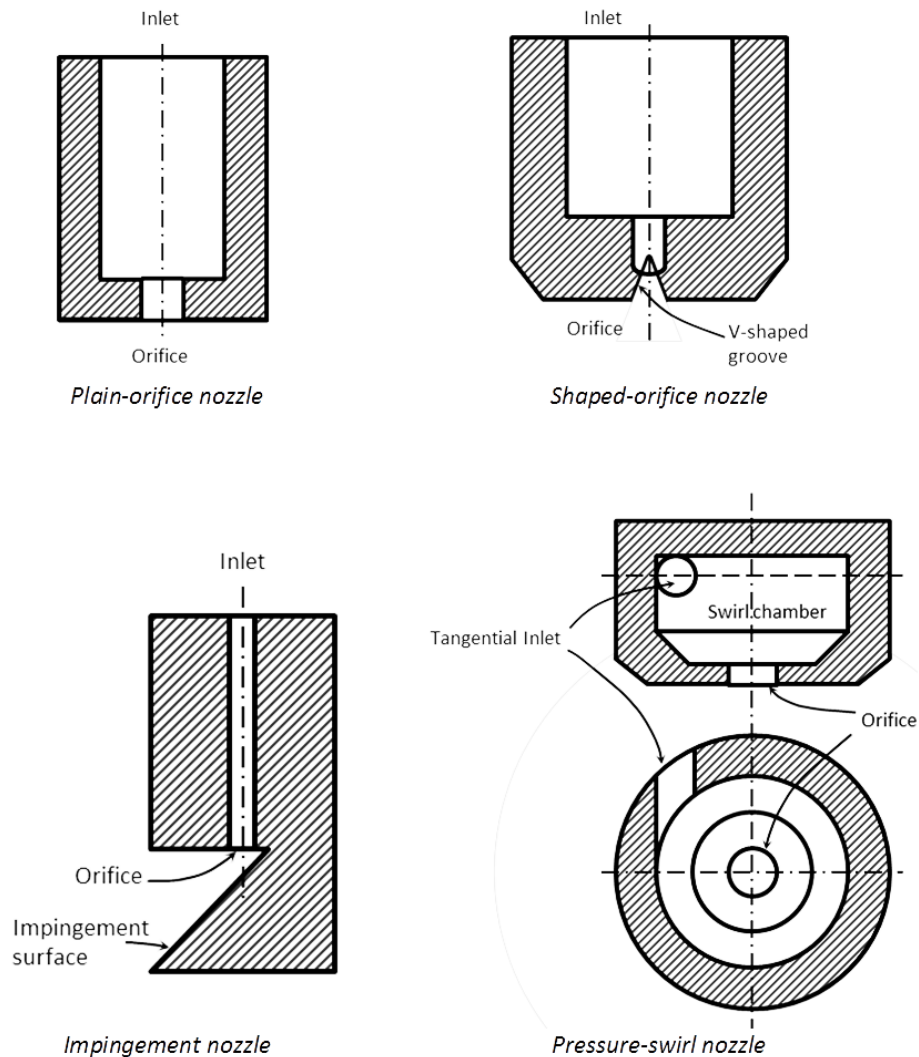


Figure 2.4 Configurations of different hydraulic nozzle designs

Twin-fluid nozzles utilize the interactions between gas-phase and liquid-phase materials to achieve fluid atomization. Compressed air is usually employed as the gas source for spraying. A high-speed gas stream interacts with a liquid stream inside or outside the nozzle body causing the liquid stream to break into ligaments which

further disintegrate into small drops later in the process [11]. In some twin-fluid nozzle designs, the liquid is also pressurized to generate higher kinetic energy so that more severe interactions occur when it impinges into the gas [11]. This family of nozzles can produce sprays of full-cone, hollow-cone, and flat fan patterns. Also different spray impacts, flow rates and droplet size distributions can be obtained from different nozzle configurations [11]. Spray angles from 20° to 60° are within their capabilities. Twin-fluid nozzles are usually used for producing very fine droplets and the droplet sizes of a single nozzle design are closely related to the relative velocities between the liquid and air streams [8] and the discharged gas to liquid mass ratios [11]. Various twin-fluid nozzle designs can be grouped into different types according to the flow rates and the ways that the gas is brought into contact with the liquid [11]. Figure 2.5 shows some typical configurations of twin-fluid designs.

Pre-filming nozzles are the most frequently used twin-fluid nozzles [11], [15]. Their good performance in producing fine droplets is mainly obtained by two steps. The first step is to force the liquid stream through a small annular gap inside the nozzle body in order to form a thin liquid sheet. This helps to increase the surface area of the stream. Then the liquid sheet comes into contact with the high-speed air and breaks into ligaments and drops [11]. Energy from the air is transferred more efficiently to the liquid with a larger contact area between the pressurized air and the liquid stream to be atomized. Moreover, liquid films with smaller film thicknesses have smaller characteristic lengths compared to the original jets which reduce the average droplet sizes [11]. The thickness of the produced liquid sheet is a key design parameter for a pre-filming nozzle design.

Airblast nozzles and air-assist nozzles share the same nozzle configurations. The main distinction between the two types lies in the required operating conditions. For air blast nozzles, conical liquid sheets are exposed to a large volume of low-to-moderate pressure air [8], [9], [11]. High mass ratios of atomized gas to liquid are used in this type of nozzle to achieve atomization. Air-assist twin-fluid atomizers use relatively low gas/liquid mass ratios. But the air is pressurized before feeding into the nozzles and, unlike the airblast nozzles where the air is supplied continuously, air-assist nozzles only introduce the air streams when it is needed [8], [11]. There are a variety of airblast/air-assist nozzle designs but they are all developed from a basic configuration which consists of separated channels for liquid and gas [11]. Liquid and

gas streams can be brought into contact externally or internally. These two types of nozzles are widely used in industrial furnaces or gas turbines [8], [9].

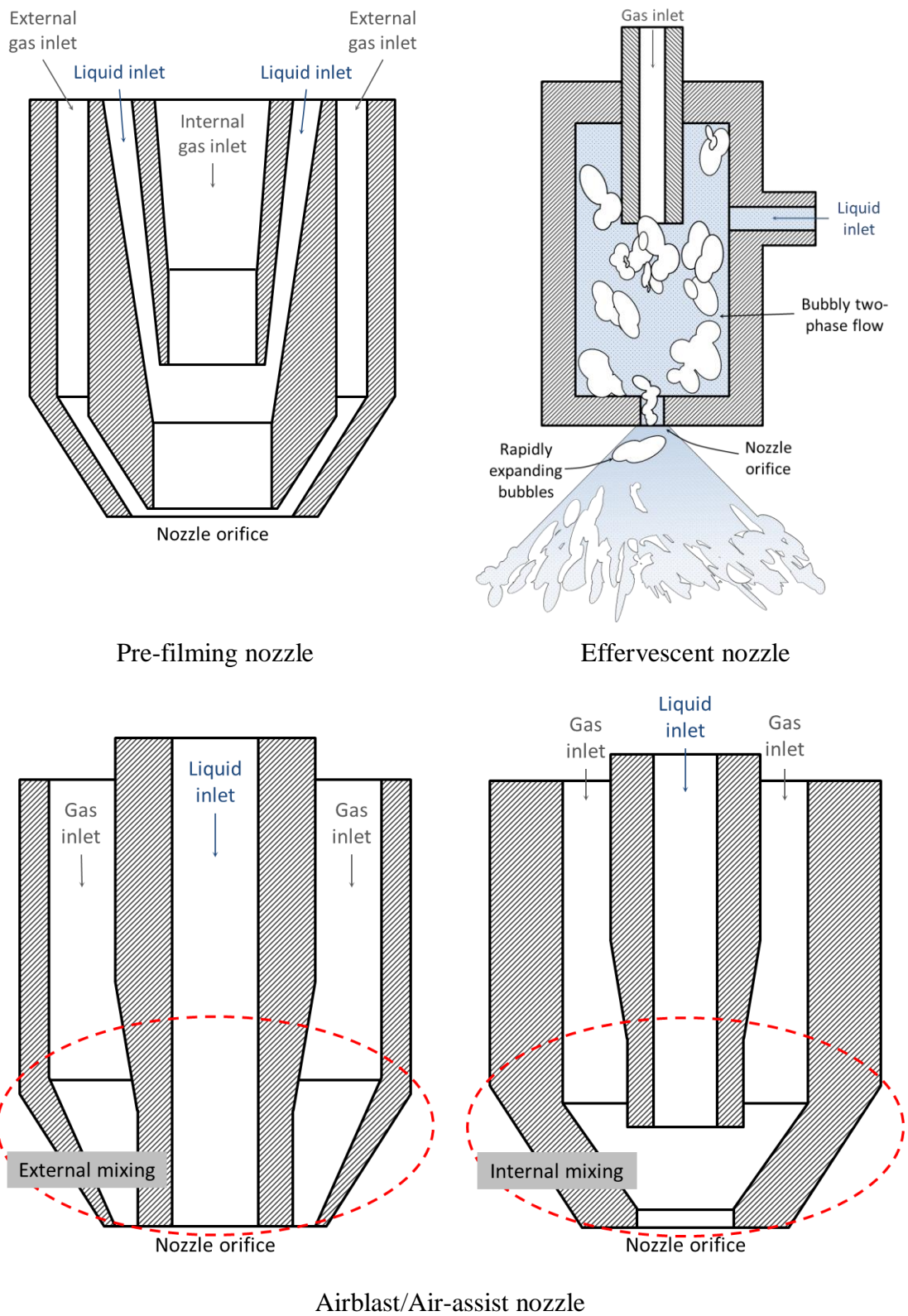


Figure 2.5 Configurations of different twin-fluid nozzle designs

Effervescent nozzles introduce relatively small volumes of gas for atomizing and they are a type of highly effective nozzle. This type of nozzle usually has a simple configuration which includes a gas inlet, a liquid inlet, a mixing chamber and an orifice. Pressurized liquid is fed into the nozzle through the liquid inlet and the gas, with pressures slightly higher than the atomized liquid, are supplied through the gas inlet. Gas and liquid are mixed inside the mixing chamber which generates bubbles. Then the bubbly flows are released from the nozzle orifice causing a sudden pressure drops in the flow, which result in rapid expansion of the bubbles. The liquid is squeezed by the expanding bubbles to form thin ligaments and subsequently breaks into small droplets [11]. Effervescent nozzles are used in different spray systems [11], [16], [17].

Mechanical Energy Nozzles are a family of nozzles that do not rely on hydraulic energy or multi-phase interactions to produce sprays. As their name suggests, they achieve the atomizing processes by imparting different mechanical energy to the liquid. There are various ways for atomizers to apply mechanical energy into flowing liquid streams which contribute to a variety of nozzle designs. The two most popular type of nozzle in this category are rotary nozzles and ultrasonic nozzles.

A rotary nozzle has a spinning disk, cup or wheel which can rotate at high speed. In a spraying process, the liquid to be atomized is fed onto the spinning surface and, under the effect of centrifugal force, the liquid stream breaks into droplets [8], [11]. Rotary atomizers control droplet sizes through adjusting the rotation speeds [8]. This kind of nozzle does not clog during the atomization processes and it can produce relatively uniform droplet sizes [11]. Rotary nozzles can be further categorized as vaneless disk nozzles, vaned disk nozzles and rotary cup nozzles according to the type of rotary surface. The liquid to be sprayed can also be mixed with gas in the atomizing process, forming a twin-fluid rotary nozzle [11]. This type of nozzle usually finds applications in boilers, firefighting, spray painting and lawn sprinklers [8], [11].

In ultrasonic atomization, a piezoceramic element is employed to convert electrical energy to mechanical energy in the form of high-frequency (25 kHz to 120 kHz) vibrations. The mechanical energy is imparted to the liquid, which causes the formation of capillary waves. As the mechanical energy in the liquid increases, capillary waves become unstable and the liquid breaks into small droplets [8], [11].

Droplet sizes produced by this kind of nozzle depend on the nozzle design and vibration frequencies. Droplets produced by ultrasonic atomizers are usually fine and travelling at a relatively low speeds [11]. They are especially suitable for different kinds of coating processes [11].

Electrostatic nozzles are the last kind of nozzle introduced in this review. This class of nozzle produces sprays by employing electric potential energy between the liquid to be atomized and the target surface. An electric charge is applied on the liquid and at the same time, an opposite electric charge is imparted on the impact surface. Increasing the electric potential on the liquid surface forces the droplets to separate from each other and also creates a strong attraction force to the droplets from the impact surface. Droplets are accelerated by this attraction force toward the target surface which creates a spray [8], [11]. Electrostatic nozzles can generate very uniform droplet sizes and they can precisely control the droplet size by controlling the electric charge. However this type of nozzle cannot be widely used because they have relatively low liquid flow rates and there are limitations on the type of liquid to be atomized. The main application for electrostatic nozzles is paint spraying[8], [11].

Apart from the nozzle classification method based on different atomizing mechanisms, spray nozzles can be categorized by the produced spray patterns. These are created by full-cone nozzles, hollow-cone nozzles, solid-stream nozzles and flat-fan nozzles. Many categorization methods have been developed based on the nozzle characteristics of interest.

2.1.3 Patent Review

In order to investigate the state-of-the-art in nozzle designs and their working principles, a patent review was conducted based on the Espacenet¹ patent database. Selected keywords were relevant to multi-material nozzles which can produce fine droplets. Table 2-1 presents a list of reviewed patents categorised according to the main keywords used.

¹ <http://ep.espacenet.com/>

Table 2-1 Review of nozzle-related patents

Inventor / Assignee	Year	Patent No.	Title
ASKAWA ET AL. (NOZZLE NETWORKS CO. LTD)	2013	US2013/0181063	LIQUID ATOMIZING DEVICE AND LIQUID ATOMIZING METHOD
FILICICCHIA ET AL.	2008	PCT/US2008/077096	ULTRASONIC ATOMIZING NOZZLE WITH VARIABLE FAN-SPRAY FEATURE
ADAMS ET AL. (PURE MAINTENANCE)	2013	US2013/140374	ATOMIZING STERILIZATION OF A PLURALITY OF CLEANING AGENTS
WHEELER AND TERRY	2012	WO2012100271	MULTI-HEADED MOBILE FOGGING SYSTEM AND METHOD
MATHE HANS-GEORG	2012	EP2407180	METHOD FOR DISINFECTING SURFACES, FUMIGATION DEVICES AND MOBILE APPLICATION DEVICE
PHILLIPS AND GULDALJ	2009	US2009014558	PORTABLE SPRAYER/MISTER/FOGGING SYSTEM FOR DISPERSING MEDIA IN A UNIFORM AND CONTROLLED MANNER
SHIGEMI KAZUTOYO	2006	JP3860203 / JP2007246397	FOG-FORMING DEVICE AND METHOD FOR FORMING FOG
FENG AT AL. (INST OF FARM IRRIGATION AND DR)	2005	CN2673513	MULTIFUNCTIONAL NOZZLE
ZHANG HUCHENG	2002	CN2470722	CENTRIFUGAL ATOMIZING HUMIDIFIER
LANG HUANPU	2001	CN2443777	MULTIDIRECTIONAL ATOMIZING SPRAY HEAD
Keyword search: misting nozzle			
HUANG YU-QIONG	2013	TWM459027	MICRO-MISTING NOZZLE HAVING HIGH STABILITY
HSIEH PAI-CHOU (YUAN PIN IND CO LTD)	2013	US2013153688	MISTING NOZZLE
ASKAWA ET AL. (NOZZLE NETWORKS CO. LTD)	2013	WO2013065503	LIQUID ATOMIZATION DEVICE
RICHARD AND WILLIAM (PARKER HANNIFIN CORP)	2013	US2013092746	ADJUSTABLE MISTING NOZZLE FOR A DISTRIBUTION MANIFOLD
TORONTOW SHAHN	2012	US2012228407	MULTI-NOZZLE MISTING SHOWER HEAD
LIAO HUANG-ZHEN (TITAN UNITED CO LTD)	2012	TWM427206	HIGH-PRESSURE MISTING-SPRAY NOZZLE STRUCTURE
METCALF KENNETH	2011	US2011309158	AIR DIFFUSING AND WATER MISTING APPARATUS AND METHOD
CHEN YUNG [US]; JUNKEL ERIC F	2012	US2012319308	PORTABLE MISTING DEVICE
PALESTRANT LAURENCE [US]; ANDREWS HERB L (AMFOG NOZZLE TECHNOLOGY INC)	2009	US2009308953	ATOMIZING NOZZLE
	2007	US2007075165	MISTING DEVICE
CRITCHFIELD ROLAND	2007	US2007089448	PORTABLE MISTING SYSTEM
LAWYER JERRY D	2006	US7152816	MISTER NOZZLE APPARATUS

Keyword search: Twin-fluid nozzle			
K C TECH CO LTD	2009	CN101372001	TWIN-FLUID NOZZLE FOR CLEANING SUBSTRATE
HIRAKIKAWA HITOSHI (SPRAYING SYSTEMS CO JAPAN)	2009	KR20090051735	TWIN FLUID SLIT NOZZLE AND MANUFACTURE METHOD THEREOF
YAMAGUCHI ET AL. (KYORITSU GOKIN CO LTD)	2007	KR20070107597	TWIN-FLUID NOZZLE AND SPRAYING METHOD USING THE SAME
KIM ET AL. (KOREA INSTITUTE OF ENERGY RESEARCH)]	2006	KR100622987	TWIN FLUID ATOMIZING NOZZLE
COMBELLACK JOSEPH HENRY	2000	WO0056464	ATOMISING NOZZLE
NEWTON DAVID	1999	GR3030922	TWIN FLUID NOZZLE
WALZEL PETER PROF DR (WEBASTO THERMOSYSTEME GMBH)	1999	DE19752245	TWIN SUBSTANCE NOZZLE FOR ATOMIZED SPRAY
MASAI ET AL. (BABCOCK HITACHI K)	1989	JPH01184055	TWIN FLUID SPRAY NOZZLE
Keyword search: Multi-fluid nozzle			
WURZ DIETER [DE]; HARTIG STEFAN	2013	US2013037628	EXTERNALLY MIXING MULTI-COMPONENT NOZZLE
FENG ET AL. (HEILONGJIANG NORTH AGRICULTURE ENGINEERING CO LTD)	2012	CN202113969	MULTI-NOZZLE COMBINED REMOTE SPRAY GUN
PENG YUAN; NINGNING GONG (FOREVER TECHNOLOGY CO LTD)	2011	CN201735462	MULTI-FLUID NOZZLE EQUIPMENT FOR SPRAYING
keyword search: adjustable nozzle			
STEINGASS ET AL(TASK FORCE TIPS INC)	2013	US2013256427	ADJUSTABLE FIREFIGHTING NOZZLE
KAH JR CARL L C (RAIN MFG CORP K)	2013	WO2013131086	SELECTABLE ARC AND RANGE OF COVERAGE SPRAY NOZZLE ASSEMBLY WITH MULTIPLE FLUIDIC FAN SPRAY NOZZLES
ZHIFA HOU	1992	CN2117212	ADJUSTING RANGE AND SPRAYING NOZZLE

2.1.4 Design Review

To further study the configurations of different spray nozzles and their capabilities, a product review was carried out based on different nozzles produced by various manufacturers. Both single-fluid and multi-fluid nozzles were covered in the review and the focus was put on the ranges of droplet sizes and flow rates that each kind of nozzle can produce with varying spraying pressures. The review consisted of two steps. The first step was finished by collecting information from manufacturers'

official websites and catalogues. Products from BETE², Spraying Systems Co.³, H.IKEUCHI & Co.⁴ and Lechler⁵ were reviewed in this step and Appendix A.1 in Appendix A shows the collected data.

In the second step, this product review was broadened by the assist of the NOZNET⁶ Spray Nozzle Global Search System (SGS). This system contained information for more than 70,000 atomizers from 21 manufacturers all over the world. Searching criteria included categories of required nozzles (spray materials, nozzle types), spray patterns and required specifications (e.g. manufacturers, pressure flow rates). Table 2-2 lists the nozzles reviewed in this study.

Table 2-2 List of reviewed nozzle designs

Manufacturer	Model
Single fluid axial full cone nozzle	
BETE	1FNC1009w-1
BETE	2FMP750W-2
Single fluid axial hollow cone nozzle	
Niikura	F11/2EX5120W-PVC
Niikura	F2EX5300W-PP
Single fluid tangential full cone nozzle	
H. Ikeuchi & Co., Ltd	3/4MAJP80AL92
Niikura	F2EX2300WL-PP
Single fluid tangential hollow cone nozzle	
Katorigumi Mfg. Ltd	K-4-RC3/4-14.2-BC
Katorigumi Mfg. Ltd	K-4-RC11/4-19.2-BC
Twin fluid axial full cone nozzle	
BETE	SA2303-7
BETE	1/4XA00PR050A-7
Twin fluid axial full cone nozzle	
Delavan Ltd.	31618-1
BETE	1/4XA00XW050B-7
Delavan Ltd.	31618-1

Figure 2.6 shows the flow rates of different nozzle designs with increasing pressure. Different nozzles are presented by curves of different colours. Red lines and orange lines covering the largest area in the figure, indicating that single fluid tangential full cone nozzles and single fluid axial hollow cone nozzles can achieve the largest range

² <http://www.bete.com/>

³ <http://www.uk.spray.com/>

⁴ <http://www.kirinoikeuchi.co.jp/eng/>

⁵ http://www.lechler.de/index-en_US

⁶ <http://sgs.nozzle-network.com/en/index.html>

of flow rate with the change of pressure. The tangential model F2EX5300W-PP and the axial model F2EX2300WL-PP of Niikura can produce flow rates from less than 120 L/min to 600 L/min with working pressure changes from 1 bar to 10 bar. For the twin fluid nozzles, curves in cyan and green indicate the possible ranges of water flow rate. The axial full cone design SA2303-7 from BETE has a flow rate up to 80 L/min and 31618-1 from Delavan Ltd can generate spray from 5 L/min to 56 L/min. Generally, at the same water pressure, the flow rate of water from a twin fluid nozzle is much lower than the one from a single fluid nozzle. In Figure 2.6, a straight line in black is drawn across the graph perpendicular to the axis for flow rate. This line marks the flow rate of 120 L/min which is well below the maximum flow of single fluid nozzles but is hard to be achieved by twin fluid nozzles.

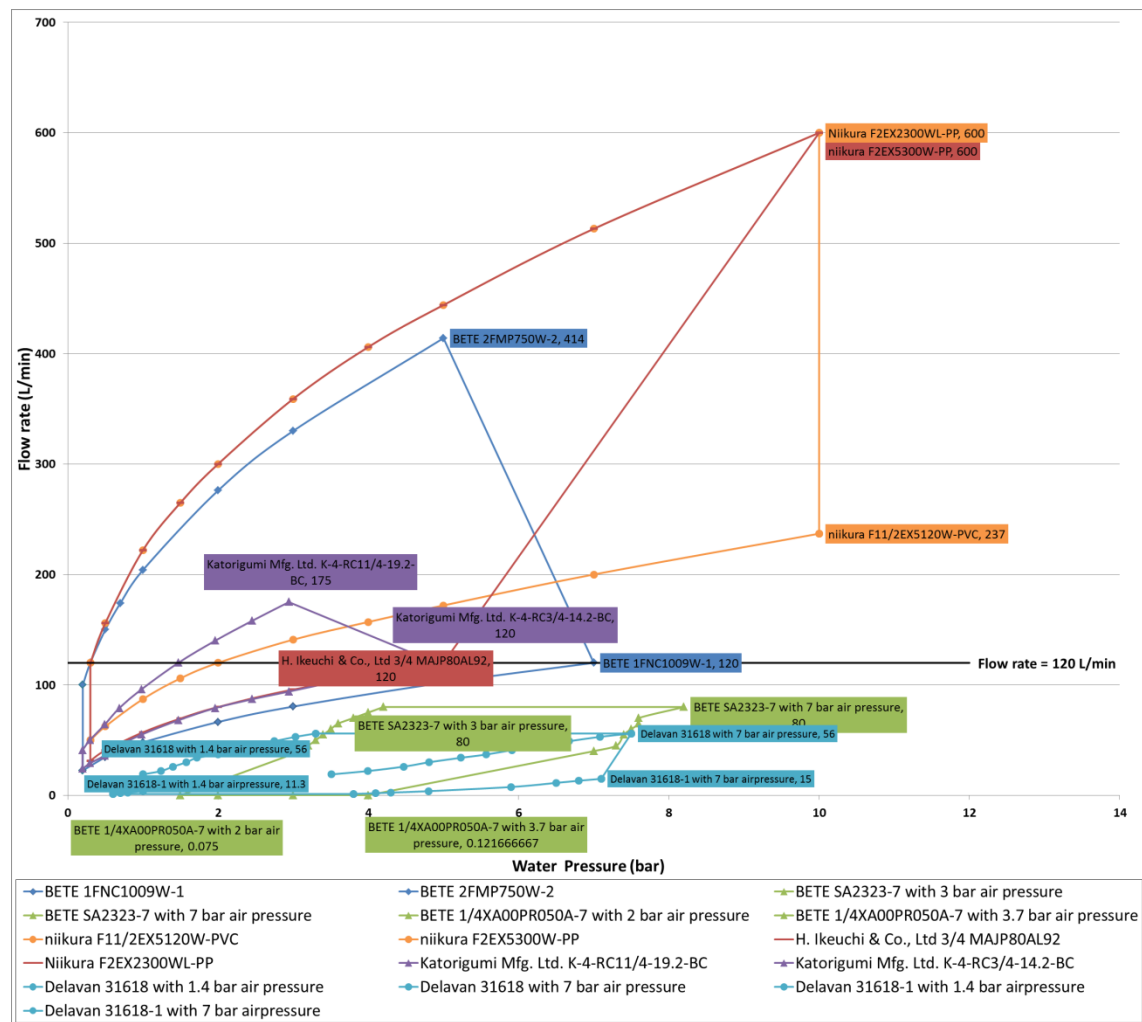


Figure 2.6 Flow rates produced by various nozzles with different water pressure

The diameter of the produced droplet is another characteristic for nozzle evaluation. Data of droplets atomized from single fluid nozzles and twin fluid nozzles were

collected. Figure 2.7 shows the sizes of droplets produced by single fluid axial full cone nozzles.

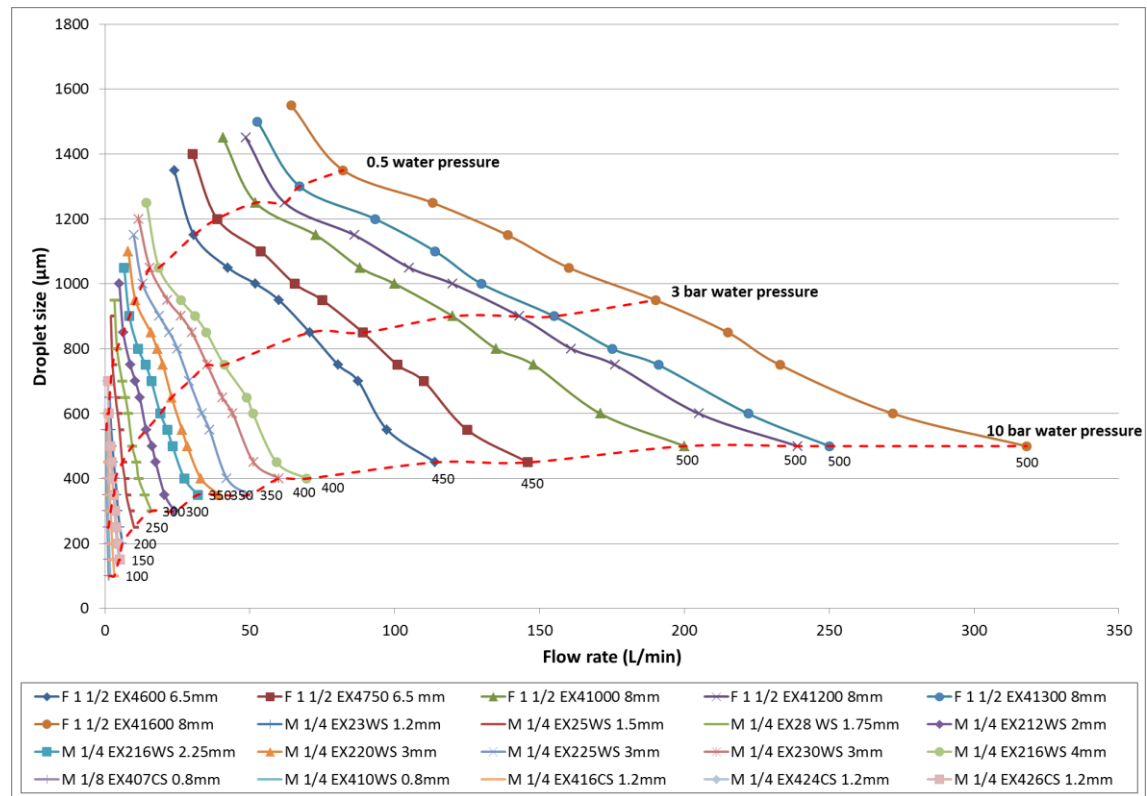


Figure 2.7 Mean droplet sizes produced by single fluid axial full cone nozzle with different flow rates

In this figure, droplets from 20 models of nozzle designs are recorded. Curves for different models are distinguished by colours and symbols. Similar patterns can be observed among different models regarding the relationship between water pressure, flow rate, and droplet size. For all the models, flow through the nozzle increases with increasing water pressure. At the same time, a decrease in produced droplet size is noticed. For the model comparison, nozzles that are capable of producing smaller droplets have smaller flow rates. The smallest droplet produced by the axial full cone nozzle has a size of $100 \mu\text{m}$ at water pressure of 10 bar with a flow rate of 3.2 L/min . Similar sets of data are also collected for axial hollow cone, tangential full cone, and tangential hollow cone nozzles. Results are shown in Appendix A.2 - Appendix A.4.

Apart from single fluid nozzles, sizes of droplets generated by twin fluid nozzles were also researched. As there is not as much information for twin fluid nozzles as there are for single fluid nozzles, only 4 models of full cone nozzles and 1 model of a hollow cone nozzle are studied. Figure 2.8 shows the relationship between the flow of water

and size of droplet from twin fluid nozzles it shows that the droplet becomes larger as the flow rate increases. This is different from what was observed from single fluid nozzles. As mentioned above, the performance of twin fluid nozzles is affected by the combination of air and water supply. Lines in blue, in red, and in green indicate the same nozzle working at different air pressures. For twin fluid nozzles, it is possible to obtain the same water flows with different droplet sizes. Data for a hollow cone nozzle is presented in Appendix A.5. Generally a twin fluid nozzle is able to generate sprays with fine droplets which are usually smaller than $100\ \mu\text{m}$.

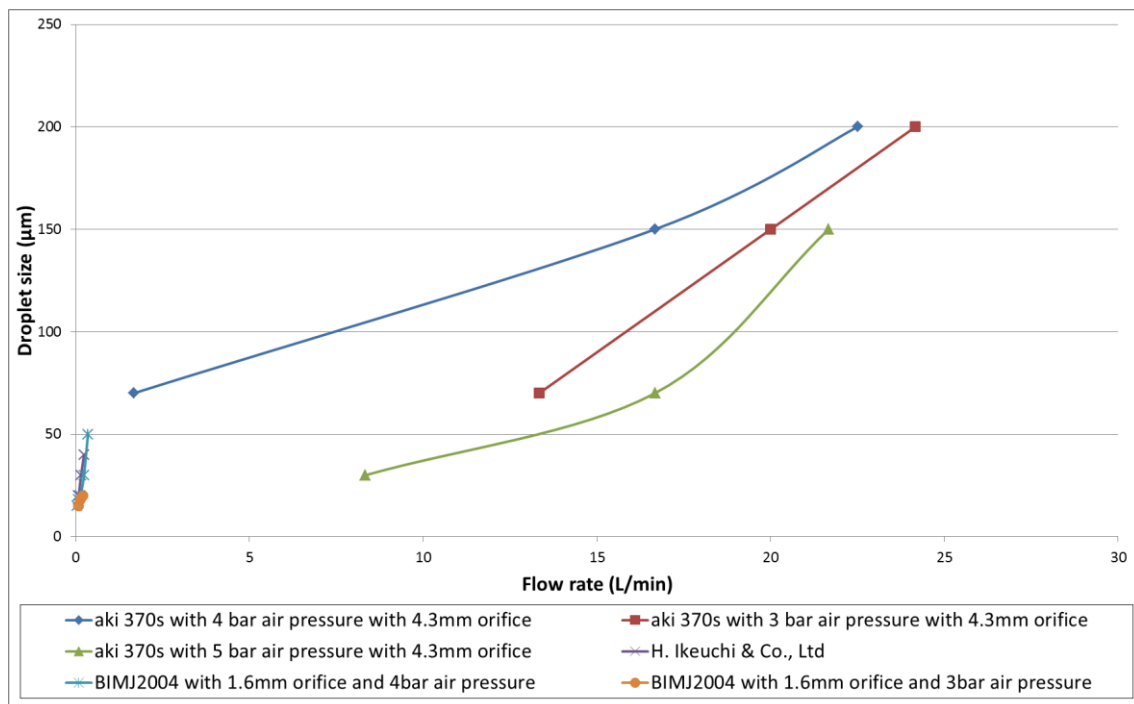


Figure 2.8 Mean droplet sizes produced by twin fluid full cone nozzle with different flow rates

Putting information of single fluid nozzles and twin fluid nozzles together, a direct comparison can be made between the two nozzle configurations regarding flow rate and droplet size. In Figure 2.9, performance of 4 single-fluid nozzles and 2 twin-fluid nozzles are presented. Different types of nozzles are distinguished by the colours. The area within a close loop of lines defines the combinations of droplet size and flow rates achievable by the nozzle that is represented by the colour. Some conclusions can be made as follow:

- A single fluid nozzle has a much larger range of achievable flow rates and droplet sizes

- A twin fluid nozzle can obtain smaller droplets than a single fluid nozzle. The smallest droplet obtained by the reviewed twin fluid nozzles has a diameter of $15 \mu\text{m}$ while droplets from single fluid nozzles are no less than $100 \mu\text{m}$;
- While discharging the same rate of water, a twin fluid nozzle is able to produce smaller droplets.

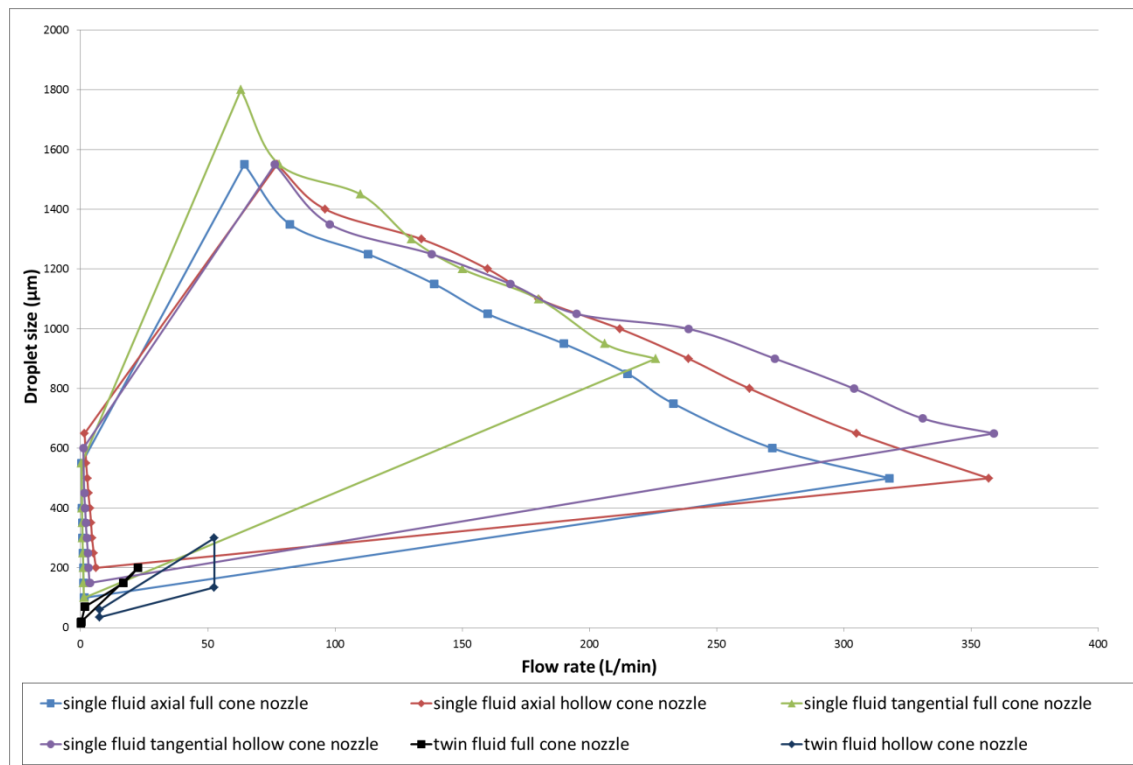


Figure 2.9 Performance of single fluid nozzle and twin fluid nozzle

2.2 Challenges in Advanced Nozzle Design

Design of micro-droplet generators and their applications are popular topics in academic research. The former includes investigations on advanced nozzle design [18]–[21], droplet breakup mechanisms [22]–[25], numerical models for droplet description [26]–[29], experiments for nozzle characterization [26]–[29], and measurement techniques for small droplets [30]–[32]. The latter focuses on studying the droplet size effect on different applications [33]–[39].

In pest management, it is reported by Wei-Cai et al. [39] that the optimum droplet size for pesticide distribution for crop protection is between the range of $50 \mu\text{m}$ and $300 \mu\text{m}$. Droplets within this range can penetrate the crop canopy and form a high coverage, while larger drops flow away from the crop surface more easily, which

results in low coverage density and reduced biological efficacy. Large amount of fine droplets can also be useful for fire suppressions, especially in situations where spaces are confined and water is limited. For the same volume of water droplets with smaller diameter have a larger surface area which enhances vaporization. Fires are mainly suppressed by oxygen displacement and cooling provided by vaporized droplets in a water mist [36]. Using water mist for fire suppression can also reduce the water supply requirement, reduce the potential for damaging electronic device by water, and avoid releasing any pollutant [35], [36]. Many studies have reported the effectiveness of water mist systems for suppressing fires of different classes [35], [36], [40]. A recent study shows that fine sprays are useful for dust suppression [33]. Fine-dispersion dust with sizes from $1\ \mu\text{m}$ to $10\ \mu\text{m}$ (PM2.5 and PM10) can be harmful to the human body. Fine spray is suitable for dust suppression because of its high efficiency, relatively low cost, and no requirements for complicated systems. However, to trap dust particles successfully, droplets must have similar sizes to the targeted particles. If the droplet is considerably larger than the particle, air flow around the droplet tends to carry the dust particle away (Figure 2.10).

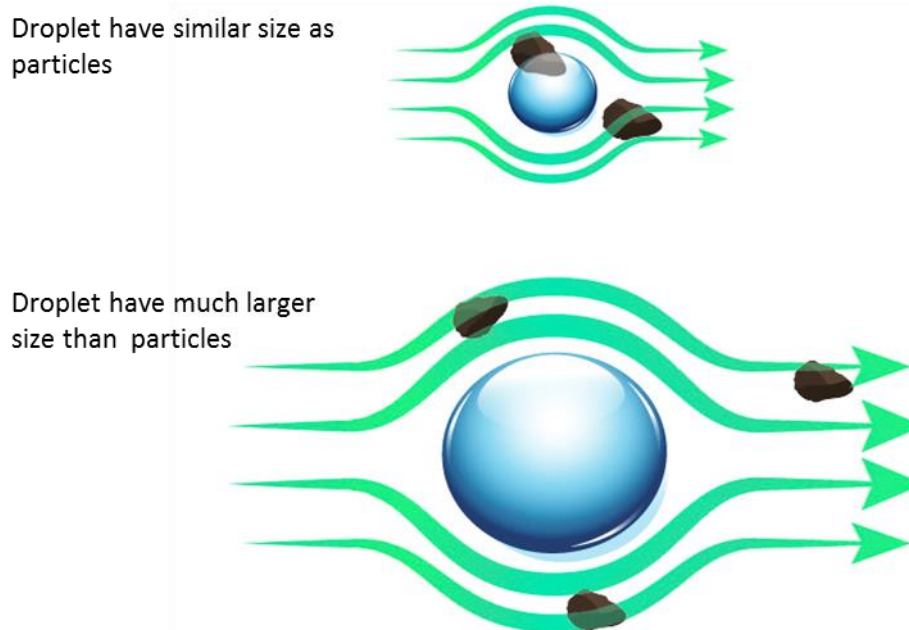


Figure 2.10 Effect of droplet size for trapping particles

Although many nozzle designs are newly developed (Section 2.1.3) or already available in the market (Section 2.1.4), it can be seen from Figure 2.9 that nozzles which can produce small droplets have low flow rates. This reduces the efficiency of fine-spray nozzle and requires longer atomization time to achieve tasks for pest management, fire suppression, and dust removal. Fine droplets and high flow rate are

contradictive aspects of nozzle performance and achieving both of them at the same time remains a challenge in advanced nozzle design.

2.3 Nozzle Design Procedures

Since atomizing nozzles are very popular devices for producing sprays with different characteristics, many investigations have been carried out on obtaining the optimum profiles for nozzle internal shapes. As illustrated above, different types of nozzles have different configurations and key features. For example, a swirl nozzle usually has a swirl inset while impingement nozzles have shaped external impingement surfaces. So the empirical correlations, key nozzle dimensions and flow conditions for nozzle designs vary according to specific nozzle types.

Davies and Jackson [41] introduced a numerical method which solved stream equations for selecting nozzle geometries to create the greatest impact with a given input pressure. Besides, they used boundary layer analysis coupled with empirical correlations to guide the surface finish requirements. Their study intended to develop nozzles for cutting and mining purposes. Lacava et al. [42] and Chin et al. [43] proposed similar procedures for designing pressure-swirl atomizers and effervescent atomizers. Both methods started with the calculations for flow number FN from liquid mass flow rates, liquid densities and injection pressure differentials. In Lacava's study, the nozzle discharge diameter was determined in advance and then other atomizer geometrical parameters for a pressure-swirl nozzle were selected accordingly under the guidance of dimensionless groups. Each of these dimensionless groups was solved based on recommended values from previous research or previously established empirical correlations related to the discharge coefficient [42]. Chin proposed to obtain proper length/diameter ratios of discharge orifices and nozzle convergence angles of effervescent atomizers according to the discharge coefficient and air/liquid ratio. Optimum values for the number and size of the air injection holes and the diameters of the mixing chambers were calculated based on analytical results of the complex flow phenomena happening in effervescent atomization.

More recent investigations of atomizer designs and optimizations are increasingly relying on numerical simulations. CFD models have been studied and developed to gain a deeper insight into the nature of the nozzle internal flows which are inaccessible from experimental observations. Sipatov [44] carried out three-

dimensional simulations on an air-blast atomizer which can be used in air craft engines. The study focused on investigating the factors which can influence the spray quality and, based on the numerical studies, the nozzle was optimized by changing the design of the swirl and discharge opening diameter. Sprays with finer droplet sizes and less circumferential non-uniformity distributions were produced by the optimized nozzle design[44]. Melanie [45] numerically studied the influences of flow conditions and physical properties on mean film thicknesses from pre-filming nozzles. The simulation results were used to correlate the relations between film thickness and gas velocity, working pressure, surface tension, gas kinematic viscosity, and liquid kinematic viscosity. This correlation can be used for guiding pre-filming atomizer design [45]. A numerical approach was adopted by Dongmo [46] to study the high velocity suspension flame spraying (HVSFS) combustion and flow dynamic system. The CFD simulations helped to determine the effect of individual parameters on the process and also optimized the nozzle by changing the injection angle for suspension injection. This reduced the evaporation length and eliminated the cooling effect [46].

Although different mathematical, empirical or computational methods were used for designing atomizers for different applications, the general process for nozzle design and optimization can be described in the following five points.

1. *Recognition of end-user requirements.* This includes identification of use-case scenarios and detailed spray requirements such as droplet size, flow rate, spray pattern and liquids involved in atomization.
2. *Outlet parameters definition.* These are the parameters that the nozzle will work with. They are the liquid properties (densities, surface tensions, and viscosities), discharge ambient characteristics (ambient pressure, density and viscosity) and liquid injection conditions (mass flow rate and the injector pressure differential).
3. *Configuration selection.* Nozzle designs usually begin by selecting a suitable base model according to the requirements and outlet parameters. The base model can be as simple as a plain-orifice nozzle design or a complex nozzle configuration like a pressure-swirl nozzle or a pre-filming nozzle;
4. *Detailed design.* This is the most important part in the whole nozzle design process. It can be accomplished by mathematically solving the flow equations using the empirical correlations or adopting the CFD method as described

above. The defined liquid properties, ambient characteristics and injection conditions are used as input parameters and boundary conditions. Design variations are based on the selected nozzle configuration. Requirements from spray applications are used as design targets in the detailed nozzle development process.

5. *Experiments.* This is an essential step for validating the method adopted for designing the nozzle and also examining the nozzle performance.

2.4 Summary

This chapter focused on reviewing nozzle designs and their performances. In this chapter:

- Spray pattern, capacity of water, impact on targeted surface, spray angle, mean droplet size, and droplet distribution of spray have been studied and presented. These characteristics define the performance of nozzles and also limit their applications. Certain applications of fog would determine specific requirements for these spray characteristics and it is the nozzle development technology that attempts to achieve or even exceed the requirements set by the application.
- Mechanisms behind different categories of nozzles for converting bulk fluid flows into dispersed droplets have been revealed. Single-fluid nozzles mainly use the combination of pressurized liquid and nozzle geometry to breakup droplets while twin-fluid nozzle induces droplet instability by multiphase interaction. It is essential to understand these mechanisms when nozzle optimization is needed.
- A patent review has been conducted including information of more than 30 advanced nozzle designs based on the Espacenet patent database. Information of this review has been further expanded by a following design review which studied the performances of more than 40 commonly used nozzles with the assist of the NOZNET Spray Nozzle Global Search System (SNGS). Results of the reviews have been concluded and plotted in Figure 2.9. Generally speaking a single fluid nozzle is able to produce spray with a high flow rate and large droplets while a twin fluid nozzle produces much smaller drops at lower water flow rates.

- By analysing data collected from existing nozzle designs and also considering the developing need for high-performance sprays, challenges for developing advanced nozzle design have been recognized. Sprays with high flow rates and fine droplet sizes have never been generated by existing nozzle designs although this spray would have a great potential for wide application.
- A process for nozzle development has been developed here. This process will be repeated several times in this study to obtain the final optimized nozzle design.

Chapter 3

CFD Modelling of Multiphase Atomization

This chapter presents information of numerical models related to the simulation of the atomization process. Main discussions include:

- **Fundamentals of Computational Fluid Dynamics (CFD)** representing the conservation laws of mass and momentum in a predefined calculation domain;
- **Turbulent models** which are used to calculate additional unknown variables for fluctuating components introduced in the averaging process;
- **Multiphase models** either based on Eulerian-Eulerian or Eulerian-Lagrangian methods accounting for interactions between immiscible phase in the calculation domain;
- **Droplet dynamics models** which define criteria for droplet breakup, collision and coalescence.

3.1 Basics of Computational Fluid Dynamics (CFD)

The main focus of fluid dynamics is to study the field of interest which describes the fluid flow in a predefined calculation domain. Problems or phenomena studied in fluid dynamics are usually macroscopic and activity at the microscopic scale is not important. In this case, fluid is treated as continuum, of which the flow can be described by using the conservation laws of mass and momentum. The equation for

conservation of mass (or continuity equation) defines that the mass accumulated within a system is equated to the difference between the mass entering and leaving that system. And the conservation equation of momentum states that momentum within a system can neither be created nor be destroyed but can only be changed by the action of forces.

Conservation equations for mass and momentum are the fundamental equations in Computational Fluid Dynamics (CFD). Mass conservation in the CFD system is defined by [4]

$$\frac{\partial \rho}{\partial t} + \nabla \cdot (\rho \vec{v}) = S_m \quad (4)$$

which is a general form of the continuity equation. This equation is applicable for incompressible as well as compressible flows. $\frac{\partial \rho}{\partial t}$ is the accumulation of mass in a control volume and $\nabla \cdot (\rho \vec{v})$ is the mass flux. ρ denotes the material density and \vec{v} is the flow velocity vector field. S_m represents the mass source which is transferred from the secondary phase to the primary phase and any user specified sources. The conservation of momentum in fluid flow is described by [4]

$$\frac{\partial}{\partial t} (\rho \vec{v}) + \nabla \cdot (\rho \vec{v} \vec{v}) = -\nabla p + \nabla \cdot (\bar{\tau}) + \rho \vec{g} + \vec{F} \quad (5)$$

where p is the static pressure, $\frac{\partial}{\partial t} (\rho \vec{v}) + \nabla \cdot (\rho \vec{v} \vec{v})$ is the rate of change in momentum, $\bar{\tau}$ represent the stress tensor, $\rho \vec{g}$ is the gravitational body force, and \vec{F} is the external body force.

Stress tensor in the conservation equation for momentum can be calculated by

$$\bar{\tau} = \mu \left[(\nabla \vec{v} + \nabla \vec{v}^T) - \frac{2}{3} \nabla \cdot \vec{v} I \right] \quad (6)$$

here μ denotes the molecular viscosity, I represents the unit tensor.

These two conservation equations for mass and momentum are solved for all flows while additional equations may also be included in the analytical process depending on the problem concerned. Energy conservation is necessary if heat transfer or compressibility is considered in the flow. Species conservation equations for mixing, transport and reaction of chemical species are included to describe convection,

diffusion, and reaction sources for each component species. Also additional transport equations are solved if the effect of turbulence is important.

3.2 Models for Turbulent Fluctuation

Turbulent flow is commonly seen in fluid flows occurring in nature or created in engineering applications. In fluid dynamics, turbulence is fluid motion characterized by fluctuating fields of pressure and velocity. The onset of turbulence can be predicted by the ratio of inertial forces to viscous forces within a fluid, which is called the Reynolds number. Affected by the fluctuating velocity, transported quantities such as momentum, energy, and species concentration in different conservation equations also experience chaotic changes. To solve these changes directly by using Direct Numerical Simulation (DNS), the size of mesh is required to be finer than the length scale of the smallest turbulent eddies which becomes smaller with an increasing Reynolds number. Also the numerical time step has to be set smaller than the time scale of turbulent fluctuations. These two requirements make this method too computationally expensive and not practical for engineering calculations. Instead, instantaneous variables of turbulent flow can be decomposed into mean (ensemble-averaged or time-averaged) and fluctuating components to remove the resolution of small scales. The fluctuating component is used to represent the turbulent fluctuation. This method results in a modified set of equations with additional unknown variables due to the averaging process and the equations need to be closed by an additional turbulence model.

ANSYS Fluent provides several turbulence models while only the most commonly used ones will be introduced here

3.2.1 $k - \epsilon$ Model

The $k - \epsilon$ Model is a two equation model which can be subdivided into standard, RNG, and realizable $k - \epsilon$ models. Main differences between the three sub-models are methods of calculating turbulent viscosity, turbulent Prandtl numbers governing the turbulent diffusion of k and ϵ , and the generation and destruction terms in the ϵ equation.

The standard $k - \epsilon$ model [47] uses two separate transport equations to independently determine the turbulent velocity and length scales. It is assumed that the flow is fully

turbulent in the standard $k - \epsilon$ model. Turbulent kinetic energy, k , in this model is defined as

$$\begin{aligned} \frac{\partial}{\partial t}(\rho k) + \frac{\partial}{\partial x_i}(\rho k u_i) &= \frac{\partial}{\partial x_j} \left[\left(\mu + \frac{\mu_t}{\sigma_k} \right) \frac{\partial k}{\partial x_j} \right] \\ &+ G_k + G_b - \rho \epsilon - Y_M + S_k \end{aligned} \quad (7)$$

where $\frac{\partial}{\partial t}(\rho k) + \frac{\partial}{\partial x_i}(\rho k u_i)$ is the rate of change in turbulent kinetic energy, u_i is the velocity component in corresponding direction, G_k represent the generated turbulence kinetic energy due to mean velocity gradients. G_b denotes the turbulence kinetic energy generated due to buoyancy. Y_M is the contribution of the fluctuating dilatation in compressible turbulence to the overall dissipation rate. σ_k is the turbulent Prandtl number for k . S_k is the user-defined source terms. Similarly, turbulence dissipation rate, ϵ , is defined as

$$\begin{aligned} \frac{\partial}{\partial t}(\rho \epsilon) + \frac{\partial}{\partial x_i}(\rho \epsilon u_i) &= \frac{\partial}{\partial x_j} \left[\left(\mu + \frac{\mu_t}{\sigma_\epsilon} \right) \frac{\partial \epsilon}{\partial x_j} \right] \\ &+ C_{1\epsilon} \frac{\epsilon}{k} (G_k + C_{3\epsilon} G_b) - C_{2\epsilon} \rho \frac{\epsilon^2}{k} + S_\epsilon \end{aligned} \quad (8)$$

here $\frac{\partial}{\partial t}(\rho \epsilon) + \frac{\partial}{\partial x_i}(\rho \epsilon u_i)$ is the rate of change in turbulent dissipation energy, $C_{1\epsilon}$, $C_{2\epsilon}$, and $C_{3\epsilon}$ are constants. σ_ϵ is the turbulent Prandtl number for ϵ . S_ϵ is the user-defined source terms.

The turbulent viscosity, μ_t , is described as

$$\mu_t = \rho C_\mu \frac{k^2}{\epsilon} \quad (9)$$

where C_μ is a constant.

RNG $k - \epsilon$ model [48] refines the standard model by including an additional term in the ϵ equation to improve the accuracy, by taking the effect of swirl on turbulence into consideration, by providing an analytical formula for turbulent Prandtl numbers, and by extending the model for low-Reynolds-number effects. The turbulence kinetic energy, k , and its rate of dissipation, ϵ , have a similar form to the ones defined in the standard model, which are

$$\begin{aligned} \frac{\partial}{\partial t}(\rho k) + \frac{\partial}{\partial x_i}(\rho k u_i) &= \frac{\partial}{\partial x_j} \left(\alpha_k \mu_{eff} \frac{\partial k}{\partial x_j} \right) \\ &+ G_k + G_b - \rho \epsilon - Y_M + S_k \end{aligned} \quad (10)$$

and

$$\begin{aligned} \frac{\partial}{\partial t}(\rho \epsilon) + \frac{\partial}{\partial x_i}(\rho \epsilon u_i) &= \frac{\partial}{\partial x_j} \left(\alpha_\epsilon \mu_{eff} \frac{\partial \epsilon}{\partial x_j} \right) \\ &+ C_{1\epsilon} \frac{\epsilon}{k} (G_k + C_{3\epsilon} G_b) - C_{2\epsilon} \rho \frac{\epsilon^2}{k} - R_\epsilon + S_\epsilon \end{aligned} \quad (11)$$

α_k and α_ϵ are the inverse effective Prandtl numbers for k and ϵ . μ_{eff} is the effective viscosity.

The RNG model adopted a differential equation for turbulent viscosity:

$$d \left(\frac{\rho^2 k}{\sqrt{\epsilon \mu}} \right) = 1.72 \frac{\hat{v}}{\sqrt{\hat{v}^3 - 1 + C_v}} d\hat{v} \quad (12)$$

where

$$\hat{v} = \mu_{eff} / \mu \quad (13)$$

$$C_v \approx 100 \quad (14)$$

By integrating Equation (12), the RNG model defines changes in effective turbulent transport due to the effective Reynolds number. In this case, the model is more applicable for low-Reynolds-numbers and near-wall flows.

The additional term R_ϵ in ϵ equation makes this model different from the standard $k - \epsilon$ model. Value of R_ϵ is calculated by

$$R_\epsilon = \frac{C_\mu \rho S_k^3 (1 - S_k / \eta_0) \epsilon^2}{1 + \beta S_k^3} \frac{\epsilon^2}{k} \quad (15)$$

where $\eta_0 = 4.38$, $\beta = 0.012$.

By adding R_ϵ to the ϵ equation, the RNG model gives comparable results to the standard $k - \epsilon$ model in weakly or moderately strained flow, and gives lower turbulent viscosity in rapidly strained flows. The RNG $k - \epsilon$ model is more applicable for flow with rapid strain and streamlines curvature than the standard $k - \epsilon$ model.

The realizable $k - \epsilon$ model [49] is a more recent development. It is modified from the standard $k - \epsilon$ model by replacing the equation for turbulent viscosity and the transport equation for dissipation rate, ϵ .

Transport equation of k and ϵ in the realizable $k - \epsilon$ model are

$$\begin{aligned} \frac{\partial}{\partial t}(\rho k) + \frac{\partial}{\partial x_j}(\rho k u_j) &= \frac{\partial}{\partial x_j} \left[\left(\mu + \frac{\mu_t}{\sigma_k} \right) \frac{\partial k}{\partial x_j} \right] \\ &+ G_k + G_b - \rho \epsilon - Y_M + S_k \end{aligned} \quad (16)$$

and

$$\begin{aligned} \frac{\partial}{\partial t}(\rho \epsilon) + \frac{\partial}{\partial x_j}(\rho \epsilon u_j) &= \frac{\partial}{\partial x_j} \left[\left(\mu + \frac{\mu_t}{\sigma_\epsilon} \right) \frac{\partial \epsilon}{\partial x_j} \right] \\ &+ \rho C_{1\epsilon} S_\epsilon - \rho C_2 \frac{\epsilon^2}{k + \sqrt{\nu \epsilon}} + C_{1\epsilon} \frac{\epsilon^2}{k} C_{3\epsilon} G_b + S_\epsilon \end{aligned} \quad (17)$$

where

$$C_1 = \max \left[0.43, \frac{\eta_\epsilon}{\eta_\epsilon + 5} \right], \eta_\epsilon = S \frac{k}{\epsilon}, S = \sqrt{2S_{ij}S_{ij}} \quad (18)$$

$C_{1\epsilon}$ and $C_{3\epsilon}$ are the model constants as the ones in Eq. (11). C_2 is a new model constant introduced in the realizable $k - \epsilon$ model. The k equation in the realizable model has the same form as that in other $k - \epsilon$ models. But the ϵ equation is modified. Eddy viscosity is computed as the same form of Equation (9). However, the value of C_μ in realizable $k - \epsilon$ model is no longer a constant. Instead, it is defined by

$$C_\mu = \frac{1}{A_0 + A_s \frac{kU^*}{\epsilon}} \quad (19)$$

where

$$U^* \equiv \sqrt{S_{ij}S_{ij} + \tilde{\Omega}_{ij}\tilde{\Omega}_{ij}} \quad (20)$$

and

$$\tilde{\Omega}_{ij} = \Omega_{ij} - 2\epsilon_{ijk}\omega_k \quad (21)$$

$$\Omega_{ij} = \overline{\Omega_{ij}} - 2\epsilon_{ijk}\omega_k \quad (22)$$

$$S_{ij} = \frac{1}{2} \left(\frac{\partial u_j}{\partial x_i} + \frac{\partial u_i}{\partial x_j} \right) \quad (23)$$

$\overline{\Omega_{ij}}$ is the mean rate-of-rotation tensor viewed in a rotating reference frame with the angular velocity ω_k . A_0 and A_5 are model constants.

The realizable model is improved in calculating the spreading rate of both planar and round jets. It also has better performance in modelling flows which involve rotation, boundary layers under strong adverse pressure gradients, separation, and recirculation. Initial studies have reported that the realizable model has the best performance in simulating separated flows and flows with complex secondary flow features among all the $k - \epsilon$ models [4].

3.2.2 $k - \omega$ Model

The $k - \omega$ model is also a commonly used two-equation model. The two additional transported variables in this model are the turbulent kinetic energy, k , and specific dissipation, ω . Specific dissipation defines the scale of turbulence. One of the advantages of $k - \omega$ model is its near wall treatment for low-Reynolds-number flows. The model is numerically robust and tends to produce converged solutions because it does not have a complex nonlinear damping function as is required by the $k - \epsilon$ model. Standard $k - \omega$ model and Shear-Stress Transport (SST) $k - \omega$ model are the two sub-models available in ANSYS Fluent.

The standard $k - \omega$ model [50] is based on the Wilcox $k - \omega$ model. Transport equations of turbulence kinetic energy, k , and the specific dissipation rate, ω , are defined as

$$\frac{\partial}{\partial t}(\rho k) + \frac{\partial}{\partial x_i}(\rho k u_i) = \frac{\partial}{\partial x_j} \left(\Gamma_k \frac{\partial k}{\partial x_j} \right) + G_k - Y_k + S_k \quad (24)$$

and

$$\frac{\partial}{\partial t}(\rho \omega) + \frac{\partial}{\partial x_i}(\rho \omega u_i) = \frac{\partial}{\partial x_j} \left(\Gamma_\omega \frac{\partial \omega}{\partial x_j} \right) + G_\omega - Y_\omega + S_\omega \quad (25)$$

where $\frac{\partial}{\partial t}(\rho k) + \frac{\partial}{\partial x_i}(\rho k u_i)$ is the rate of change in turbulent kinetic energy, $\frac{\partial}{\partial t}(\rho \omega) + \frac{\partial}{\partial x_i}(\rho \omega u_i)$ is the rate of change in specific dissipation, G_k is the turbulence kinetic energy generated due to mean velocity gradients. G_ω is the generation of ω . Γ_k

and Γ_ω are the effective diffusivity of k and ω respectively. Y_k and Y_ω are the dissipation of k and ω . S_k and S_ω are user-specified source terms.

The turbulent viscosity, μ_t , is computed by

$$\mu_t = \alpha^* \frac{\rho k}{\omega} \quad (26)$$

α^* is a coefficient for low-Reynolds-number correction. It is defined by

$$\alpha^* = \alpha_\infty^* \left(\frac{\alpha_0^* + Re_t/R_k}{1 + Re_t/R_k} \right) \quad (27)$$

$$Re_t = \frac{\rho k}{\mu \omega} \quad (28)$$

and in high-Reynolds-number situation, $\alpha^* = \alpha_\infty^* = 1$. R_k is a model related constant. The standard $k - \omega$ model also includes a coefficient for the production of ω , G_ω , and the dissipation of ω , Y_ω , which make the model suitable for modelling low-Reynolds-number flows.

The Shear-Stress Transport (SST) $k - \omega$ model [51] modifies the standard $k - \omega$ model so that the turbulent calculation changes gradually from the standard $k - \omega$ model in the region close to the boundary layer, to $k - \epsilon$ model in the far field. Meanwhile, calculation for turbulent viscosity is changed to include the transport effects of the principal turbulent shear stress.

The SST $k - \omega$ model has exact the same form of transport equation for k as that in standard $k - \omega$ model. The parameter for generation of turbulent kinetic energy, G_k , is replaced by \tilde{G}_k in the SST $k - \omega$ model. This new term of generated turbulence energy is defined as

$$\tilde{G}_k = \min(G_k, 10\rho\beta^*k\omega) \quad (29)$$

by replacing G_k with \tilde{G}_k , the SST $k - \omega$ model adds a limiter to the production term and tries to avoid the excessive generation of turbulence energy in stagnation regions near the boundary layers.

The transport equation for ω is changed by adding a cross-diffusion term, D_ω , which blends the standard $k - \omega$ model with the standard $k - \epsilon$ model.

Turbulent viscosity, μ_t , is defined in the SST $k - \omega$ model as

$$\mu_t = \frac{\rho k}{\omega} \frac{1}{\max\left[\frac{1}{\alpha^*}, \frac{SF}{\alpha_1 \omega}\right]} \quad (30)$$

S is the strain rate magnitude and F is a blending function which restricts the limiter included in the turbulent kinetic energy, \tilde{G}_k , to the wall boundary layer.

The SST $k - \omega$ model makes good use of the advantages of both standard $k - \omega$ model and standard $k - \epsilon$ model. By modifying the transport equations and including a blending function, the SST $k - \omega$ model is expected to perform more accurately and reliably for a wider class of turbulent problems.

3.2.3 Large Eddy Simulation (LES) Model

As mentioned earlier, to directly model eddies in turbulent flows, it is required that the calculation is based on a very fine mesh. This is because eddies which characterize the turbulent flows vary within a wide range of length and time scales. In this case the calculation process is computationally expensive. And in some practical engineering problems which involve high-Reynolds-number flows the computational cost can even be prohibitive. Large eddy simulation (LES) is a mathematical model that applies low-pass filtering to the Navier-Stokes equations, which then reduce the computational cost by ignoring the smallest eddies in turbulent flows. Only large eddies are solved in LES. Small eddies are modelled by using the subgrid-scale models (SGS model).

In LES, the time-dependent Navier-Stokes equations are filtered so that eddies smaller than the filter width or grid spacing are filtered out. Only the dynamics of large eddies are resolved. A filtered variable is defined by

$$\bar{\phi}(x) = \int_D \phi(x') G(x, x') dx' \quad (31)$$

where $\bar{\phi}$ is the filtered variable, D is the fluid domain, and G represent the filter function which filters out eddies smaller than a predefined scale.

Then the filtered Navier-stokes equations have the form as

$$\frac{\partial \rho}{\partial t} + \frac{\partial}{\partial x_i} (\rho \bar{u}_i) = 0 \quad (32)$$

and

$$\frac{\partial}{\partial t}(\rho \bar{u}_i) + \frac{\partial}{\partial x_j}(\rho \bar{u}_i \bar{u}_j) = \frac{\partial}{\partial x_j}(\sigma_{ij}) - \frac{\partial \bar{p}}{\partial x_i} - \frac{\partial \tau_{ij}}{\partial x_j} \quad (33)$$

here σ_{ij} denotes the stress tensor due to molecular viscosity which can be obtained by

$$\sigma_{ij} \equiv \left[\mu \left(\frac{\partial \bar{u}_i}{\partial x_j} + \frac{\partial \bar{u}_j}{\partial x_i} \right) \right] - \frac{2}{3} \mu \frac{\partial \bar{u}_i}{\partial x_i} \delta_{ij} \quad (34)$$

and τ_{ij} is the subgrid-scale stress defined by

$$\tau_{ij} \equiv \rho \bar{u}_i \bar{u}_j - \rho \bar{u}_i \bar{u}_j \quad (35)$$

ANSYS Fluent provides four models to take care of the subgrid-scale turbulent stresses. They are the Smagorinsky-Lilly model, the dynamic Smagorinsky-Lilly model, the WALE model, and the dynamic kinetic energy subgrid-scale model.

3.3 Models for Multiphase Fluid Flow

It is an essential yet challenging task for numerical modelling to capture the dynamic behaviour of liquid-gas interfaces appearing in an atomization process [11], [52]. Several numerical techniques have been developed specifically to handle the tasks for tracking complex interfaces [5], [11], [53]–[61]. The complexity in simulating multiphase flow is mainly induced by four reasons, which are:

- Interfaces between two immiscible fluids which affect the mass and momentum transport are not defined and are part of the solution [11].
- Usually large density, viscosity, and velocity ratios are observed between the two interacting fluids [11].
- Various physical reactions happen in a very short time span at the interfacial area [52].
- Discrete-phase volume fraction varies from close to 100 % in bulk liquid stream to less than 5 % in dispersed droplets, which requires different mathematical model to describe the multiphase interaction.

In ANSYS Fluent, four different models are available for modelling multiphase flow. They are the Volume of Fluid (VOF) Model, the Mixture Model, the Eulerian Model, and the Discrete Phase Model (DPM). The VOF Model is designed for tracking the position of interfaces between two or more immiscible fluids. It is appropriate for

studying stratified flows, free-surface flows, filling, sloshing, etc. [5]. In Mixture Model and Eulerian Model, different phases are treated as interpenetrating continua. Multiphase interaction is modelled in the Mixture Model by solving a mixture momentum equation and prescribing slip velocities of dispersed phases [5]. While in the Eulerian Model, momentum and continuity equations are solved for each phase then the solutions of phases are coupled by pressure and interphase exchange coefficients. Mixture Model and Eulerian Model are targeting similar flow regimes which include bubbly, droplet, and particle-laden flows, slurry flows, hydro-transport, etc. [5]. The Eulerian Model is also applicable for modelling granular flow which is beyond the capability of Mixture Model.

Although multiphase interactions and movements in wide range of flow regimes can be described and captured by the models above, they still cannot satisfy the need to model the effect of turbulent flow of continuous phase on the smallest droplets. All three models are limited in that they can only be used in situations where dispersed-phase volume fractions exceed 10 % [5]. For particle dynamics of dispersed small droplets surrounded by air streams, Discrete Phase Model (DPM) is especially competent. DPM model is an Euler-Lagrange approach which treats the fluid phase as a continuum and the dispersed phase as discrete particles, bubbles, or droplets [5]. Navier-Stokes equations are solved in the continuous phase and the particle trajectories are computed. The model is suitable for modelling spray dryers, coal and liquid fuel combustion, and some particle-laden flows [5].

3.3.1 Volume of Fluid (VOF) Model

In the VOF model, it is assumed that no interpenetration happens between fluids. Each of the introduced phases has its own indicator of volume fraction in a numerical cell. For each cell, volume fraction of all fluids sum to unity. Fields of variables and properties in the calculation domain are assigned as volume-averaged values. Any one of the cells is either fully occupied by one of the phases, or by a mixture of phases, which is indicated by the volume fraction value. For example, in the case in which f_n represents the n^{th} fluid's volume fraction in a cell of interest, three possible situations that could happen:

- $f_n = 0$: There is no n^{th} in the cell.

- $0 \leq f_n \leq 1$: The cell contains the interface between the n^{th} fluid and other fluids.
- $f_n = 1$: The cell is fully occupied by the n^{th} fluid and there is no other fluid in this cell.

The values of volume fractions also facilitate the tracking of interfaces in the VOF model. The continuity equation for the volume fraction of n^{th} fluid is established in the model with the form of:

$$\frac{1}{\rho_n} \left[\frac{\partial(f_n \rho_n)}{\partial t} + \nabla \cdot (f_n \rho_n \vec{v}_n) = S_{f_n} + \sum_{l=1}^{\omega} (\dot{m}_{ln} - \dot{m}_{nl}) \right] \quad (36)$$

where $\frac{\partial(f_n \rho_n)}{\partial t} + \nabla \cdot (f_n \rho_n \vec{v}_n)$ is the rate of change in volume fraction, \dot{m}_{ln} denotes the mass transfer from phase l to phase n and \dot{m}_{nl} represents the mass transfer from phase n to phase l . S_{f_n} is the source term.

As was previously described, properties in each of the numerical cells are calculated as volume-averaged values. Taking density as an example, in a two-phase flow, density in every cell can be presented as

$$\rho = f_2 \rho_2 + (1 - f_2) \rho_1 \quad (37)$$

here, the subscripts of 1 and 2 denote different phases. All other properties are computed in the same way.

In the VOF multiphase model, only one momentum equation is solved and all the phases share the resulting velocity field. Volume fractions of phases affect the momentum equation shown in Equation (38) through the averaged material properties ρ and μ .

$$\frac{\partial}{\partial t} (\rho \vec{v}) + \nabla \cdot (\rho \vec{v} \vec{v}) = -\nabla p + \nabla \cdot [\mu(\nabla \vec{v} + \nabla \vec{v}^T)] + \rho \vec{g} + \vec{F} \quad (38)$$

The shared-fields approximation does not work very well in situations where velocity differences between phases are large. This limits the application of the VOF model.

3.3.2 Mixture Model

The Mixture model also adopts a single-fluid approach. However this model allows interpenetrating between phases and it also allows phases to move at different speeds. In order to capture the multiphase interactions, equations of momentum, continuity,

and energy for the mixture are solved. Additionally, volume fraction equations for the secondary phases, and algebraic expressions for the relative velocities are also taken care of. The continuity equation for the mixture can be given as

$$\frac{\partial}{\partial t} (\rho_m) + \nabla \cdot (\rho_m \vec{v}_m) = 0 \quad (39)$$

where \vec{v}_m is the mass-averaged velocity which is calculated as

$$\vec{v}_m = \frac{\sum_{l=1}^{\omega} f_l \rho_l \vec{v}_l}{\rho_m} \quad (40)$$

and ρ_m is the density of mixture:

$$\rho_m = \sum_{l=1}^{\omega} f_l \rho_l \quad (41)$$

with f_l representing the volume fraction of phase l .

Contributed by individual momentum equations of all phases, the momentum equation in the Mixture model has the form of

$$\begin{aligned} \frac{\partial}{\partial t} (\rho_m \vec{v}_m) + \nabla \cdot (\rho_m \vec{v}_m \vec{v}_m) = & -\nabla p + \nabla \cdot [\mu_m (\nabla \vec{v}_m + \nabla \vec{v}_m^T)] + \\ & \rho_m \vec{g} + \vec{F} + \nabla \cdot \left(\sum_{l=1}^{\omega} f_l \rho_l \vec{v}_{dr,l} \vec{v}_{dr,l} \right) \end{aligned} \quad (42)$$

here ω represents the total number of phases, \vec{F} denotes the body force, and μ_m is the viscosity of the mixture and is calculated in the same way as the density of mixture. $\vec{v}_{dr,l}$ is the drift velocity for the secondary phase l which is expressed as

$$\vec{v}_{dr,l} = \vec{v}_l - \vec{v}_m \quad (43)$$

In the Mixture model, the velocity of a secondary phase (s), \vec{v}_s , relative to the velocity of the primary phase (p), \vec{v}_p , defines the slip velocity:

$$\vec{v}_{sp} = \vec{v}_s - \vec{v}_p \quad (44)$$

The mass fraction of any phase l can be expressed as

$$c_l = \frac{f_l \rho_l}{\rho_m} \quad (45)$$

The drift velocity and the relative velocity can be defined as

$$\vec{v}_{dr,s} = \vec{v}_{sp} - \sum_{l=1}^{\omega} C_l \vec{v}_{pl} \quad (46)$$

Volume fraction of the n^{th} phase can be obtained based on the continuity equation

$$\frac{\partial}{\partial t} (f_n \rho_n) + \nabla \cdot (f_n \rho_n \vec{v}_m) = -\nabla \cdot (f_n \rho_n \vec{v}_{dr,n}) + \sum_{l=1}^{\omega} (\dot{m}_{ln} - \dot{m}_{nl}) \quad (47)$$

The main differences between Equation (36) of VOF model and Equation (47) of Mixture model are:

- Equation (47) considers relative velocities between primary phase and secondary phases while Equation (36) sees all the phases moving at the same velocities.
- Fields of variables and properties in Equation (36) are based on volume-averaged values while fields in Equation (47) are calculated from mass-averaged values.

3.3.3 Eulerian Multiphase Model

The Eulerian model is the most complex multiphase model in ANSYS Fluent. In this model, field of pressure in the calculation domain is shared by all phases and equations of momentum and continuity are solved separately for each phase. For phase n , the continuity equation is

$$\frac{\partial (f_n \rho_n)}{\partial t} + \nabla \cdot (f_n \rho_n \vec{v}_n) = \sum_{l=1}^{\omega} (\dot{m}_{ln} - \dot{m}_{nl}) + S_n \quad (48)$$

The momentum balance for n^{th} phase is expressed as

$$\begin{aligned} \frac{\partial}{\partial t} (f_n \rho_n \vec{v}_n) + \nabla \cdot (f_n \rho_n \vec{v}_n \vec{v}_n) = & -f_n \nabla p + \vec{F} + \\ \nabla \cdot [f_n \mu_n (\nabla \vec{v}_n + \nabla \vec{v}_n^T)] + f_n \rho_n \vec{g} + \sum_{l=1}^{\omega} & (\vec{R}_{ln} + \dot{m}_{ln} \vec{v}_{ln} - \dot{m}_{nl} \vec{v}_{nl}) \end{aligned} \quad (49)$$

where \vec{R}_{ln} represents the interaction force between phases and p is the pressure shared by all phases. \vec{v}_{ln} denotes the interphases velocity. In the situation where phase l mass is transferred to phase n , $\dot{m}_{ln} > 0$, $\vec{v}_{ln} = \vec{v}_l$; if mass of phase n is transferred to phase l , then $\dot{m}_{ln} < 0$, $\vec{v}_{ln} = \vec{v}_n$. Likewise, if $\dot{m}_{nl} > 0$, $\vec{v}_{nl} = \vec{v}_n$; if $\dot{m}_{nl} < 0$, $\vec{v}_{nl} = \vec{v}_l$.

The Eulerian model couples momentum and continuity equations for each phase by the share field of pressure p and interphase force \vec{R}_{ln} . An appropriate expression for \vec{R}_{ln} must be used so that the conservation of momentum can be closed. Friction, pressure, cohesion, etc. affect the interphase force. In Fluent, the interaction force is given as

$$\sum_{l=1}^{\omega} \vec{R}_{ln} = \sum_{l=1}^{\omega} K_{ln} (\vec{v}_l - \vec{v}_n) \quad (50)$$

where K_{ln} is the interphase momentum exchange coefficient. This parameter is influenced by volume fraction and density of the predominant phase, volume fraction, density and diameter of the sparser phase, and the drag force.

The Eulerian model solves equations of continuity and momentum for all phases, which obviously requires more computational effort compared to the Mixture model. This model, in principal, has no limitation on the number of secondary phases. However, the actual number of secondary phases is limited by memory requirements and convergence behaviour. When there is a wide distribution of the particulate phase in the calculation domain or when the interphase laws are unclear, simulations using the full multiphase Eulerian model may be less reliable. An alternative multiphase model like the Mixture model can execute as well as the Eulerian model by considering fewer variables.

3.3.4 Discrete Phase Model (DPM)

Different from the three described multiphase models which follow the Euler-Euler approach, the DPM model adopts the Euler-Lagrange approach. Fluid phase in the calculation domain is treated as a continuum and the Navier-Stokes equations are solved. For the dispersed phase, the model treats it as discrete particles, bubbles, or droplets and their movements in the fluid flow are tracked. Momentum, mass, and energy in the dispersed phase can be exchanged with the fluid phase. Particle-particle interactions are neglected, which requires a low volume fraction of the second phase.

Trajectory of a discrete phase particle (or droplet or bubble) is calculated by considering the force balance on that particle. In a Lagrangian reference frame, the force balance equation on a particle can be given as

$$\frac{d\vec{u}_p}{dt} = \frac{\vec{u} - \vec{u}_p}{\tau_r} + \frac{\vec{g}(\rho_p - \rho)}{\rho_p} + \vec{F} \quad (51)$$

\vec{F} is an additional acceleration term which is affected by gravitational, “virtual mass”, thermophoretic, Brownian, and Saffman’s lift forces. $\frac{\vec{u} - \vec{u}_p}{\tau_r}$ represents the drag force acting on per unit particle mass. \vec{u} denotes the fluid phase velocity, \vec{u}_p represents the particle velocity, ρ_p and ρ are the densities for fluid and particle respectively. τ_r is the droplet or particle relaxation time and is defined as

$$\tau_r = \frac{\rho_p d_p^2}{18\mu} \frac{24}{C_d Re} \quad (52)$$

here μ is the molecular viscosity of the fluid, d_p is the particle diameter, and Re is the relative Reynolds number which is expressed as

$$Re \equiv \frac{\rho d_p |\vec{u}_p - \vec{u}|}{\mu} \quad (53)$$

The DPM model is appropriate for flows in which the dispersed-phase volume fractions are less than 10%. It is particularly useful for studying multiphase interaction in the spray regime which is very difficult to capture by using the other three multiphase models. Besides, the DPM model can be used to study droplet dynamics including droplet breakup, collisions, and coalescence in the atomization process. Models for studying droplet dynamics will be present in the following section.

3.4 Models for Droplet Breakup, Collision, and Coalescence

Apart from tracking the movements and positions of discrete phase particles, the DPM model is also capable of capturing particle dynamics including breakup, collision, and droplet coalescence in the atomization process, which is very important for predicting the produced droplet sizes and distributions.

3.4.1 Models for Droplet Breakup

There are four models that are available in ANSYS Fluent for modelling droplet breakup. They are the Taylor Analogy Breakup (TAB) model, Wave model, KHRT model, and Stochastic Secondary Droplet (SSD) model.

The Taylor Analogy Breakup (TAB) Model [62] is a classical model for droplet breakup in low-Weber-number sprays. Oscillations and distortions of droplet are studied in the model and once the droplet oscillations reach a critical value, “parent” droplets will separate into a number of smaller “child” droplets. The damped, forced oscillator can be expressed as [4], [63]

$$F_d - k_d x - d \frac{dx}{dt} = m \frac{d^2 x}{dt^2} \quad (54)$$

x is the displacement of the droplet equator from its spherical (undisturbed) position. m , F_d , k_d , and d are mass, force, spring constant, and damping constant. Their value can be taken from Taylor’s analogy:

$$\frac{F_d}{m} = C_F \frac{\rho_g u^2}{\rho_l r} \quad (55)$$

$$\frac{k_d}{m} = C_k \frac{\sigma}{\rho_l r^3} \quad (56)$$

$$\frac{d}{m} = C_d \frac{\mu_l}{\rho_l r^2} \quad (57)$$

ρ_l and ρ_g represent the discrete phase and continuous phase densities, u denotes the relative velocity of the droplet, r is the radius of droplet at its undisturbed position, σ is the droplet surface tension, and μ_l stands for the droplet viscosity. C_F , C_k , and C_d are dimensionless constants which is defined based on experiments and theory. Break up is assumed to take place once the distortion on a droplet grows to a critical ratio of the radius of that droplet, which is presented as

$$x > C_b r \quad (58)$$

C_b is a constant defined as 0.5 if the droplet is assumed to breakup at the situation when distortion proceeds to half the droplet radius. Setting $y = x/(C_b r)$ and substituting the relationships in Equation (55) - (57), Equation (54) is nondimensionalized as

$$\frac{d^2 y}{dt^2} = \frac{C_F \rho_g u^2}{C_b \rho_l r^2} - \frac{C_k \sigma}{\rho_l r^3} y - \frac{C_d \mu_l}{\rho_l r^2} \frac{dy}{dt} \quad (59)$$

In this deduced equation, the droplet collapses when $y > 1$. Assuming that the relative velocity is constant, y can be determined from

$$y(t) = We_c + e^{-\left(\frac{t}{t_d}\right)} \left[(y_0 - We_c) \cos(\omega t) + \frac{1}{\omega t} \left(\frac{dy_0}{dt} + \frac{y_0 - We_c}{t_d} \right) \sin(\omega t) \right] \quad (60)$$

where

$$We = \frac{\rho_g u^2 r}{\sigma} \quad (61)$$

$$We_c = \frac{C_F}{C_k C_b} We \quad (62)$$

$$y_0 = y(0) \quad (63)$$

$$\frac{dy_0}{dt} = \frac{dy}{dt} (0) \quad (64)$$

$$\frac{1}{t_d} = \frac{C_d \mu_l}{2 \rho_l r^2} \quad (65)$$

$$\omega_d^2 = C_k \frac{\sigma}{\rho_l r^3} - \frac{1}{t_d^2} \quad (66)$$

here u is the relative velocity and We is the droplet Weber number which is the ratio of aerodynamic forces to surface tension forces. ω_d denotes the droplet oscillation frequency. Based on the work of Liu et al., y_0 has a default value of 0. The value of C_F , C_k , and C_d can now be defined as

$$C_k = 8 \quad (67)$$

$$C_d = 5 \quad (68)$$

and

$$C_F = \frac{1}{3} \quad (69)$$

The size of child droplets is calculated by equalling the combined energy of child droplets to the energy of the parent droplet, which can be given as

$$E_{parent} = 4\pi r^2 \sigma + K \frac{\pi}{5} \rho_l r^5 \left[\left(\frac{dy}{dt} \right)^2 + \omega_d^2 y^2 \right] \quad (70)$$

K is the ratio of the total energy in distortion and oscillation to the energy in the fundamental mode. Energy of child droplets are expressed as

$$E_{child} = 4\pi r^2 \sigma \frac{r}{r_{32}} + \frac{\pi}{6} \rho_l r^5 \left(\frac{dy}{dt} \right)^2 \quad (71)$$

by equating the energy of the parent droplet and child droplets, Sauter mean radius, r_{32} , can be obtained:

$$r_{32} = \frac{r}{1 + \frac{8Ky^2}{20} + \frac{\rho_l r^3 \left(\frac{dy}{dt} \right)^2}{\sigma} \left(\frac{6K - 5}{120} \right)} \quad (72)$$

Mass conservation of droplets is used to determine the number of child droplets when the size of child droplets is obtained.

Wave Breakup Model [64] assumes that droplet disintegrates as a result of relative velocity between gas and liquid phases. The model is suitable for atomization relating to high-Weber-number flow ($We > 100$) and high-speed injection. Time of breakup and size of child droplets are affected by Kelvin – Helmholtz instability which can be described by jet stability analysis. In the analysis, a cylindrical, viscous, liquid jet of radius a at velocity v is injected from an orifice into a stagnant, incompressible, inviscid gas. The gas has a density of ρ_2 while the liquid has a density, ρ_1 , and viscosity, μ_1 . Using a cylindrical polar coordinate system which moves with the jet, an arbitrary axisymmetric surface displacement imposed on the initially steady motion can be expressed as

$$\eta = \eta_0 e^{ik_W z + \omega_W t} \quad (73)$$

The relationship between the real part of the growth rate, ω_W , and the wave number, $k_W = 2\pi/\lambda$, is desired to be obtained.

Assuming the wave solutions have the form

$$\phi_1 = C_{1w} I_0(kr) e^{ik_W z + \omega_W t} \quad (74)$$

$$\psi_1 = C_{2w} I_1(Lr) e^{ik_W z + \omega_W t} \quad (75)$$

where ϕ_1 and ψ_1 represent the velocity potential and stream function. C_{1w} , C_{2w} are integration constants, I_0 , I_1 are modified Bessel functions of the first kind, $L^2 = k_W^2 + \omega_W/v_1$ and v_1 is the liquid kinematic viscosity. Liquid pressure, p_1 , can be solved from the liquid equation and the fluctuating gas pressure at $r = a$ can be obtained by solving the equation for inviscid gas (viscosity is negligible):

$$-p_{21} = -\rho_2(u - i\omega_W k_W)^2 k_W \eta \frac{K_0(k_W a)}{K_1(k_W a)} \quad (76)$$

where K_0 and K_1 are modified Bessel functions of the second kind and u denotes the velocity difference between liquid and gas. Linearized boundary conditions of liquid kinematic free surface, continuity of shear stress, and continuity of normal stress can be formulated as

$$v_1 = \frac{\partial \eta}{\partial t} \quad (77)$$

$$\frac{\partial u_1}{\partial r} = -\frac{\partial v_1}{\partial z} \quad (78)$$

and

$$-p_1 + 2\mu_1 - \frac{\sigma}{a^2} \left(\eta + a^2 \frac{\partial \eta}{\partial z^2} \right) + p_2 = 0 \quad (79)$$

where u_1 and v_1 are axial perturbation velocity and radial perturbation velocity for liquid. σ is the surface tension. To obtain Equation (78), radial perturbation velocity of gas, v_2 , is assumed to be 0.

The linearized boundary conditions can be used to eliminate the integration constants C_{1w} , and C_{2w} in velocity potential and stream function. The desired dispersion relation between ω_W and k_W is obtained by substituting the pressure and velocity solutions into Equation (79):

$$\begin{aligned} \omega_W^2 + 2v_1 k_W^2 \omega_W \left[\frac{I'_1(k_W a)}{I_0(k_W a)} - \frac{2k_W L}{k_W^2 + L^2} \frac{I_1(k_W a)}{I_0(k_W a)} \frac{I'_1(La)}{I_1(La)} \right] \\ = \frac{\sigma k_W}{\rho_1 a^2} (1 - k_W^2 a^2) \left(\frac{L^2 - a^2}{L^2 + a^2} \right) \frac{I_1(k_W a)}{I_0(k_W a)} + \\ \frac{\rho_2}{\rho_1} \left(u - i \frac{\omega_W}{k_W} \right)^2 \left(\frac{L^2 - a^2}{L^2 + a^2} \right) \frac{I_1(k_W a)}{I_0(k_W a)} \frac{K_0(k_W a)}{K_1(k_W a)} \end{aligned} \quad (80)$$

Given a set of flow conditions Equation (80) can be used to predict the most unstable wave. Maximum growth rate, Ω , and the corresponding wavelength, Λ , are given by Reitz:

$$\frac{\Lambda}{a} = 9.02 \frac{(1 + 0.45Oh^{0.5})(1 + 0.4Ta^{0.7})}{(1 + 0.87We_2^{1.67})^{0.6}} \quad (81)$$

$$\Omega \sqrt{\frac{\rho_1 a^3}{\sigma}} = \frac{0.34 + 0.38 We_2^{1.5}}{(1 + Oh)(1 + 1.4 Ta^{0.6})} \quad (82)$$

Oh is the Ohnesorge number which can be calculated as $\sqrt{We_1}/Re_1$. Ta is the Taylor number and is calculated as $Oh\sqrt{We_2}$. We_1 and We_2 are Weber numbers for liquid and gas which are obtained from $\rho_1 u^2 a/\sigma$ and $\rho_2 u^2 a/\sigma$ respectively. $Re_1 = ua/\nu_1$ is the Reynolds number.

In the Wave model the radius of generated child droplets is assumed to be proportional to the wavelength of the fastest-growing unstable surface wave on the parent droplet, which gives

$$r = B_0 \Lambda \quad (83)$$

Based on the work of Reitz [64] model constant, B_0 , is set as 0.61. Expression for the rate of change of droplet radius in parent parcel is

$$\frac{da}{dt} = -\frac{(a-r)}{\tau}, r \leq a \quad (84)$$

where τ is the breakup time and can be expressed as

$$\tau = \frac{3.726 B_1 a}{\Lambda \Omega} \quad (85)$$

B_1 is the breakup time constant which has a range from 1 to 60. According to the work by Liu et al [65], value of B_1 is recommended to be 1.73.

In the wave model a new parcel is created when the shed mass accumulated from parent drops reach 5% of the initial parcel mass. The newly generated parcel shares the properties like temperature, material, position, etc. with the parent parcel. Parcel radius and velocity are updated.

KHRT Breakup Model [66], [67] is a model that improves the Wave Breakup Model by combining it with Rayleigh-Taylor instabilities due to acceleration of shed drops ejected into freestream conditions. Wave growth on the surface of the droplet is of the most concern in this model and breakup happens when the fastest growing instability is reached. This model is applicable for high-Weber-number sprays.

In KHRT model, child droplets separate from the liquid core which is assumed to exist close to the nozzle region. Droplet breakup within the liquid core is modelled by using the Wave Breakup Model. For breakup happening outside the liquid core both Kelvin-Helmholtz and Rayleigh-Taylor instabilities are considered. For high-Weber-number flow, distortion on the droplet is dominantly affected by Rayleigh-Taylor

instability. This is because Rayleigh-Taylor instability grows faster on droplet with high acceleration than Kelvin-Helmholtz instability. According to Levich theory [68]:

$$L = C_L d_0 \sqrt{\frac{\rho_l}{\rho_g}} \quad (86)$$

L is the length of the modelled liquid core, C_L is the Levich constant and d_0 denotes a reference nozzle diameter.

Rayleigh-Taylor instability is wave instability on the droplet surface. The frequency of the fastest growing wave is given by

$$\Omega_{RT} = \sqrt{\frac{2(-g_t(\rho_p - \rho_g))^{3/2}}{3\sqrt{3}\sigma(\rho_p + \rho_g)}} \quad (87)$$

where g_t is the acceleration of the droplet in its traveling direction. The corresponding wave number is expressed as

$$K_{RT} = \sqrt{\frac{-g_t(\rho_p - \rho_g)}{3\sigma}} \quad (88)$$

and the breakup time τ_{RT} is defined as

$$\tau_{RT} = \frac{C_\tau}{\Omega_{RT}} \quad (89)$$

where C_τ is the Rayleigh-Taylor breakup time constant. If a wave on droplet grows for a time longer than τ_{RT} , breakup occurs.

Stochastic Secondary Droplet (SSD) Model [69] described droplet breakup as a discrete random event which produces droplets with diameters over a range.

In this model, breakup happens when drops are larger than a critical radius:

$$r_c = \frac{We_{cr}\sigma_l}{\rho_g u_{rel}^2} \quad (90)$$

We_{cr} is the critical Weber number, σ_l is the surface tension of liquid, and u_{rel} is the relative velocity between the gas and the droplet.

The breakup time is formulated as

$$t_{bu} = B \sqrt{\frac{\rho_l}{\rho_g} \frac{r}{|u_{rel}|}} \quad (91)$$

here B is the breakup constant. Breakup occurs if the breakup time on the parcel is larger than the critical breakup time. In this case, the old parcel is deleted and child

parcels are created. Diameters of the newly formed droplets are calculated by sampling a distribution function in the log of the diameter, $x = \ln r$:

$$T(x) = \frac{1}{\sqrt{2\pi\langle\xi^2\rangle}} \exp\left[\frac{-(x - x_0 - \langle\xi\rangle)^2}{2\langle\xi^2\rangle}\right] \quad (92)$$

here $\langle\xi\rangle$ is a user-specified parameter and $\langle\xi^2\rangle$ is computed from $\langle\xi^2\rangle = -0.1 \ln\left(\frac{We_{cr}}{We}\right)$.

After all the new parcels are generated, which use up the mass of the parent parcel, a scaling factor is applied to the drop number in all the child parcels to make sure mass between parent and child parcels is conserved.

3.4.2 Models for Collision and Droplet Coalescence

ANSYS Fluent is capable of modelling droplet collisions and their outcomes. O'Rourke's algorithm [70] is adopted to capture droplet collision.

In this algorithm, collision only happens when two droplets are in the same continuous – phase cell. Probability of collision of two droplets is modelled based on the droplet with larger diameter. Because the reference frame for calculation is built on the larger droplet, its velocity is set as 0. Relative distance between the larger droplet, called collector droplet, and the smaller droplet is a very important parameter in this algorithm. Collision will happen if the centre of smaller droplet passes within a flat circular area of $\pi(r_1 + r_2)^2$ around the collector and perpendicular to the direction that the smaller droplet travels. Here r is radius of droplets, subscript number 1 marks properties of the collector droplet, and subscript number 2 identifies properties of the smaller droplet. Moreover, a collision volume can be defined by multiplying the circular area by the distance travelled by the small droplet in 1 time step, which is $\pi(r_1 + r_2)^2 v_2 \Delta t$. This collision volume is then used to calculate the probability of collision. The chance of the smaller droplet being within the collision volume of the collector is calculated by the algorithm. A smaller droplet exists in the continuous-phase cell of volume V and the probability for this droplet to be anywhere within the volume is even. So the opportunity of a droplet appearing within the collision volume of the collector is the ratio between volume of collision and volume of continuous – phase cell, which is

$$P_1 = \frac{\pi(r_1 + r_2)^2 v_{rel} \Delta t}{V} \quad (93)$$

If the collector and smaller droplet parcels have n_1 and n_2 droplets respectively, the mean expected number of collisions of collector can be defined by

$$\bar{n} = \frac{n_2 \pi (r_1 + r_2)^2 v_{rel} \Delta t}{V} \quad (94)$$

The actual number of collisions obeys a Poisson distribution. According to O'Rourke, the probability distribution of the number of collisions is given by

$$P(n_s) = e^{-\bar{n}} \frac{\bar{n}^{n_s}}{n_s!} \quad (95)$$

here n_s is the number of collisions between a collector and other droplets

There are two possible outcomes once the collision of parcels is confirmed. The two parcels will either combine into one if they bump into each other directly, or they will separate again if the collision is oblique. Probability of coalescence is related to the offset of the centre of the collector droplet and the trajectory of the smaller droplet. According to O'Rourke, critical offset can be given by

$$b_{crit} = (r_1 + r_2) \sqrt{\min\left(1.0, \frac{2.4f}{We}\right)} \quad (96)$$

here f is a function of r_1/r_2 , which can be calculated by

$$f\left(\frac{r_1}{r_2}\right) = \left(\frac{r_1}{r_2}\right)^3 - 2.4\left(\frac{r_1}{r_2}\right)^2 + 2.7\left(\frac{r_1}{r_2}\right) \quad (97)$$

The outcome of collision is determined by comparing the actual collision parameter, b , with the critical offset, b_{crit} . The value of b is obtained by

$$b = (r_1 + r_2) \sqrt{Y} \quad (98)$$

where Y is a random number between 0 and 1. If $b < b_{crit}$, parcels combine after the collision. Basic conservation laws are applied to calculate the properties of newly – formed coalesced droplets.

3.5 Summary of CFD Models and Challenges for Modelling Atomization

This chapter presented some numerical theories regarding basics of CFD and models for turbulence, multi-phase flow, and droplet dynamics. Information for different

models is briefly summarized in Table 3-1, Table 3-2, and Table 3-3. Although a lot of models have been developed [4], [62], [64]–[70] and are accessible from ANSYS Fluent for problems of different flow regimes, there is no universal algorithm that can be used for modelling the atomization process from internal nozzle flow to external droplet-cloud dynamic. Modelling the whole atomization process remains a challenge for both academic research and engineering calculation. This is because the process involves a dramatic change of the volume fraction in the calculation domain, big differences in properties and field of variables between interaction phases, and varying length scale of interest for internal and external flows. Despite the extensive effort for developing new mathematical models [6], [26]–[28], [71]–[80], no model is reliable enough for engineering calculations.

Comparing different turbulent models in Table 3-1, realizable $k - \epsilon$ model is the most suitable model for studying the atomization process. DNS model is too computationally expensive and not practical for engineering calculation. Standard $k - \epsilon$ model and RNG $k - \epsilon$ model are mainly for flows with high Reynolds numbers. While fluid flows inside nozzle body have a low Reynolds numbers close to the internal walls and have high Reynolds numbers at unbounded areas. $k - \omega$ Models are generally for flows with low Reynolds numbers. Although the LES method reduces the computational cost of DNS method by filtering the smallest eddies, the model still requires considerable computational effort if an accurate result is expected. The realizable $k - \epsilon$ model finds a good balance between calculation accuracy and consumed effort. It has been extensively validated for flows with a wide range of Reynolds numbers.

For multiphase models listed in Table 3-2, VOF model is not suitable for flows with large velocity differences between phases, whereas liquid is separated by a high-speed air stream in the multiphase atomization process. Both the Mixture model and the Eulerian model are capable of modelling flows with relative velocities. The Eulerian model is the most complicated model for multiphase flow in Fluent. However, it solves equations of momentum and continuity separately for each phase, which makes it computationally expensive. These three models are only valid for flows with dispersed-phase volume fractions more than 10% which are not satisfied in the spray regime. The DPM model works well in flows with dispersed-phase volume fractions less than 10%. It is particularly useful for studying multiphase interaction in the spray

regime. Both the Mixture multiphase model and DPM model are suitable for modelling the atomization process but they should be separated in different steps with the focus on different spray characteristics.

To model droplet breakup and coalescence, droplet breakups in sprays are caused either by large velocity differences between gas and liquid phases at the core of the sprays or by Rayleigh-Taylor instabilities on shed droplets outside the core. The TAB model is only applicable for situations where Weber numbers are low. The Wave Breakup Model only accounts for breakups caused by velocity difference. The KHRT Model which takes both effects into consideration is the most suitable for the study of multiphase atomization. The SSD model considers droplet breakup as a random event which is not suitable for studying atomization. The default collision and coalescence model is applicable since droplet bouncing and coalescence are the main consequences after droplet collisions.

Table 3-1 Models for Turbulent Fluctuation

Models for Turbulent Fluctuation			
Name	Description	Requirement	Remark
Direct numerical simulation (DNS)			
Direct numerical simulation (DNS)	Solves the transported quantities affected by the fluctuating velocity and pressure directly.	<ul style="list-style-type: none"> • Size of the mesh needs to be finer than the length scale of the smaller turbulent eddies • Numerical time step needs to be smaller than the time scale of turbulent fluctuations 	This method is too computationally expensive and not practical for engineering calculations.
<i>k</i> – ϵ Model			
Standard <i>k</i> – ϵ model	Two separate transport equations to independently	<ul style="list-style-type: none"> • Solving the transport equations for turbulence kinetic energy and rate of dissipation to calculate 	The standard <i>k</i> – ϵ model assumes that the flow is fully turbulent.

	determine the turbulent velocity and length scales.	the turbulent velocity and length scales	
RNG $k - \epsilon$ model	RNG $k - \epsilon$ model refines the standard model.	<ul style="list-style-type: none"> • Solving the transport equations for turbulence kinetic energy and rate of dissipation • Solving analytically-derived differential formula for effective viscosity that accounts for low-Reynolds-number effects to enhance the standard model 	The model is more applicable for low-Reynolds-number and near-wall flows.
Realizable $k - \epsilon$ model	This model is modified from the standard $k - \epsilon$ model by replacing the equation for turbulent viscosity and the transport equation for dissipation rate ϵ .	<ul style="list-style-type: none"> • Solving the transport equations for turbulence kinetic energy and rate of dissipation. • Including new formulation for turbulent viscosity where C_μ is no longer a constant 	This model has been extensively validated for a wide range of flows. It provides the best performance of all the $k - \epsilon$ models.
$k - \omega$ Model			
standard $k - \omega$ model	Two additional transported variables in this model are	<ul style="list-style-type: none"> • Solving the transport equations for turbulence kinetic energy and rate of dissipation to calculate 	This model has advantages in near wall treatment for low-Reynolds-

	turbulent kinetic energy and specific dissipation.	the turbulent time and length scales	number flows.
Shear-Stress Transport (SST) $k - \omega$ model	Modified from standard $k - \omega$ model. It changes gradually from standard $k - \omega$ model in the region close to the boundary layer to $k - \epsilon$ model in the far field.	<ul style="list-style-type: none"> Solving the transport equations for turbulence kinetic energy and rate of dissipation Calculation for turbulent viscosity is changed to include the transport effects of the principal turbulent shear stress 	This model makes good use of the advantages of both standard $k - \omega$ model and standard $k - \epsilon$ model. It is expected to perform more accurately and reliably for a wider class of turbulent problems.

Large Eddy Simulation (LES) Model

Large Eddy Simulation (LES) Model	This model applies low-pass filtering to the Navier-Stokes equations, which then reduce the computational cost by ignoring smallest eddies in turbulent flows.	<ul style="list-style-type: none"> Solving the Navier-stokes equations for large eddies Small eddies are modelled by using the subgrid-scale models 	Although the model is less computationally expensive than the DNS model. The results still depend on the grid size, which make it not practical engineering calculations.
-----------------------------------	--	---	---

Table 3-2 Models for Multiphase Fluid Flow

Models for Multiphase Fluid Flow			
Name	Description	Requirement	Remark

<p>Volume of Fluid (VOF)</p>	<p>The model assumes that no interpenetration happens between fluids.</p>	<ul style="list-style-type: none"> • Calculating the volume fraction of each phase in every numerical cell, for each cell, volume fraction of all fluids sum to unity • Assigning Fields of Variables and properties in the calculation domain as volume-averaged values • One momentum equation is solved and all the phases share the resulting velocity field 	<p>Designed for tracking the position of interfaces between immiscible fluids, this model is appropriate for studying stratified flows, free-surface flows, filling, sloshing, etc. The shared-fields approximation does not work very well in situations where velocity differences between phases are large. This limits the application of the VOF model.</p>
<p>Mixture Model</p>	<p>This model allows interpenetrating between phases and it also allows phases to move at different speeds.</p>	<ul style="list-style-type: none"> • Modelling multiphase interaction by solving a mixture momentum equation and prescribing slip velocities of dispersed phases • Considering relative velocities between primary phase and secondary phases • Calculating Fields of variables and properties from mass-averaged values 	<p>This model treats different phases as interpenetrating continua. This model targets bubbly, droplet, and particle-laden flows, slurry flows, etc.</p>
<p>Eulerian Model</p>	<p>This model allows</p>	<ul style="list-style-type: none"> • Sharing field of pressure in the 	<p>This model targets bubbly, droplet, and</p>

	interpenetrating between phases and it also allows phases to move at different speed.	<p>calculation domain by all phases</p> <ul style="list-style-type: none"> • Solving equations of momentum and continuity separately for each phase • Using appropriate expression for \vec{R}_{In} so that the conservation of momentum can be closed. 	particle-laden flows, slurry flows, hydro-transport, granular flow, etc. The model requires more computational effort compared to the Mixture model.
Discrete Phase Model (DPM)	Fluid phase in the calculation domain is treated as a continuum and dispersed phase are tracked as discrete particles.	<ul style="list-style-type: none"> • Solving Navier-Stokes equations for continuous phase • Modelling trajectory of a discrete phase particle (or droplet or bubble) by considering the force balance on that particle. 	This model is for flows with dispersed-phase volume fractions less than 10%. It is particularly useful for studying multiphase interaction in a spray regime. DPM model can be used to study droplet dynamics including breakup, collisions, and coalescence

Table 3-3 Models for Droplet Breakup, Collision, and Coalescence

Models for Droplet Breakup, Collision, and Coalescence			
Name	Description	Requirement	Remark
Models for Droplet Breakup			
Taylor Analogy Breakup (TAB) Model	Once the droplet oscillations reach a critical value, “parent” droplets will separate into a number of smaller	<ul style="list-style-type: none"> • Studying oscillations and distortions of droplet • Size of child droplets is calculated by equalling the combined energy of child droplets to the 	This is a classical model for droplet breakup in low-Weber-number sprays.

	“child” droplets.	<p>energy of the parent droplet</p> <ul style="list-style-type: none"> • Determining number of child droplet by Mass conservation when size of child droplets is obtained. 	
Wave Breakup Model	Droplet disintegrates as a result of relative velocity between gas and liquid phases.	<ul style="list-style-type: none"> • Deriving the jet stability analysis for the fastest-growing Kelvin-Helmholtz instability which determines time of breakup and the resulting droplet size • Predicting details of the newly-formed droplets by the wavelength and growth rate of the instability 	The model is suitable for atomization relating to high-Weber-number flow ($We > 100$) and high-speed injection.
KHRT Breakup Model	Improving the Wave Model by combining it with Rayleigh-Taylor instabilities.	<ul style="list-style-type: none"> • Modelling droplet breakup by tracking wave growth on the surface of the droplet • Breakup occurring due to the fastest growing instability based on local conditions 	The KHRT model was developed to simulate high Weber number sprays and should not be applied to low pressure sprays.
Stochastic Secondary Droplet (SSD) Model	Describing droplet breakup as a discrete random event which produces droplets with diameters over	<ul style="list-style-type: none"> • Calculating the critical radius and breakup time • Drops with a radius larger than the critical radius (derived from the critical Weber number) have their 	Probability of breakup is independent of the parent droplet size. The secondary

	a range.	breakup times incremented <ul style="list-style-type: none"> • When the breakup time on the parcel is larger than the critical breakup time (locally calculated from conditions in the cell and on the parcel), breakup occurs 	droplet size is sampled from an analytical solution of the Fokker-Planck equation for the probability distribution.
--	----------	---	---

Model for Collision and Droplet Coalescence

Model for Collision and Droplet Coalescence	Collision takes place when smaller droplet center passes within a flat circle centred around the collector of area $\pi(r_1 + r_2)^2$ perpendicular to the trajectory of the smaller droplet.	<ul style="list-style-type: none"> • Calculating the probability of the smaller droplet being within the collision volume for the probability of collision • Calculating the probability of coalescence by the offset of the collector droplet centre and the trajectory of the smaller droplet • Applying basic conservation laws for the properties of newly – formed coalesced droplets 	This model is most applicable for low-Weber-number collisions where collisions result in bouncing and coalescence.
---	---	---	--

Chapter 4

CFD-Aided Nozzle Development

Considering challenges for developing advanced nozzle design and establishing a CFD model for atomization, this chapter plans the workflow for overcoming the challenges depicted in previous chapters. Information presented in this chapter includes:

- **Workflow** for developing an advanced nozzle design with high performance and establishing a CFD calculation system for simulating the whole atomization process from internal nozzle flow to external droplet distribution;
- **Requirements for advanced nozzle design** which give specific aims for nozzle design and optimization;
- **Architecture of the CFD model** detailing a plan for setting up model interaction and data transfer by using User-Defined-Functions and subroutine.

4.1 Research Development Workflow

Figure 4.1 shows the workflow for this study. There is a close relationship between the development of the CFD model for the atomization process and the design of an advanced nozzle.

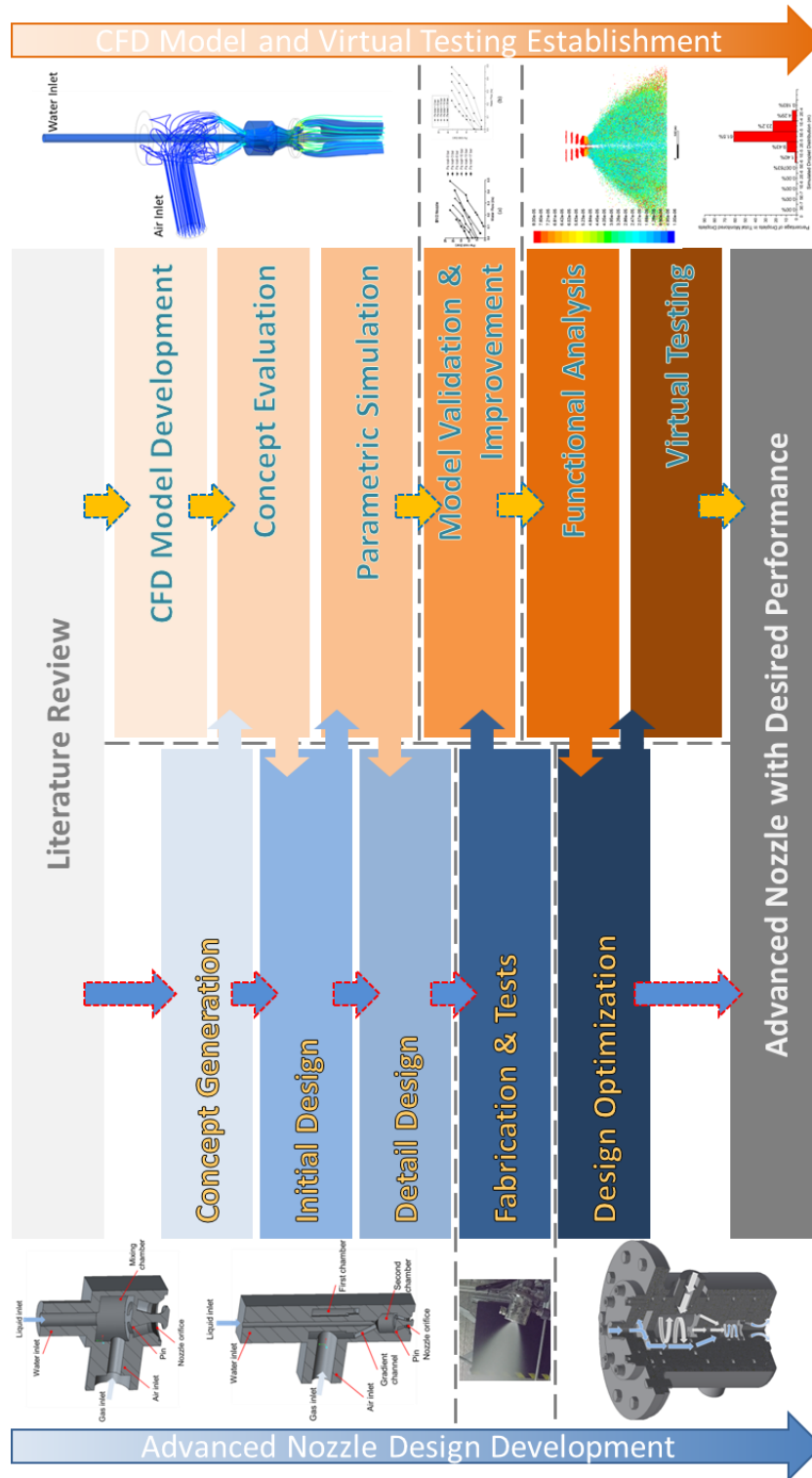


Figure 4.1 Workflow for developments of advance nozzle design and CFD model

After conducting the literature review, basic nozzle designs and their performances were studied (Chapter 2). Several concepts based on these nozzle designs are generated. At the same time, advantages and disadvantages of different CFD models for turbulent flows, multiphase flows, and droplet dynamics were investigated (Chapter 3). Potential models for simulating turbulent multiphase flows and for

tracking droplet interactions are selected. These models are connected in a logical way. User-defined functions and schemes are compiled to transfer results/variables between models. All the interconnected models together with user-defined functions and schemes form the CFD model for studying the spraying process. Generated nozzle designs are evaluated by this CFD model and the design having the best performance in generating small droplets and high flow rates will be set as the initial design. Parametric simulations based on the proposed CFD model will be used to study the performance of the nozzle when the dimensions of the nozzle features are changed. Details of nozzle design will be set according to the parametric study.

After the 1st detailed design is developed, parts of the nozzle will be fabricated and the nozzle will be tested in a fog dynamic lab. Spray characteristics of flow rates, spray angles, and droplet sizes will be recorded. These experimental data will be used to validate and improve the CFD model. If the performance of the 1st nozzle design is not satisfying the design requirements, the CFD model will be used to analyse the internal flow path of the nozzle (functional analysis) which cannot be achieved by experimental method. The design will then be optimized based on the result of the analysis. The optimized design can be tested by virtual testing using the validated CFD model and requirements of operating pressure will be provided for desired nozzle performances.

4.2 Requirements for the Nozzle Design

For the design and development of the advanced nozzle, the following set of key design requirements are defined (Figure 4.2) with the aim of improving the most commonly used nozzles:

- *The nozzle should be able to be used in indoor and outdoor conditions. At the outdoor conditions where the nozzle might experience strong cross wind, the droplet produced by the nozzle should have sufficient initial velocity at the orifice so that the generated droplet can still form a spray at the external area.*
- *Droplet size should be between 1-2000 μm . The droplets should be as small as possible to improve the efficacy of droplets.*
- *The nozzle should provide a flow rate close to 2.0 l/s of water solution.*
- *The nozzle should be adjustable for fogging and emulsifying based on the droplet size, fluid rates and fluid proportions.*

- *The nozzle must be able to mix or emulsify up to three fluids: water solution, air and different solutions.*
- *The nozzle should be able to mix solid particles as a third component.*
- *The nozzle should be able to provide a uniform solid cone spray pattern.*
- *The spray angle will be determined by the dispersal volume required and the estimated application distance and spray width.*
- *The spray for the application distance is to be between 2m and 8m.*

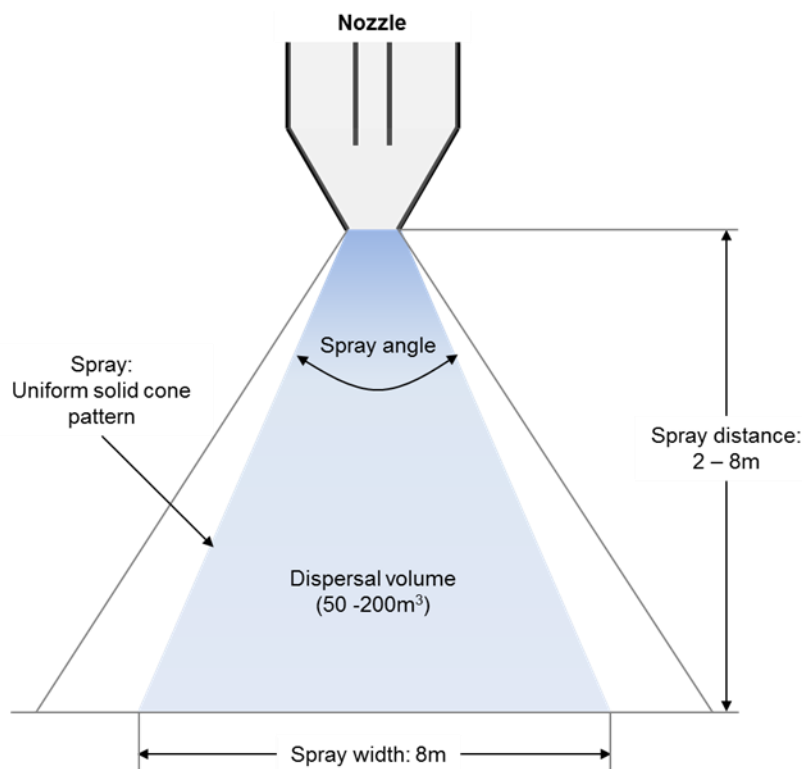


Figure 4.2 General requirements for the spray generated by the designed nozzle

4.3 Architecture of CFD Model

Figure 4.3 shows the calculation sequence and data flow path in the developed CFD model. The CFD model itself is mainly made up of three parts and is depicted at the middle-to-right side of the figure. There is a simulation for the whole flow field, a simulation for the spray region, and a self-developed model coupling module for collecting and transferring data between the two simulations. Transient simulations are used in both whole-flow-field and particle calculations. At the beginning of both calculations, initial conditions such as pressures, velocities, and dispersed-phase volume fractions are set. Conservation equations for mass and momentum are solved according to the initial conditions, followed by the solutions for other model scalars. Then a decision for calculation convergence is made. If the scaled residuals for

masses, momentums, or other model scalars are not meeting the predefined convergence criteria, a calculation loop will be activated to refine the result of masses, momentums, or other model scalars until the convergence criteria are reached. Once the calculations converge, for the whole simulation, a comparison will be made between the current calculation time and the pre-set calculation duration. The results will be used as final results if the pre-set calculation time is reached otherwise the time will be advanced for calculation of the next time step. For particle calculation, force-balance and trajectory calculations are conducted before the decision on the calculation time step is made.

The models of whole-field and spray region calculations are working well at their targeted regime of flows. However, neither of them, by its own, is capable of simulating the atomization process from the internal nozzle until the fine droplets are dispersed in the spray region. As presented in Chapter 3, whole-field simulation is valid only when the dispersed-phase volume fraction is more than 10%, while results of particle calculation are reliable when particle volume fraction is less than 10%. There is a gap between these two models and it remains an academic challenge to combine the advantages of both models. The self-developed module for automated data analysis and transfer intends to build communications between the two models and to bridge the knowledge gap between separated flow theories in order to establish practical systematic simulation for engineering calculations.

In this proposed model, general analysis is made after the field simulation is finished. Geometry of the nozzle internal volume is separated at a plane where dispersed-phase volume fraction is close to 10%. Flow properties on this plane are collected. Calculation domain for spray simulation starts from this plane onward until the edge of the external volume. Collected data from the whole simulation will be used as initial boundary conditions for the spray calculation. However, there is no existing method to automatically transfer information on the plane from one simulation to another. A coupling method has to be built in order to established communication between the two calculations.

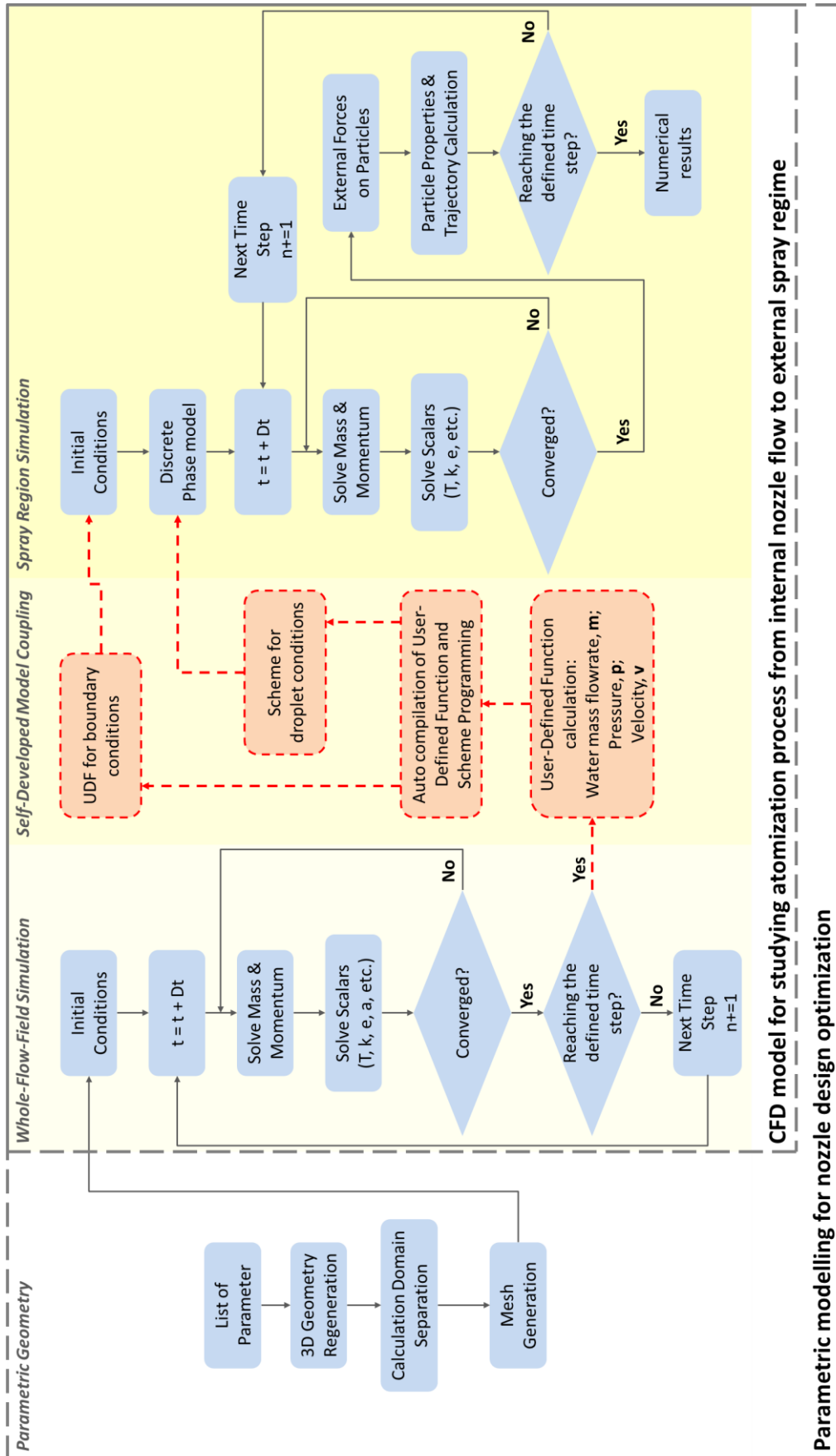


Figure 4.3 Numerical architecture of the proposed CFD model for studying the atomization process

This self-developed model coupling module is made of 4 steps, which are:

- *Data acquisition.*
- *Data analysis.*
- *Auto programming of user-defined functions and schemes.*
- *Inserting functions and schemes into algorithms.*

Data acquisition is a key step for calculation coupling since the calculation itself cannot automatically export information about water flow rates, water velocities, and total pressures on the plane in a form that is useful to the spray calculation. A user-defined scheme is activated at the end of the whole simulation to assess data on faces and cells adjacent to the plane.

Data analysis converts the raw data collected from previous step to information required by the spray calculation. In this study, values of total and gauge pressures, water mass flow rates, and water velocities are analysed. Water flow rates are calculated by summing up flows of water on faces composing the plane. In the mesh, if the plane is composed of n faces, the total water flow can be given as

$$M = \sum_{i=0}^n M_i \quad (99)$$

Here M is the total water mass flow rate and M_i represents the mass flow on the i th face composing the coupling plane. Averaged value of water velocity over the surface is calculated for the initial velocity of water droplets. The values are calculated by

$$\vec{u} = \frac{1}{\sum_{i=0}^n A_i} \sum_{i=0}^n (\vec{u}_i \cdot A_i) \quad (100)$$

\vec{u}_i and \vec{u} are facial and facet-averaged velocities for water. A_i is the area for each individual face. The values of gauge pressures are calculated in a similar way as velocity. However, gauge pressure is based on values on each cell centre. Facet value for gauge pressure has to be calculated by averaging the values of the two cells adjacent to the same face. Averaged gauge pressures are calculated as

$$p_{gauge} = \frac{1}{2 \sum_{i=0}^n A_i} \sum_{i=0}^n [(p_{i1} + p_{i2}) \cdot A_i] \quad (101)$$

p_{gauge} is the facet-averaged value of gauge pressure. p_{i1} , p_{i2} denotes gauge pressures in two cells adjacent to the same face composing the coupling plane. Facet average value for total pressures are derived from cell variables which are

$$p_{total} = \frac{1}{2 \sum_{i=0}^n A_i} \sum_{i=0}^n A_i \cdot \left[\left(p_{i1} + \frac{1}{2} \rho v_{i1}^2 \right) \cdot f_{wi1} + p_{i1} \cdot \left(1 + \frac{\gamma-1}{2} M^2 \right)^{\frac{\gamma}{\gamma-1}} \cdot (1 - f_{wi1}) + \left(p_{i2} + \frac{1}{2} \rho v_{i2}^2 \right) \cdot f_{wi2} + p_{i2} \cdot \left(1 + \frac{\gamma-1}{2} M^2 \right)^{\frac{\gamma}{\gamma-1}} \cdot (1 - f_{wi2}) \right] \quad (102)$$

here, $\left(p_{i1} + \frac{1}{2} \rho v_{i1}^2 \right) \cdot f_{wi1}$ and $\left(p_{i2} + \frac{1}{2} \rho v_{i2}^2 \right) \cdot f_{wi2}$ represent total pressures of water in adjacent cells. They are calculated as the sum of gauge pressure and dynamic pressure [4]. $p_{i1} \cdot \left(1 + \frac{\gamma-1}{2} M^2 \right)^{\frac{\gamma}{\gamma-1}}$ and $p_{i2} \cdot \left(1 + \frac{\gamma-1}{2} M^2 \right)^{\frac{\gamma}{\gamma-1}} \cdot (1 - f_{wi2})$ calculate the total pressures of air based on gauge pressure and Mach number [4]. M is Mach number which is the ratio between flow velocity and local speed of sound. γ is the ratio of specific heats and is set as 1.4 for air.

Auto programming starts after values for water mass flows, water velocities, and pressures are obtained. Because the computation considers the effect of compressible air, pressures have to be increased gradually from normal pressure (101325 Pa) so that the model will be stable and reliable. User-Defined-Functions (UDFs) are used to apply calculated values of pressures on geometry boundaries. Modelling values for DPM calculation cannot be parameterised in Fluent, so User-Defined-Schemes (UDSs) have to be written for inputting values of water mass flow rates and velocities. Both the UDFs and UDSs are automatically programmed by the coupling model with parameters calculated from the previous step.

Inserting functions and schemes into algorithms is the final step of the coupling module. Spray calculation is read in UDFs and UDSs from working folders together with other predefined model parameters and geometry. Boundary conditions and droplet properties are set correct based on the results from whole simulations. Then the calculation starts automatically.

By connecting the whole-flow-field simulation and spray region simulation with the developed model coupling method, full simulation is achieved without the need for manual data transfer. This bundle of CFD models is able to simulate the whole atomization process from internal flow to external atomization. As shown in Figure 4.3, it is possible for this model to work with parametric geometry. After defining the list of calculation tasks, the model can finish hundreds or thousands of calculations with different geometrical dimensions, operating conditions, or fluid properties without manual intervention, which is efficient and reliable for engineering calculation.

4.4 Summary

This chapter presents some detail planning and targets for the whole study. In this chapter:

- A workflow for a CFD-aided nozzle development process has been developed and presented. The workflow has been shown in Figure 4.1. Geometries generated at different periods of the nozzle development process are used as inputs for CFD simulations and data obtained from physical experiments will help to validate the CFD model. While results from concept evaluation, parametric simulation, and functional analysis achieved in CFD software support concept justification, dimension selection, and design optimization in the nozzle development process. The purpose of the workflow is to overcome challenges in advanced nozzle design and simulation for the atomization process;
- Requirements for advanced nozzle design have been defined. The requirements include specific ranges for flow rate, droplet size and other functional properties for the final optimized nozzle;
- Architecture of the CFD model has been designed in detail. The main body of the CFD calculation system for the atomization process from internal nozzle flow to external droplet distribution consists of three parts. 1st is the whole flow field simulation which calculates fields of variables and properties in the whole calculation domain. The 2nd is the discrete phase calculation focusing on modelling droplet dynamics. The 3rd is the most important part where the 1st 2 parts of calculations are connected and data are transferred from the 1st

simulation to the 2nd. All these steps are finished automatically. Together with parametric model design, the developed CFD system can handle a large amount of calculation for design optimization.

Chapter 5

Design of Multi-Fluids Atomizer

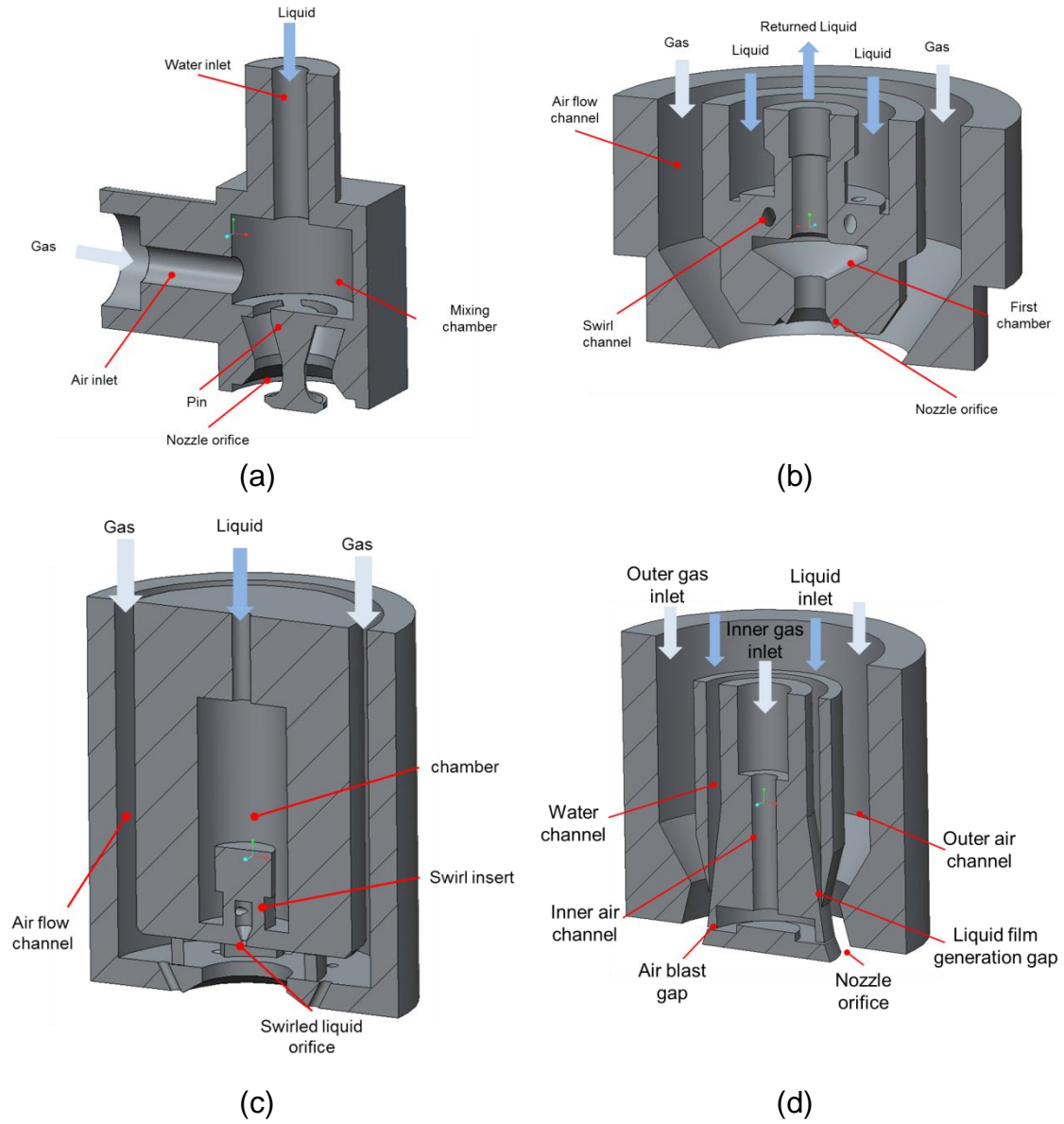
This section presents results of the work from the concept generation and optimization phase of the nozzle development. This development includes:

- **Concept generation** which is based on knowledge gained from the literature review of different nozzle designs;
- **Concept evaluation** using the developed CFD calculating system to estimate performances of flow rates, drop sizes, and droplet distributions from generated concepts;
- **Nozzle dimensions optimization** which conducts parametric simulations for investigating effects of different nozzle dimensions on spraying performances.
- **Investigation on nozzle size effect** studying the flow rates and droplet size affected by the scale of the nozzle.

5.1 Nozzle Design Concepts

In this study, 6 nozzle designs featuring different configurations were initially selected as the potential design basis for a multi-phase atomizer targeting high liquid flow rate and small droplet size. Figure 5.1 (a) – (f) present the 6 potential nozzle designs.

Figure 5.1 (a) is a typical right-angle twin-fluid design based on a commercial nozzle from Delavan Ltd. To perform atomization, Water is fed into the nozzle axially and interacts with air entering through the tangential inlet. The mixed fluid flow will then impact against the pin, stream through the slots and flow out from the orifice.



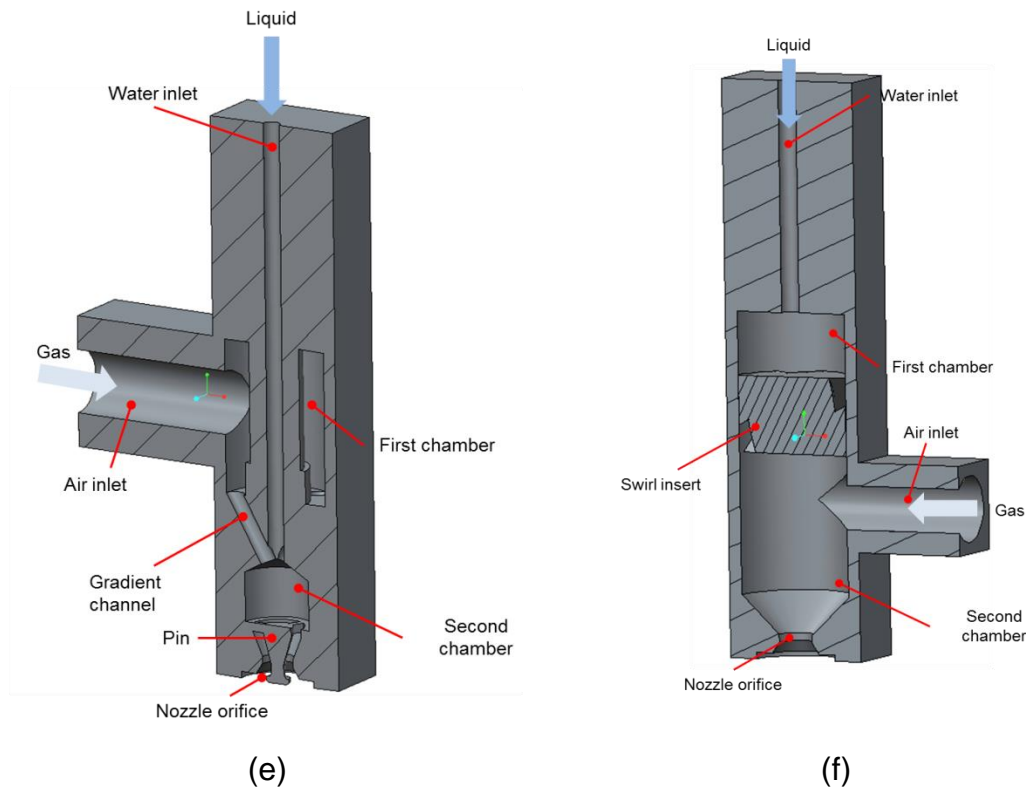


Figure 5.1 Selected nozzle configurations

Figure 5.1 (b) is based on a patented spill-return nozzle design [81]. This type of nozzle can produce well-atomized spray with a wide range of flow rate [15]. Water is fed from the water inlet and enters the first chamber through three swirl channels. Water in the first chamber can leave the nozzle either from the spill return orifice or from the nozzle orifice. When the full capacity of nozzle is required, a valve mounted at the spill line will be totally shut so that there will be no liquid being spilled from the nozzle. Once the valve is open, part of the liquid will flow away from the nozzle chamber, resulting in the reduction of flow rate from the orifice. Swirled water flowing out from nozzle orifice will mix with strong air flow in the outer air channel.

Figure 5.1 (c) is based on an air-assist pressure-swirl atomizer for *Jatropha* oils [82]. Water is supplied from the central inlet and flows through the swirl insert to introduce centrifugal force on water. After spinning in the swirl chamber, water flows out from the small orifice and interacts with the strong air flow.

Figure 5.1 (d) is based on a patented pre-filming nozzle [83]. This configuration has two air inlets. Water is supplied through the third inlet which sits between the inner and outer air inlets. Water fed through the inlet firstly flows through a small gap and forms a thin water sheet. Then the water sheet is broken into filaments and is

accelerated by air stream from outer air inlet. The water-air mixture continues to flow downstream and interact with air from the inner inlet, which further breaks the water filaments into small droplets.

Figure 5.1 (e) is another design based on a commercial air-swirl nozzle from Delavan. This design is a variant of the right-angle twin-fluid nozzle (Figure 5.1 (a)). Rather than feeding the air directly into the mixing chamber, air is firstly fed into a distributing chamber which separates the air into three streams and pushes them into the mixing chamber through 3 gradient channels. The water stream interacts and mixes with air streams in the mixing chamber. The air-water mixture hits the pin before flowing out of the nozzle from the orifice.

Figure 5.1 (f) features a twin swirl design which is an originated nozzle concept developed based on the literature review of atomization mechanism. The swirl effect of water or air helps with the disintegration of the liquid jet and the formation of small drops. However, there is little research or commercial nozzles available for the twin swirl design (both water and air are swirled before they were mixed with each other). This design is intended to highlight the configuration of the twin swirl nozzle. Water is supplied from the water inlet and separated into three streams in the first chamber. Before being fed into the mixing chamber, water streams flow through a swirl insert at which water is swirled. The swirl water is then mixed with the air stream fed from a tangential air inlet. Swirl effect is intensified in the water and finally the mixed fluid flow exits the nozzle and generates spray.

5.2 Numerical Evaluation of Nozzle Concepts

Performances of 6 nozzle designs for multi-fluid atomization were evaluated by using the proposed CFD simulation procedure. The main characteristics of concern were water and air flow rates, cone patterns, spray angles, ranges and mean values of droplets of the produced sprays. Numerical studies for each nozzle concept were accomplished in two steps. First was the calculation of fields of interest in the whole calculation domain. The Eulerian-Eulerian multiphase model was adopted to model water volume fraction, fields of pressure and velocity, spray angle, and water flow rate in both internal channel flow and external spray region. Then, in the second computational step, the atomization process was captured in more detail by using the Lagrangian Discrete Phase Method (DPM). Results obtained from the first numerical

step were transferred into the DPM model as initial boundary conditions by User-Defined Functions and schemes. Figure 5.2 (a) shows the 3D geometry of the calculation domain for concept A. Pressure inlets were assigned to water and air inlets with specified inlet pressures. The volume fraction of input water was set as 1 at the water inlet and set as 0 at the air inlet. The nozzle internal surface was designated as a no-slip wall. Fluid attaching to the wall of nozzle had a velocity of zero. At the external spray region, pressure outlets were assigned at the border where fluid can flow away from the calculation domain. Similar boundary conditions were applied in simulations for different design concepts. Figure 5.2 (b) presents the mesh for numerical evaluation of concept A. The calculation domain was comprised of 802,588 elements. The total number of elements for each design concept might vary depending on the size of each nozzle, complexity of design feature, and type of element that was applicable for the specific geometry. However, best efforts have been made to create the external spray region, partition the geometry, and generate the mesh so that all numerical evaluations were conducted with the same sizes of external spray region and similar mesh quality. In this case, the results were more comparable.

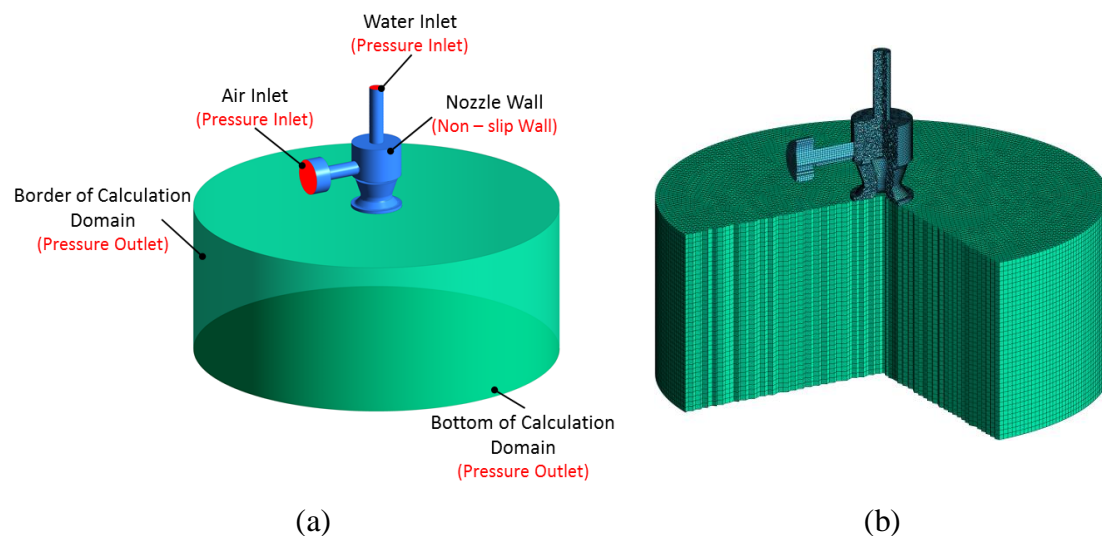


Figure 5.2 (a) 3D geometry and boundary conditions for Concept A. (b) Mesh for simulation of concept A

An unsteady flow calculation was used for all simulations for concept evaluation. Considering the computational effort and flow regime where a wide distribution of the dispersed liquid was mixing with air, the mixture model was used to study multiphase interaction in whole flow-field simulations for all nozzle concepts. A realizable k-epsilon model with scalable wall functions was adopted to describe turbulent flow. Pressures at air and water inlets were kept the same for all simulations so that a direct

comparison could be made based on results of water flow rates, spray angles, droplet distribution, and drop size ranges.

In the second step of evaluation for the spray region, numerical results including gauge pressures, velocities, and water flow rates from the first numerical step were used as boundary conditions. A Discrete Phase Model (DPM) was applied to capture the interaction between air flow and dispersed droplets. Spray models of Breakup, Collision, and Coalescence were enabled so that size changes in droplets during the atomization process were considered. It is impossible to measure droplet sizes after initial breakup which starts inside the nozzle body. The initial breakup can be seen as droplets produced by single fluid nozzle and released into the high-speed air stream. Droplets smaller than $300\ \mu\text{m}$ can be produced by single-fluid nozzle at a water pressure of $10\ \text{bar}$. Based on the droplet break theory reviewed in chapter 3.4.1, final size of droplet depends on the aerodynamic force and surface tension. So, initial sizes of droplets were set between $100\ \mu\text{m}$ and $200\ \mu\text{m}$ with an average size of $150\ \mu\text{m}$ for all concepts. In this case, mean droplet sizes generated by nozzles were mainly dependant on the generated flow condition. Table 5-1 lists CFD models and boundary conditions used in the two-step evaluation procedure for all design concepts.

Table 5-1 CFD models and boundary conditions for numerical evaluation of nozzle concepts

Simulation	Model / Boundary	Setting
1st Step Simulation of whole flow field	Multiphase Model	Mixture
	Viscous Model	Realizable k – epsilon model with Scalable Wall Functions
	Air Inlet	Pressure Inlet with 728, 080 Pa total pressure and 700, 000 Pa gauge pressure
	Water Inlet	Pressure Inlet with 1, 044, 084 Pa total pressure and 750, 000 Pa gauge pressure
	Internal Wall	No – Slip Wall
	Borders of External Spray Region	Pressure Outlet with 0 Pa gauge pressure

	Outlet	Pressure Outlet with 0 Pa gauge pressure
2nd Step Simulation of spray region	Multiphase Model	Discrete Phase Model (DPM) with spray model of Breakup, Collision, and Coalescence
	Viscous Model	Realizable k – epsilon model with Scalable Wall Functions
	Air Inlet	Pressure Inlet, total and gauge pressures are based on the results from 1 st step
	Water Inlet	Pressure Inlet, total and gauge pressures are based on the results from 1st step
	Internal Wall	No – Slip Wall, reflect boundary condition for particles
	Borders of External Spray Region	Pressure Outlet with 0 Pa gauge pressure, reflect boundary condition for particles
	Outlet	Pressure Outlet with 0 Pa gauge pressure, reflect boundary condition for particles
	Drop Size Range	100 – 200 μm
	Mean Drop Diameter	150 μm

In the simulations, air was treated as a compressible fluid. The ideal gas law was introduced to model the behaviour of air. Equation (103) presents the ideal gas law which describes the relationship between state of a specific amount of gas, its pressure, volume, and temperature.

$$PV = nRT \quad (103)$$

In this equation, P is the pressure of gas, V is the volume, n is the amount of substance (in moles), R is the universal gas constant, and T is the absolute temperature. Other material properties of air and water are list in Table 5-2

Table 5-2 Material properties of air and water

Material	Density	Specific Heat	Thermal Conductivity	Viscosity	Molecular Weight
Air	Ideal Gas	1006.43 J/kg·K	0.0242 W/m·K	1.7894e-5 kg/m·s	28.966 kg/kgmol
Water	998.2 kg/m ³	N/A	N/A	0.001003 kg/m·s	N/A

5.3 Results of Concept Evaluation

Numerical results of air and water flow, cone pattern, droplet distribution and concentration, water flow rate, and mean droplet size for each of the design concepts are calculated and presented in this section.

5.3.1 Concept A

Figure 5.3 presents the simulation results of Concept A. Figure 5.3 (a) illustrates the volumetric distribution of water in the whole calculation domain. Only water is fed into the nozzle from the water inlet. Water is then blasted at the mixing chamber by an air stream entering the nozzle from the air inlet. Air-water mixture flows out from the nozzle orifice and forms a wide-angle full-cone spray at the external area. Figure 5.3 (b) shows the distribution of droplets in the spray region and their mean droplet sizes. It can be seen that nearly all the droplets in space are smaller than 60 μm . Initial breakups of droplets happens inside the nozzle channel. The smallest droplets are observed at the centre of the spray volume and the size of droplets get bigger when they are closer to the edge of the spray. Figure 5.3 (c) displays the spatial distribution of water droplets and droplet mean diameter. The number of particles in a cell represents the amount of droplets locate in a control volume. A denser distribution of droplets can be found if the value is higher. From the figure, it can be observed that water initially concentrates at the nozzle orifice. Then it gets diluted when it flows further downstream and spreads radially away from the central line of spray. Distribution of water is initially not even across the cross-section of the spray region perpendicular to the flow direction. The number of droplets becomes more uniform downstream of the spray. For the mean droplet diameter, small droplets are observed close to the nozzle orifice. At regions away from the orifice, smaller droplets are observed near the centre of spray. While at the edge of the spray region, movements of droplets are affected by stagnating air and the travelling speeds are slower. As a result droplets bump into each other which causes larger droplet sizes at this area. Figure 5.3 (d) provides statistical information on the diameter of droplets exiting the calculation domain from the bottom edge. Most of the droplets reaching the bottom edge have diameters less than 10 μm .

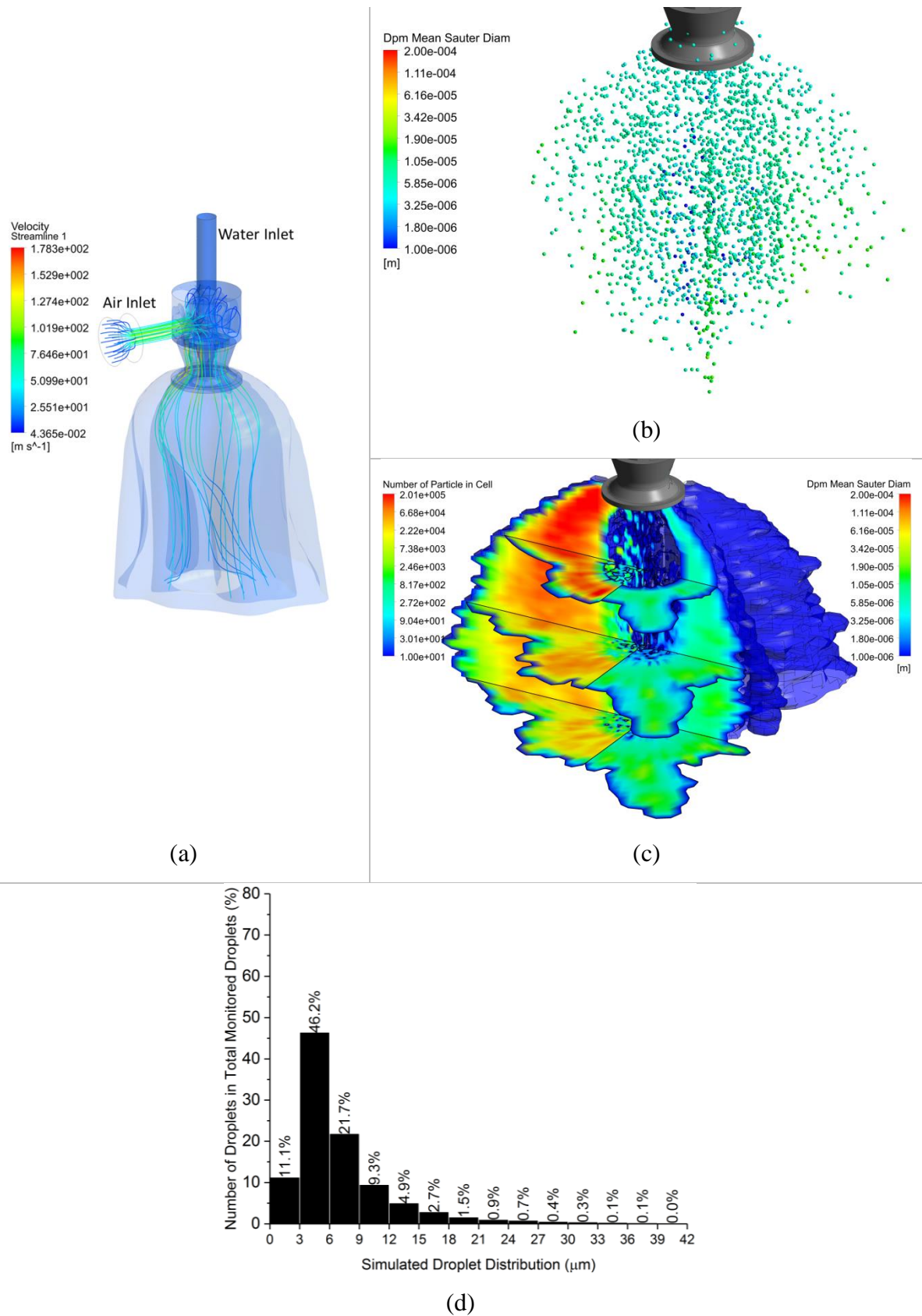


Figure 5.3 Numerical results of concept A: (a) volumetric distribution of water and streamlines of air velocity; (b) tracking of water droplets and their SMD values; (c) spatial distribution of droplet number and mean droplet size; (d) histogram presenting diameter of droplets exiting the outlet of calculation domains.

Table 5-3 concludes the information of spray produced by nozzle concept A. The nozzle is able to mix 0.027 kg of air with 0.98 kg of water in one second. Generated spray is characterized by a full cone pattern with a wide spray angle. Sizes of droplets reaching 0.075 mm downstream from the nozzle orifice have an SMD value of 16.8 μm . Droplet sizes range from 0.9 μm to 65 μm .

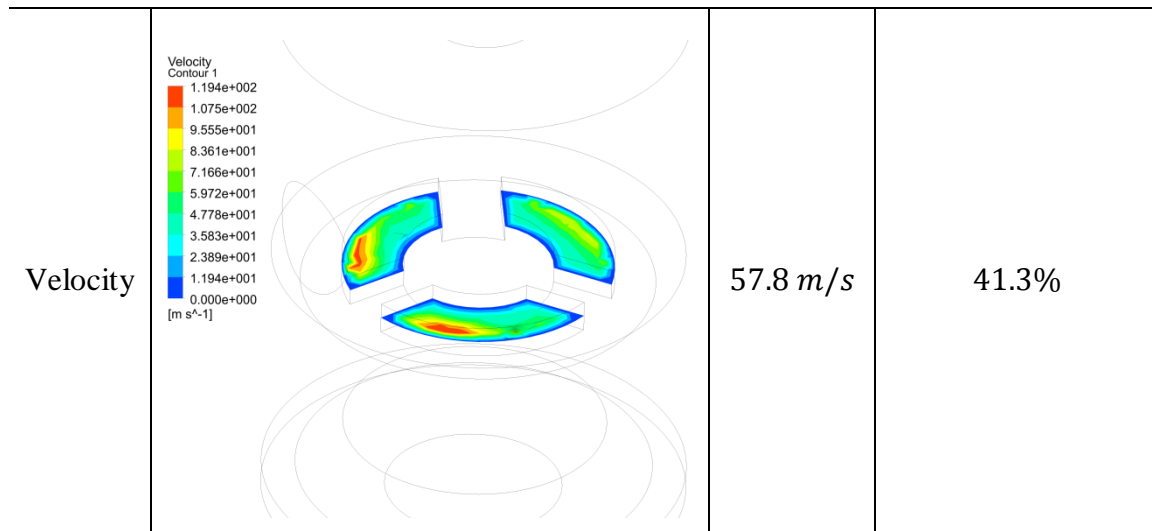
Table 5-3 Statistics information of spray generated by Concept A

Air Flow Rate (kg/s)	Water Flow Rate (kg/s)	Cone Pattern	Drop Size Range (μm)	Sauter Mean Diameter (μm)
0.027	0.980	Full cone, wide angle	0.9 – 65.0	16.8

Table 5-4 shows the distribution of pressure and velocity at the interface for the two steps of the CFD model. The interface has an area of $1.02774e - 4 \text{ m}^2$. The pressure at the interface ranges from $3.774e4 \text{ Pa}$ to $5.556e5 \text{ Pa}$ with an area-averaged value of $4.051e5 \text{ Pa}$. 69.8% of the area at the interface has the pressure value within $\pm 30\%$ of the averaged value of pressure. The velocity distribution at the interface has a range from 0 m/s to 119.4 m/s. The area-averaged velocity is 57.8 m/s with 41.3% of the area has velocity within $\pm 30\%$ of the averaged velocity. Considering the calculation stability and accuracy, it is reasonable to use the averaged value at the interface from the whole-flow-field simulation as the boundary conditions for the droplet calculation.

Table 5-4 The distribution of pressure and velocity at the interface for the two models

	Distribution	Averaged Value	Percentage of area within $\pm 30\%$ of the averaged value
Pressure		405071 Pa	69.8%



5.3.2 Concept B

Figure 5.4 shows the simulation results of Concept B. The volumetric distribution of water is shown in Figure 5.4(a). It can be seen from the result that water fed into the nozzle via the water inlet firstly runs through the swirl channel. Then water reaches a chamber which is connected with two orifices. They are the nozzle orifice and the liquid-return orifice. The liquid-return orifice is joined with a valve whose cross-section area is adjustable. In this case, the flow rate of water can be controlled. In the simulation the liquid-return orifice was kept closed so that all water fed into the nozzle flowed out from the nozzle orifice. Water flows towards the nozzle orifice then meets and interacts with a high-speed air stream, which causes the spreading and breakup of droplets. Spray produced by this nozzle design has a small spray angle. Figure 5.4 (b) shows the distribution of droplets in the spray region and their mean droplet sizes. A spray pattern similar to the one obtained from whole-flow field simulation is observed. Droplets distribute within a narrow spray region and droplet sizes fall within a relatively small range. Most of the droplets are smaller than $32\ \mu\text{m}$. Figure 5.4 (c) is the spatial distribution of droplet number in a cell and droplet mean diameter. Spray produced by this nozzle has even droplet distribution and droplet diameter along the flow path. No big variations of droplet number and size are observed streamwise. The number of droplets in a cell is slightly decreased as water flows away from the orifice and the covering area perpendicular to main flow direction increases. Figure 5.4 (d) describes statistical information of droplet sizes exiting from the bottom edge. Most of the droplets reaching the bottom edge have diameters less than $24\ \mu\text{m}$.

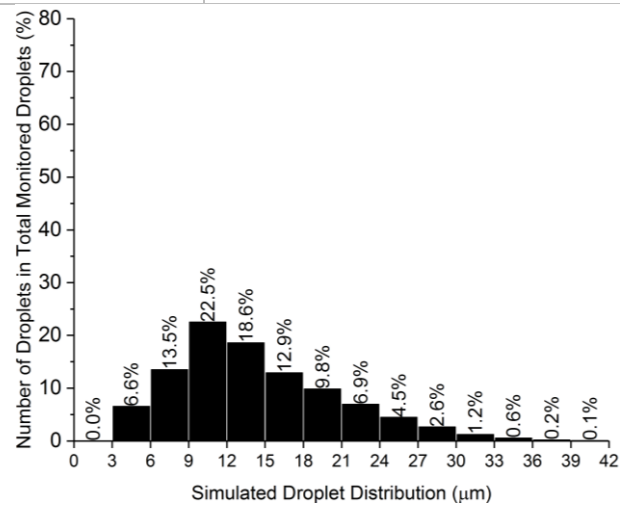
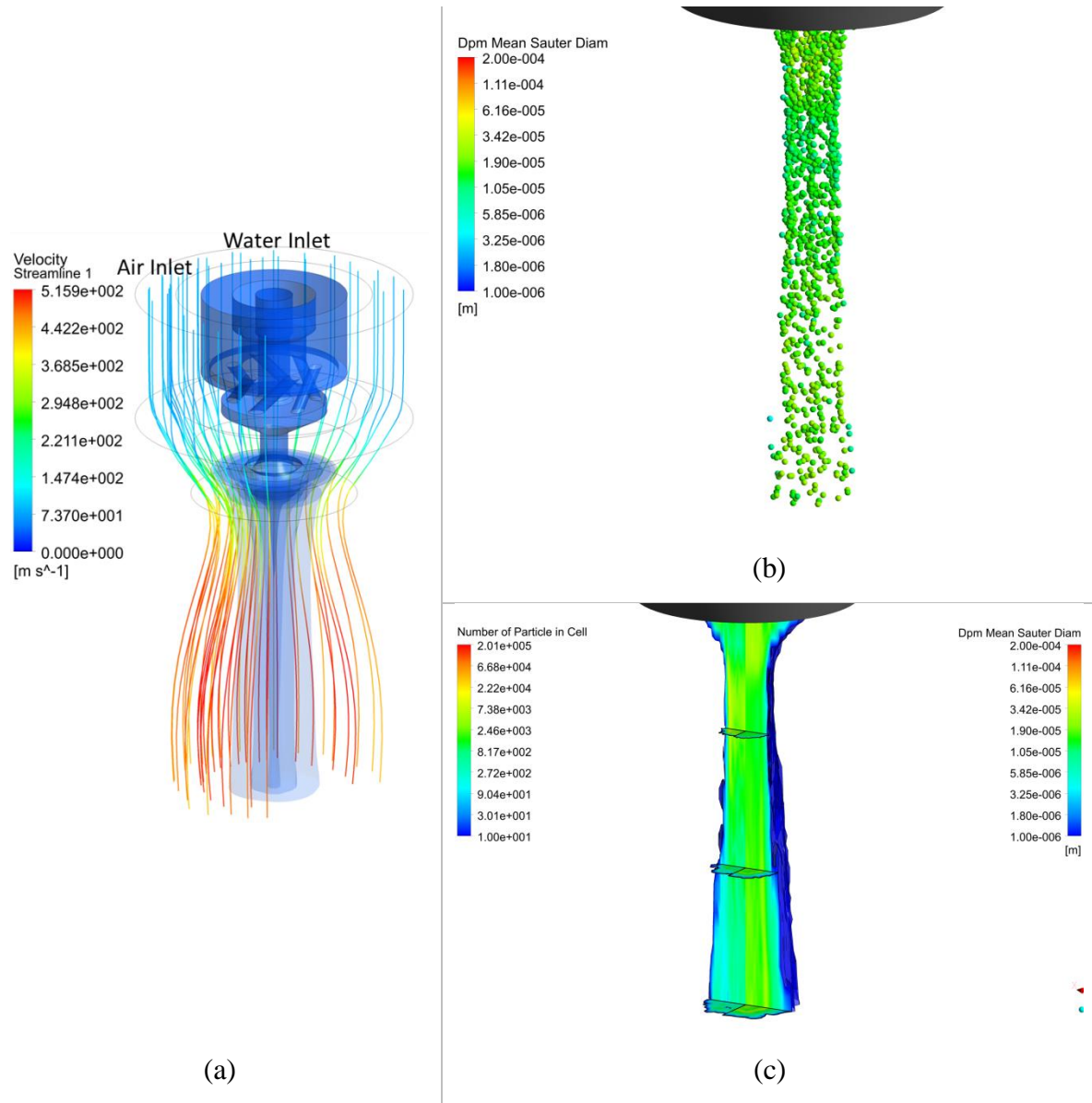


Figure 5.4 Numerical results of concept B: (a) volumetric distribution of water and streamlines of air velocity; (b) tracking of water droplets and their SMD values; (c) spatial distribution of water droplet

number and mean droplet size; (d) histogram presenting diameter of droplets exiting the outlet of calculation domains.

Table 5-5 summaries the information of spray produced by nozzle concept B. Compared to the results from concept A, this nozzle mixes a larger amount of air (1.501 kg) with less amount of water (0.488 kg) per second. This nozzle design also produces a full-cone spray but the spray angle is much smaller. The diameter of Droplets in the spray ranges from 2.9 μm to 50.7 μm . Mean droplet size of the produced spray is 20.1 μm .

Table 5-5 Statistics information of spray generated by Concept B

Air Flow Rate (kg/s)	Water Flow Rate (kg/s)	Cone Pattern	Drop Size Range (μm)	Sauter Mean Diameter (μm)
1.501	0.488	Full cone, narrow angle	2.9 – 50.7	20.1

5.3.3 Concept C

Figure 5.5 presents the simulation results of Concept C. In Figure 5.5, water is fed from the water inlet. After filling the nozzle chamber, pressurized water flows into the swirl insert through two horizontal off-centre channels. Water forced to flow forward in a spiral along the centre line of nozzle escapes from the nozzle orifice and is mixed with the high-speed air stream externally. Interaction between air and water causes the breakup and spreading of droplets, which forms a full-cone spray. Droplet distribution shown in Figure 5.5 (b) indicates that spray generated by concept C has a small spray angle. Most droplets have diameters less than 20 μm . Figure 5.5 (c) displays spatial distribution of droplet number and mean diameter. Distributions of the number of droplets and mean droplet diameter are similar across the spray area. Figure 5.5 (d) reveals the percentages occupied by different diameters of droplets exiting from the outlet of the calculation domain. Most of the droplets fall into the range from 3 μm to 12 μm .

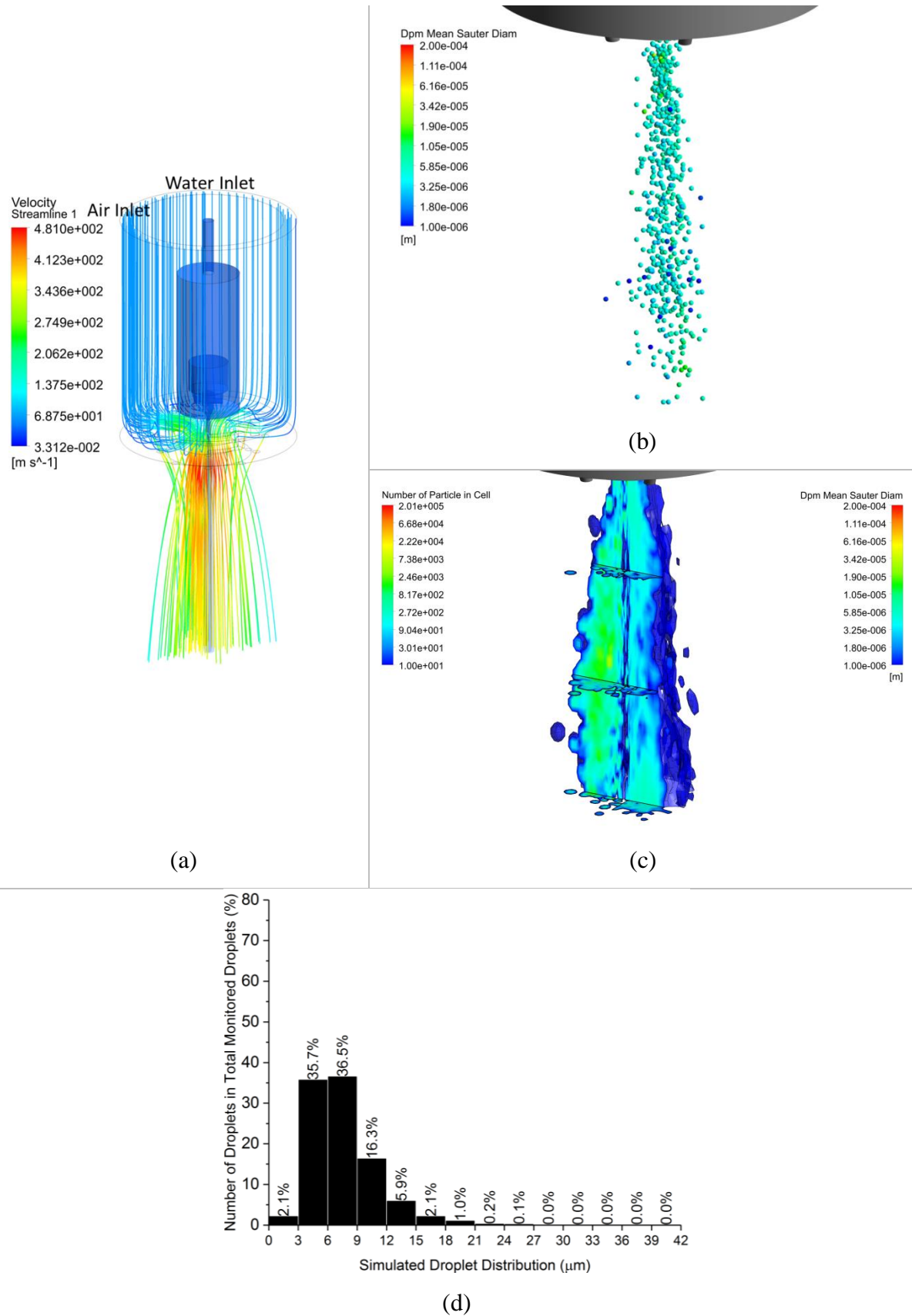


Figure 5.5 Numerical results of concept C: (a) volumetric distribution of water and streamlines of air velocity; (b) tracking of water droplets and their SMD values; (c) spatial distribution of water droplet number and mean droplet size; (d) histogram presenting diameter of droplets exiting the outlet of calculation domains.

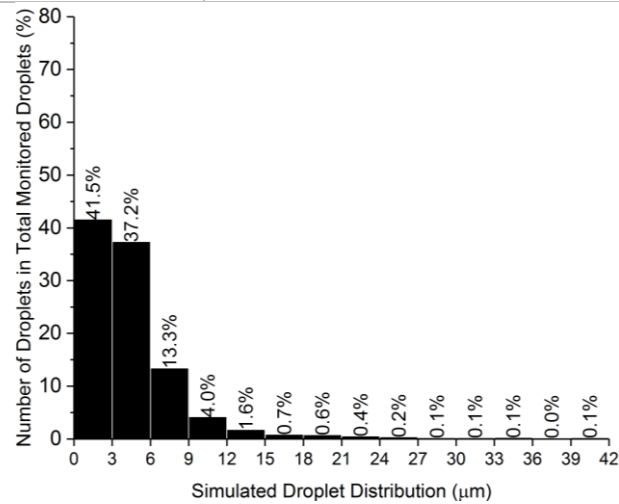
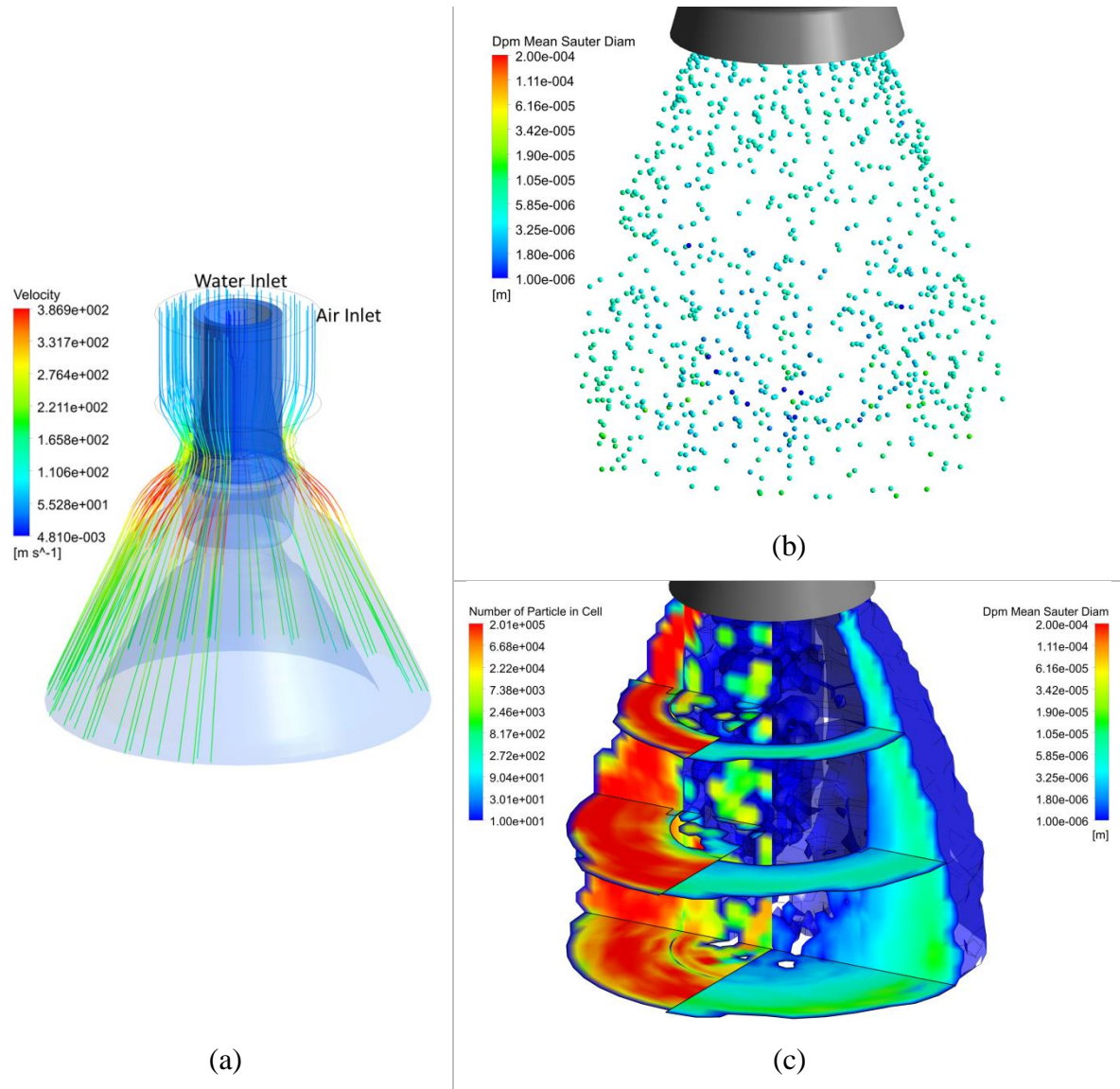
Data listed in Table 5-6 specifies the characteristics of spray produced by concept C. A small amount of water is mixed with the bulk air stream to produce a full-cone narrow-angle spray. Fine droplets are produced during the atomization process. The smallest droplet has a diameter of $1.7\ \mu\text{m}$ while the largest droplet leaving the calculation domain is $39\ \mu\text{m}$. Mean size of the droplets is $11\ \mu\text{m}$.

Table 5-6 Statistics information of spray generated by Concept C

Air Flow Rate (kg/s)	Water Flow Rate (kg/s)	Cone Pattern	Drop Size Range (μm)	Sauter Mean Diameter (μm)
0.539	0.028	Full cone, narrow angle	1.7 – 39.0	11.0

5.3.4 Concept D

Figure 5.6 presents the simulation results of Concept D. Volumetric distribution of water and streamline of air shown in Figure 5.6 (a) illustrates the flow path for water and air. In concept D, compressed air is supplied through inner and outer air inlets while water enters the nozzle via the annular water inlet in between the two air inlets. Water then flows through a small gap where thin film of water is formed. The flattened water film meets with air supplied from the external inlet, which separates the water stream into droplets. After the first encounter of air and water, air fed from the inner inlet interacts again with the mixture stream which breaks the droplets into smaller sizes before they flow out from the nozzle orifice and generate a full-cone spray. Figure 5.6 (b) reveals that spray generated by concept D has much larger spray angles than the ones produced by concept B and C. Smaller droplets exist close to the centre of the spray region while droplets near the edge of spray have a relatively larger diameter. Most of the droplets are less than $20\ \mu\text{m}$. Results of droplet number and droplet mean diameter displayed in Figure 5.6 (c) show the changes of distributions in space. High mass-density concentration is observed around the nozzle orifice. As the droplets flow downstream and are mixed with ambient air, the droplet number is decreased. Mean droplet diameter is similar across the spray region. The histogram of droplet distribution displayed in Figure 5.6 (d) emphasizes that fine droplets are produced by this nozzle concept. Most of the droplets have diameters less than $9\ \mu\text{m}$.



(d)

Figure 5.6 Numerical results of concept D: (a) volumetric distribution of water and streamlines of air velocity; (b) tracking of water droplets and their SMD values; (c) spatial distribution of water droplet number and mean droplet size; (d) histogram presenting diameter of droplets exiting the outlet of calculation domains.

Characteristics of spray produced by concept D are shown in Table 5-7. Water used by this nozzle for atomization has a flow rate of 1.351 *kg/s* and 0.72 *kg/s* of air is required to achieve the atomization process. Generated spray has a full-cone spray pattern with wide spray angle. Sizes of droplets in the spray range from 0.8 μm to 51 μm with an averaged value of 15.1 μm .

Table 5-7 Statistics information of spray generated by Concept D

Air Flow Rate (kg/s)	Water Flow Rate (kg/s)	Cone Pattern	Drop Size Range (μm)	Sauter Mean Diameter (μm)
0.720	1.351	Full cone, wide angle	0.8 – 51.0	15.1

5.3.5 Concept E

Figure 5.7 is the simulation results of Concept D. The streamline of air displayed in Figure 5.7 (a) reveals the flow path for air in the atomization process. Compressed air is fed to the first chamber from air inlet. Then the air is separated into three streams and pushed toward the mixing chamber to interact with water which is directly supplied from the water inlet to the mixing chamber. The mixture of air and water finally flows out of the nozzle from nozzle orifice and produces a full-cone spray. Figure 5.7 (b) shows the droplet distribution of spray generated by concept D. Spray constituted by a cloud of droplets in different sizes has a large spray angle. Most of the droplets are smaller than 35 μm . Smaller droplets locate near the centre of the droplet cloud. Variations of number of droplets and mean droplet size distributions are observed in different regions of the spray in Figure 5.7 (c). High droplet concentrations can be found close to the nozzle orifice. As the spray continues to flow downstream and mix with ambient air, concentrated droplet distribution is diluted and distribution is more even. For mean droplet size, initial breakup of the droplet happens inside the nozzle during the air-water mixing process. Droplets exiting from the nozzle orifice have small sizes. As the spray develops a difference of droplet size in space starts to emerge due to uneven velocity. Droplets moving at the edge of the spray are slowed down by the stagnating ambient air, which results in droplet collisions and coalescence. Droplets at the centre of the spray are less affected by the surrounding environment and maintain their fine sizes. Figure 5.7 (d) clarifies the information of droplet sizes at the exit of the calculation domain. Most of the droplets leaving from the domain outlet have diameters less than 9 μm .

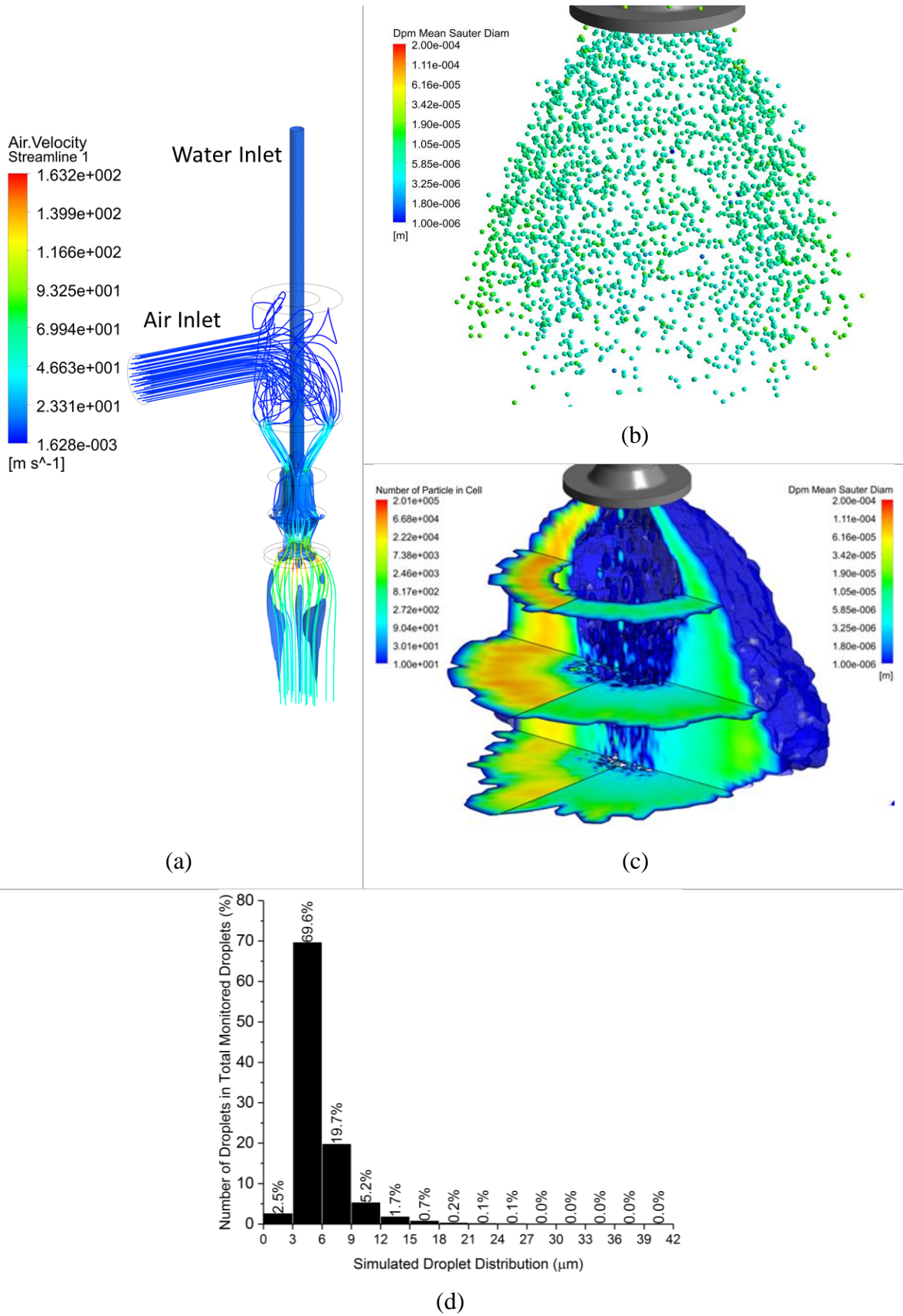


Figure 5.7 Numerical results of concept E: (a) volumetric distribution of water and streamlines of air velocity; (b) tracking of water droplets and their SMD values; (c) spatial distribution of water droplet number and mean droplet size; (d) histogram presenting diameter of droplets exiting the outlet of calculation domains.

Table 5-8 lists the information of spray produced by nozzle concept E. In every second, nozzle E mixes 0.035 kg of air with 0.881 kg of water. Although not a large amount of air is consumed for atomization, this nozzle is able to produce spray with fine droplets. Droplets leaving the calculation domain have sizes range from 1.1 μm to 62.9 μm with an average value of 9.2 μm . The produced spray has full-cone spray pattern and the spray angle is wide.

Table 5-8 Statistics information of spray generated by Concept E

Air Flow Rate (kg/s)	Water Flow Rate (kg/s)	Cone Pattern	Drop Size Range (μm)	Sauter Mean Diameter (μm)
0.035	0.881	Full cone, wide angle	1.1 – 62.9	9.2

5.3.6 Concept F

Figure 5.8 presents the numerical results of Concept F. It can be seen from Figure 5.8(a) that water enters from the water inlet is separated into three streams and fed into a mixing chamber through the swirl insert. Water flowing spirally forward interacts with supplied air which spins in a reverse direction. Strong interaction and mixing happens between the two phases before they flow out from the nozzle orifice and this produces a full-cone spray. Figure 5.8 (b) highlights the droplets in spray and their sizes. Judging from the colour, nearly all the droplets in the spray are smaller than 30 μm . As is observed from numerical results of other design concepts, droplets with larger diameter can be found close to the edge of the spray. Figure 5.8 (c) shows the distributions of droplet and mean droplet size. Droplet distribution is quite even over the spray region. It is slightly diluted when the spray travels downstream and covers a larger area. No big change of mean droplet size is observed. Droplet collisions and coalescence are revealed at the edge of the spray, which causes an increase in droplet diameter. Figure 5.8 (d) clearly shows the constitution of droplets with different diameters at the outlet of the calculation domain. Nearly all the droplets have diameters less than 15 μm , which indicates the capability of this design concept to produce spray with fine droplets.

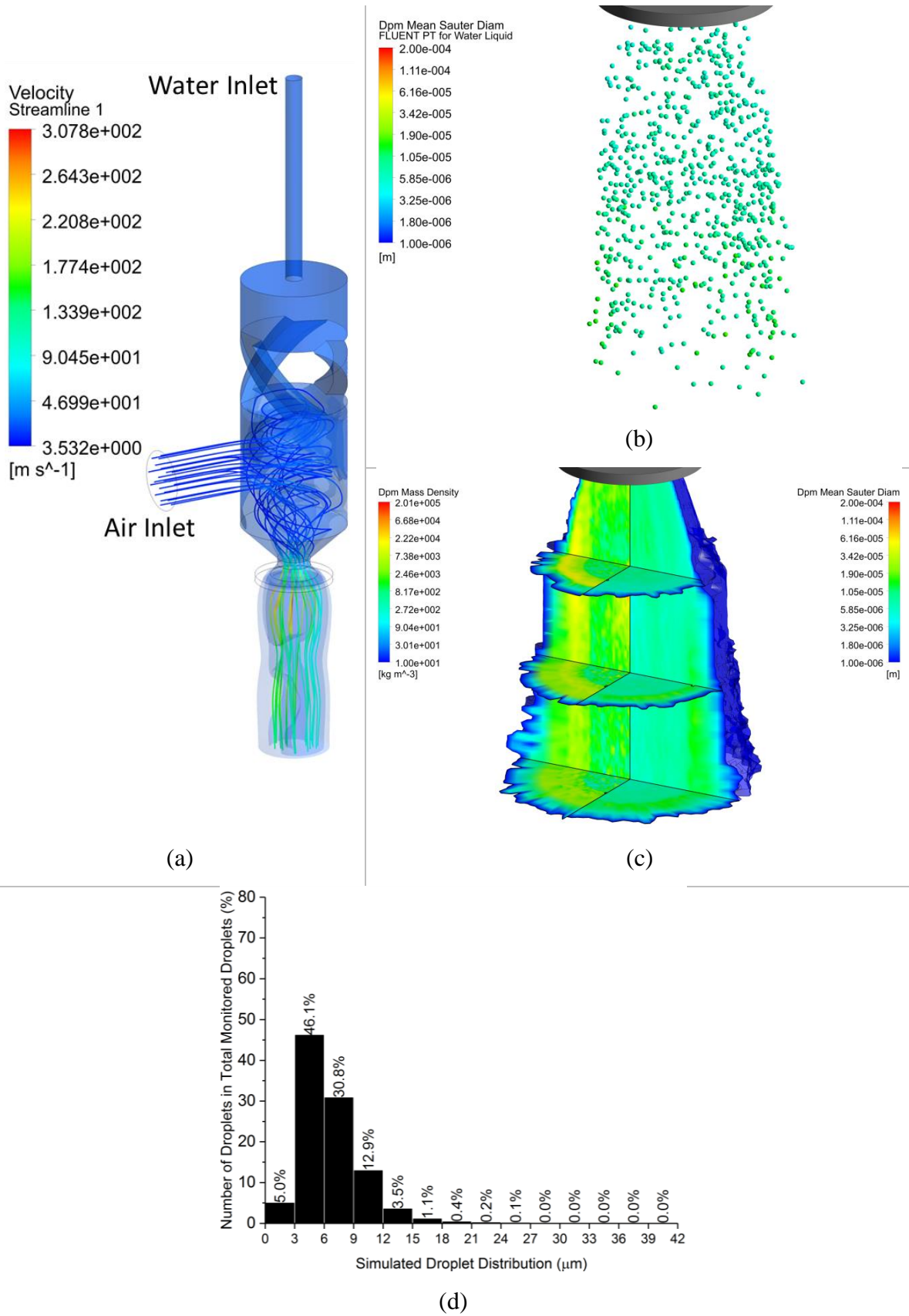


Figure 5.8 Numerical results of concept F: (a) volumetric distribution of water and streamlines of air velocity; (b) tracking of water droplets and their SMD values; (c) spatial distribution of water droplet number and mean droplet size; (d) histogram presenting diameter of droplets exiting the outlet of calculation domains.

Table 5-9 concludes the parameters of spray produced by concept F. This nozzle is able to generate spray with a water flow rate of 0.865 kg/s . Produced spray has a full-cone pattern. Sizes of the produced droplets range from $1.2 \text{ }\mu\text{m}$ to $37.8 \text{ }\mu\text{m}$ and the SMD value at the outlet of the calculation domain is $9.8 \text{ }\mu\text{m}$.

Table 5-9 Statistics information of spray generated by Concept F

Air Flow Rate (kg/s)	Water Flow Rate (kg/s)	Cone Pattern	Drop Size Range (μm)	Sauter Mean Diameter (μm)
0.068	0.865	Full cone, wide angle	1.2 – 37.8	9.8

After the numerical study is conducted for each of the nozzle design concepts, computational results of different spray characteristics are collected and listed in Table 5-10 so that a direct comparison between sprays generated by different nozzles can be made. Among these 6 concepts, concept E is able to produce a spray with smallest averaged droplet size. Concept D is estimated to produce the highest water flow rate during the atomization followed by concept A, F, and E. Air consumption is another important parameter in concept justification. If the design requires high volume of air for atomization, it is not supposed to work continuously over a long period or compressed air in gas tank will be exhausted quickly. Concept B among these 6 designs uses the greatest amount of air in the same period of time while concept A and E use the least. All the concepts produce sprays of full cone patterns. Sprays produced by design A, D, E, and F have wide spray angles. However, narrow angles are observed by sprays generated by concept B and C.

Table 5-10 Summary of numerical results from different design concepts

Parameters	Unit	Concept					
		A	B	C	D	E	F
Sauter Mean Diameter (SMD)	μm	16.8	20.1	11	15.1	9.2	9.8
Water flow rate	kg/s	0.980	0.488	0.028	1.351	0.881	0.865
Air flow rate	kg/s	0.027	1.501	0.539	0.72	0.035	0.068
Cone pattern		Full cone	Full cone	Full cone	Full cone	Full cone	Full cone
Spray angle		Wide	Narrow	Narrow	Wide	Wide	Wide

For the evaluation of the nozzle concepts, a weighted evaluation matrix was used to compare the 6 different nozzle design configurations as shown in Table 5-11.

Table 5-11 Evaluation table of nozzle design concepts

		Concept											
		A		B		C		D		E		F	
Evaluation Criteria	Weighting	s	W.S	s	W.S	s	W.S	s	W.S	s	W.S	s	W.S
SMD drop size	30	3	90	2	60	4	120	3	90	5	150	5	150
Water flow rate	30	4	120	3	90	1	30	5	150	4	120	4	120
Air usage	10	5	50	1	10	3	30	2	20	5	50	4	40
Covering area	20	5	100	1	20	1	20	5	100	5	100	3	60
Mixing	10	5	50	1	10	1	10	3	30	5	50	5	50
	100%		410		190		210		390		470		420
	Rank	3		6		5		4		1		2	

The evaluation criteria was defined by the computational result parameters and assigned a weighting based on the relative importance. In this case, the SMD droplet size and flow rate have the largest weighting respectively due to their importance for the aims of this research. Each nozzle concept was then scored (S) from a rating of 1-5 and a weighted score (W.S) calculated from the multiplication of the weighting and concept score. Next, the weighted score was totalled in order to determine the ranking of the evaluated nozzle concepts, in which the strongest concept has the highest rank and the weakest concept having the lowest rank. From Table 5-11, the ranking of the nozzle concepts is presented in the following:

- **Concept E: Air-swirl nozzle (strongest design)**
- Concept F: Twin-swirl nozzle
- Concept A: Right-angle nozzle
- Concept D: Pre-filming nozzle
- Concept C: Air-assist pressure-swirl nozzle
- **Concept B: Spill-return nozzle (weakest design)**

5.4 Initial Nozzle Design

According to results of concept evaluations presented in the previous section, an initial nozzle design was developed for multi-fluid atomization. This initial nozzle design adopts modular and adjustable features. As shown in Figure 5.9, the design is mainly made up of 5 modules. Each of the modules has a specific function to support the multi-fluid mixing and atomization process, these are:

- **Module 1:** provides nozzle inlets which are the main interface for different fluid sources to connect to the nozzle.
- **Module 2:** supports an internal volume which can be used either as a mixing chamber for the mixing or emulsifying of fluids or as a divider to separate fluids in to several streams.
- **Module 3:** sustains a modular section to integrate different nozzle design features such swirl or annular sections to influence the internal flow performance.
- **Module 4:** supports a secondary internal volume which can be used as the main mixing chamber for multiple fluids.
- **Module 5:** supports a nozzle orifice area to enable variation of the external atomisation performance by interchangeable components.

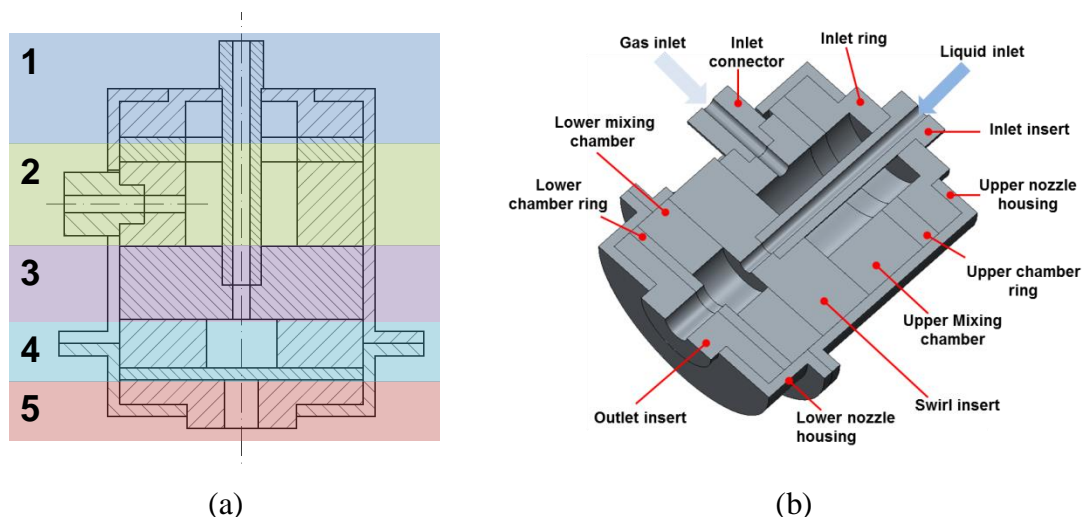


Figure 5.9 Modularisation of the initial nozzle design

Figure 5.9 (b) shows the 3D model of initial modular nozzle. This design includes a total number of 11 nozzle parts. Upper and lower housings are assembled to form a cylindrical cavity which aligns and fixes most of the other parts. The inlet insert for connection with a liquid source and inlet ring is secured at the upper housing. An

internal volume is comprised of an inlet ring, upper chamber ring, and upper mixing chamber for fluid mixing or separating in the nozzle. A recessed slot is provided on the side of the upper housing to provide an interface for a tangential inlet connector. A swirl insert is attached to the bottom of upper mixing chamber and followed by a lower mixing chamber which serves as the main location for multi-fluid mixing. The lower chamber ring and outlet insert are assembled at the outlet end of the lower housing. These two parts make up the nozzle orifice from which all the fluid flows out. All the internal parts are in ring shapes with identical outer diameter, which makes it simple to change the geometry of internal parts for different flow-path design. Modular nozzle design enables quick assembly and testing of the two most competitive design configurations in the numerical evaluation. Figure 5.10 illustrates the exploded view of the initial nozzle design.

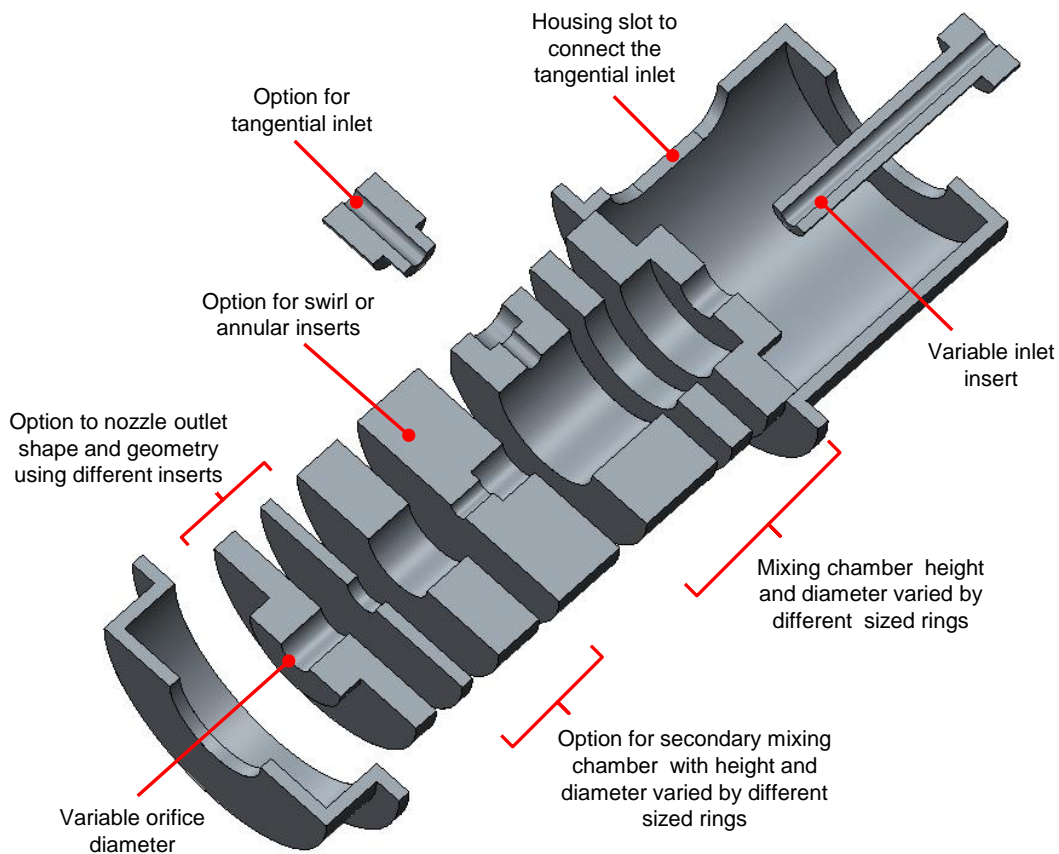


Figure 5.10 Exploded view of the initial nozzle design

5.5 Development of Third-Component Mixing Concept

The initial modular and reconfigurable nozzle was further developed in this study to support the mixing of a third component (fluid or solid particle). Figure 5.11 shows the two different mixing concepts considered in this study. These two concepts

feature internal mixing and external mixing respectively. In the internal mixing concept, an additional inlet directly leads the flow of solid particles (impulse by liquid or gas) into the internal chamber of the nozzle to obtain the final mixture of solution and solid particles. In the external mixing concept, the third component is introduced to the nozzle right before water-air mixture leaving the nozzle. Several particle inlets are designed at the nozzle orifice.

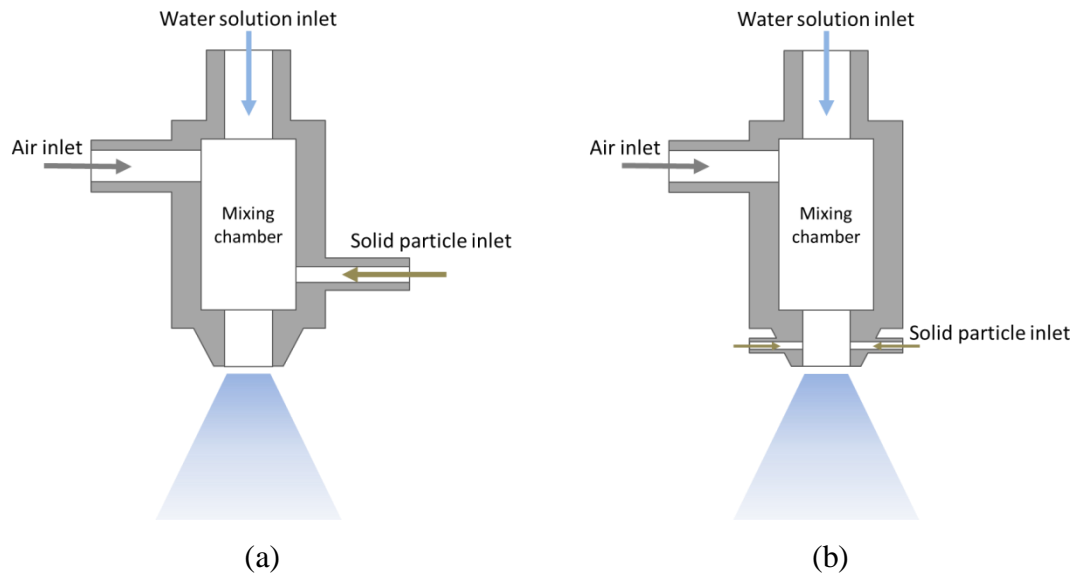


Figure 5.11 Third-component mixing concepts

Based on the two conceptual approaches, methods for third-component mixing are integrated into the initial modular nozzle design. Figure 5.12 presents the initial modular nozzle design integrated with third-component mixing features.

Figure 5.12 (a) is a nozzle design with internal mixing for the third component. For this configuration, a recess is to be cut into side of the lower nozzle housing for a threaded side inlet. The inlet is inserted and sealed into the second mixing chamber of the nozzle. Flow path for the third component is highlighted in red in Figure 5.12 (a). If the introduced third component is in the form of solid particles, it is also the highlighted area that is more likely to be physically eroded.

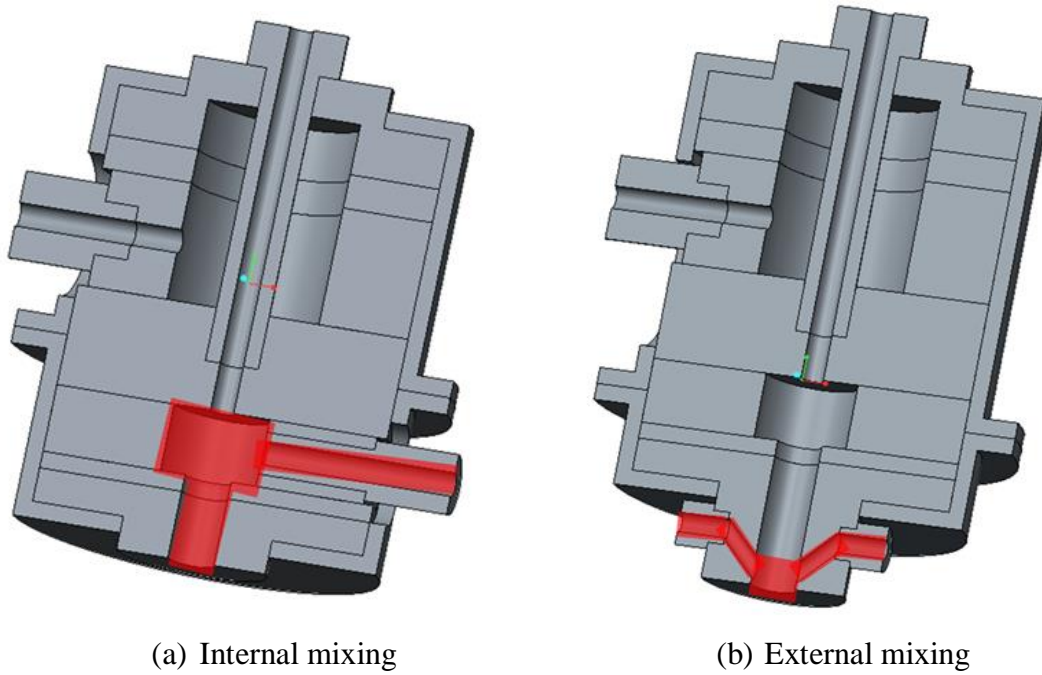


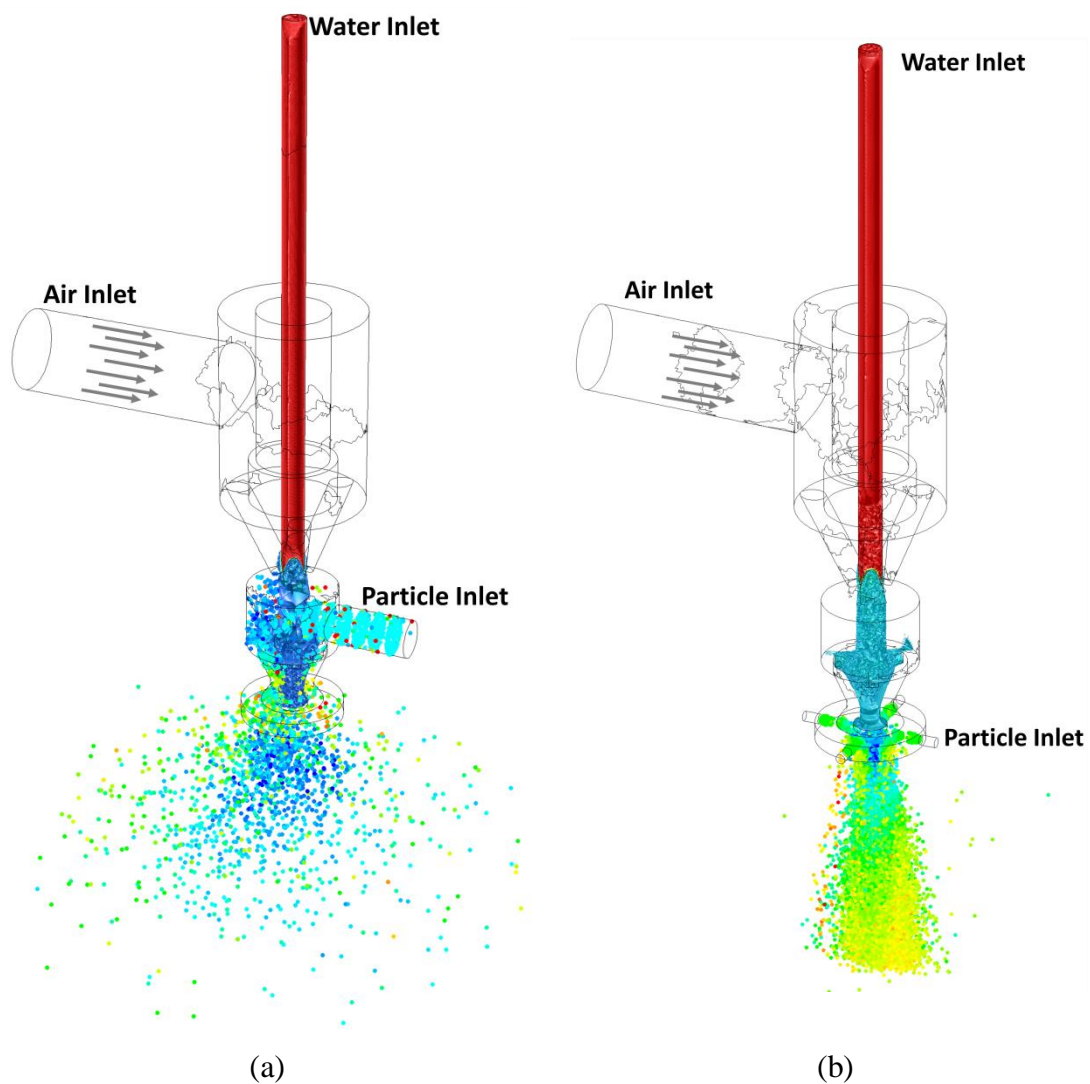
Figure 5.12 Modular nozzle designs with third - component mixing concepts

Figure 5.12 (b) shows the concept for external mixing. To feed the third component near the orifice of the nozzle the nozzle outlet is extended to support the connection of additional threaded side inlets for external mixing. Flow path for the third component is from inlet to nozzle orifice which is highlighted. Physical erosion caused by third component particles is expected in these nozzle parts.

Comparing these two design concepts for third-component mixing, it is expected that the internal mixing design will be subjected to more abrasive wear but the third component can be mixed more evenly in the spray. For the external mixing concept, internal nozzle parts are less likely to be eroded by the third component and only small modification is required on the initial design to support installation of additional inlets at the nozzle orifice.

CFD simulations were used to study and compare the performance of multi-fluid nozzle designs with different third-component mixing methods. For both methods, water and air were supplied into the nozzles through different inlets. Twin-fluid interaction and mixing happened when the two fluids met in the second chamber. For internal mixing design, the third component was introduced to the nozzle at this stage of the atomizing process. The three components were fully mixed before being atomized from the nozzle orifice. Figure 5.13 (a) shows the computational results of the internal mixing nozzle. For the external mixing configuration, the twin-fluid

mixture at the second nozzle chamber hits the pin at the bottom of the chamber and flows further downstream before meeting the third component at the nozzle orifice and generating spray. The external mixing process was simulated and is presented in Figure 5.13 (b). It can be seen that with internal mixing the third component is more evenly mixed with other two components in the generated spray. Also it is spread more widely. Internal mixing concept is therefore selected as the design for introducing the third component into nozzle. Figure 5.14 shows an exploded view drawing of the modular nozzle design with the third-component mixing concept.



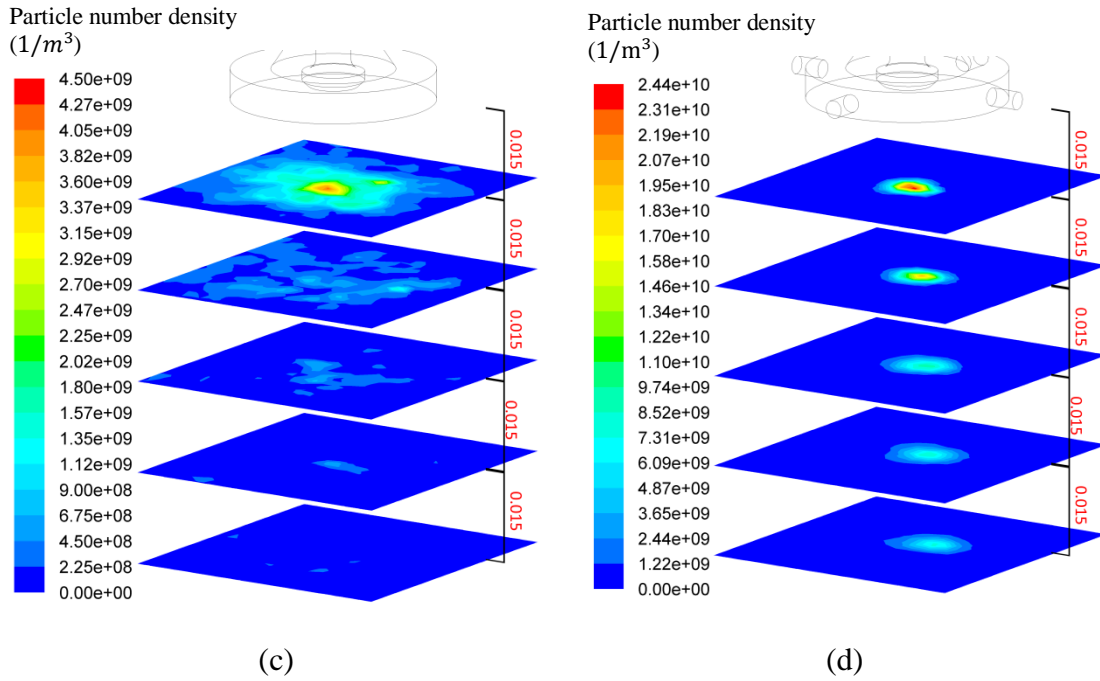


Figure 5.13 Numerical results of CFD simulations for different third-component mixing concepts

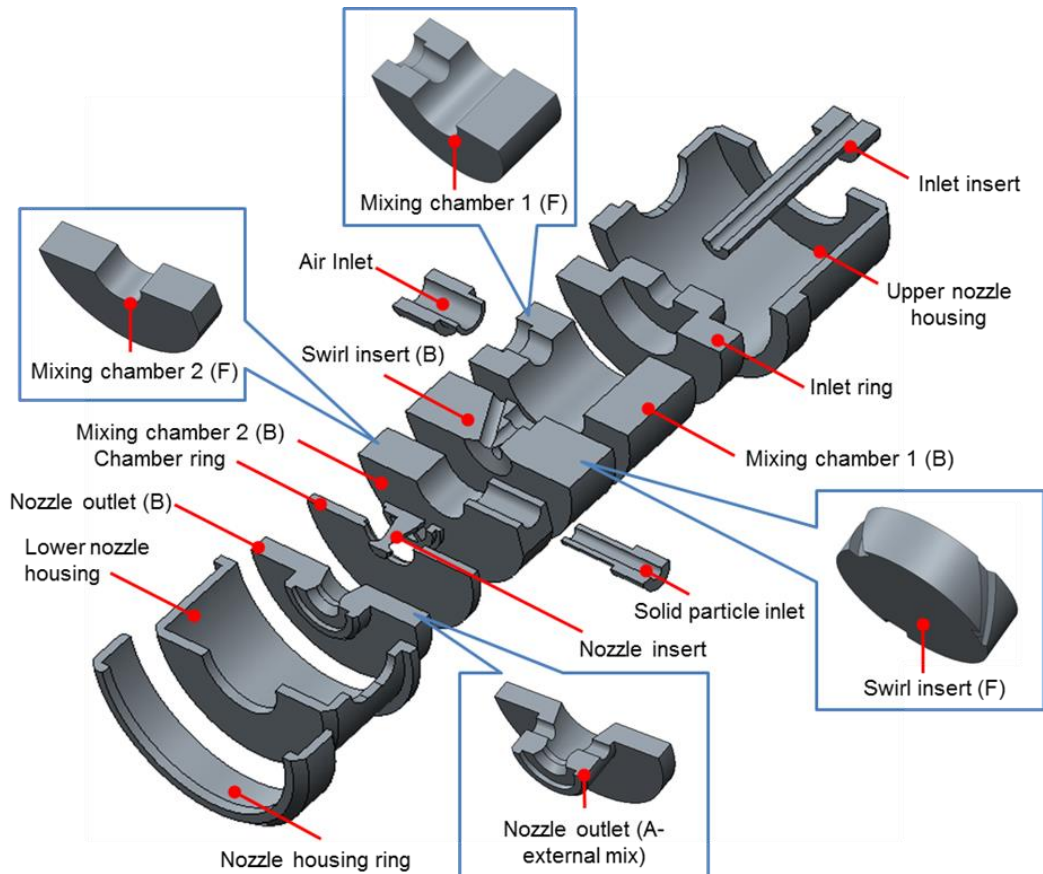


Figure 5.14 Modular nozzle design with third-component mixing concept





5.6 Numerical Optimization of Design Dimensions

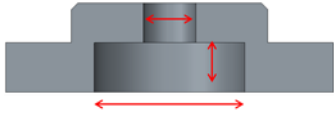
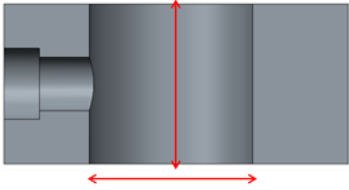
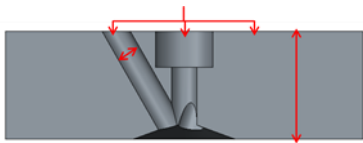
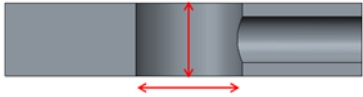

In the detail development of nozzle components, the task was to select the key design parameters for each module and the range of dimensions in which they could be

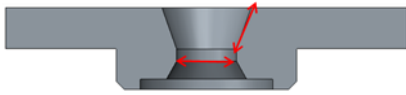

configured, these will influence of the adjustable fogging performance of the nozzle. Firstly, the key design parameters were selected based on findings from the literature review and from the initial CFD studies carried out in section 5.3. Following this, a selected range of dimensions for each design parameter was selected, which will be evaluated in the following stage of the CFD numerical studies.

Table 5-12 presents an overview of the main design parameters that can be configured for the internal nozzle components and these were used to create the parametric 3D CAD model of the spraying nozzle. The red-highlighted design parameters indicate the identified design features which are most critical in influencing the fogging performance of the nozzle design.

Table 5-12 Design parameters of different nozzle components

Module	Component (cross - section)	Description	Design Parameter (DP)	Range of value
Nozzle Housing	<p>Upper housing</p> 	Upper housing to locate and assemble the internal nozzle components	<i>Not configurable</i>	N/A
	<p>Lower housing</p> 	Lower housing to locate and assemble the internal nozzle components	<i>Not configurable</i>	N/A
	<p>Housing ring</p> 	Housing ring used to assemble and lock the upper and lower nozzle housing	<i>Not configurable</i>	N/A
Module 1	<p>Inlet insert</p> 	Provides inlet for water / fluid	<i>Not configurable</i>	N/A

	<p style="text-align: center;">Inlet ring</p> 	<p>Provides interface for inlet insert and mixing chamber 1</p>	<p><i>Not configurable</i></p>	<p>N/A</p>
<p>Module 2</p>	<p style="text-align: center;">Chamber 1</p> 	<p>Provides internal volume for the mixing /emulsifying of fluids and interface for air inlet</p>	<p><i>Not configurable</i></p>	<p>N/A</p>
<p>Module 3</p>	<p style="text-align: center;">Swirl insert</p> 	<p>Provides support for integration of swirl insert to influence internal flow performance can be interchanged with different types of swirl inserts</p>	<p><i>Swirl angle</i></p>	<p>25° - 31°</p>
<p>Module 4</p>	<p style="text-align: center;">Mixing chamber</p> 	<p>Provides secondary internal volume for mixing / emulsifying of fluids and optional interface for solid particle inlet</p>	<p><i>Mixing chamber height</i></p>	<p>15 mm – 25 mm</p>
	<p style="text-align: center;">Chamber ring</p> 	<p>Provides interface to assemble nozzle insert and also can be used the adjust the size of mixing chamber</p>	<p><i>Not configurable</i></p>	<p>N/A</p>

Module 5	Nozzle outlet 	Main nozzle orifice area at which atomisation occurs	<i>Orifice angle</i>	N/A
			<i>Orifice diameter</i>	12 mm – 16 mm
	Nozzle insert 	Used to enable variation of the atomisation performance	<i>Insert diameter</i>	4 mm – 8 mm

After the design parameters of the nozzle components had been recognized, a 3D geometry was built to represent the internal flow channel formed by the nozzle assembly. Figure 5.15 shows the internal volume of the nozzle. Changes on dimensions of nozzle components affect the generated spray by modifying the geometry of the flow channel. Hence recognized design parameters are reflected by internal-volume geometry.

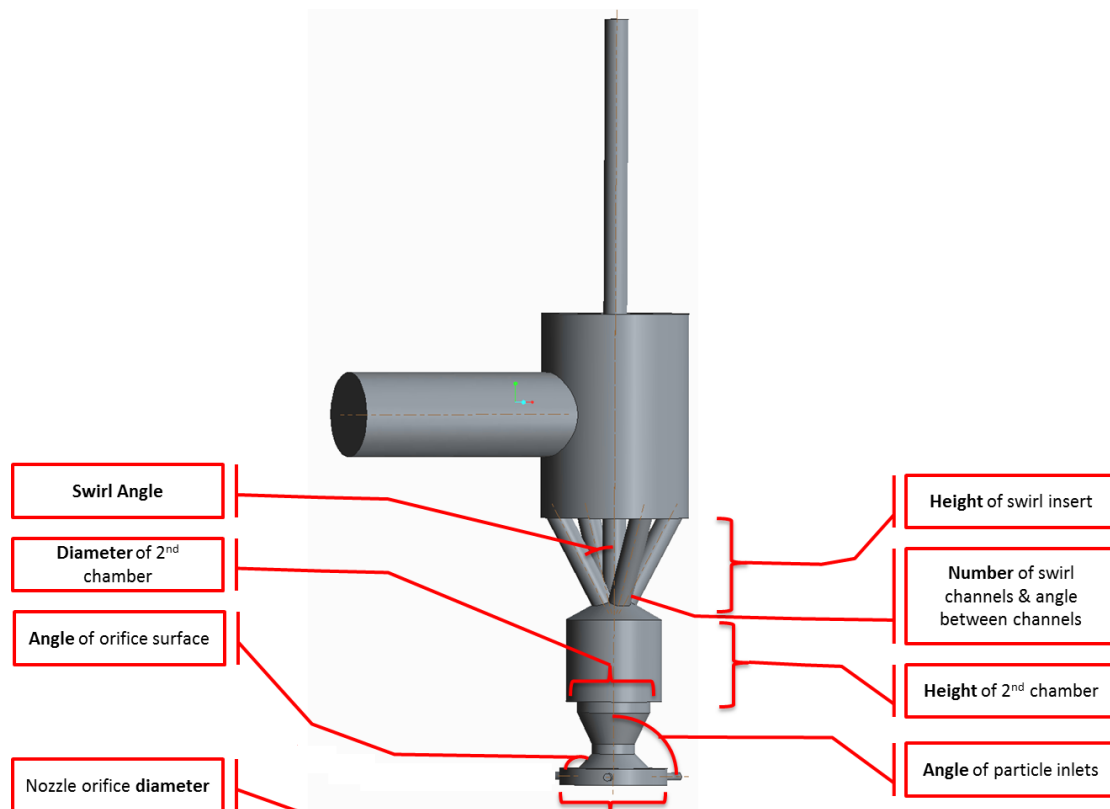


Figure 5.15 Design Parameters (DPs) projected on internal volume of nozzle assembly

Detailed values of simulation points for different design parameters are listed in Table 5-13. Considering the amount of simulations needed to be carried out, parametric geometry is used in simulations with the help of the proposed CFD model. CFD

settings and boundary condition settings are the same as the ones used for concept evaluation in section 5.2, which are listed in Table 5-1. A multiphase model of the mixture is used to take care of air-water interaction in the whole flow-field simulation in both internal and external domains. A realizable k-epsilon model with scalable wall functions is adopted to simulate any turbulence generated during the multiphase interaction. Total Pressures at the two inlets are set as 728,080 Pa for air and 1,044,084 Pa for water. A no-slip wall condition is assigned to the internal walls of the nozzle while the boundaries of the external calculation domain are designed as pressure outlets with 0 Pa gauge pressure. For the droplet dynamic simulation, DPM with droplet models of breakup, collision, and coalescence is used to predict the behaviour of water particles. Air and water pressures obtained from whole flow-field simulation are applied to the inlets. Water particles are reflected if they hit the internal walls and escape if they reach the borders of the external spray region.

Table 5-13 List of Design Parameters (DPs) and their design points

Design Parameters (DPs)	Simulation points
Nozzle orifice inner diameter (mm)	4, 5, 5.6, 7, 8
Nozzle orifice outer diameter (mm)	12, 13, 14, 15, 16
Height of 2nd chamber (mm)	15, 18, 20, 22, 25
Diameter of 2nd chamber (mm)	25, 28, 39, 29.2, 30, 32
Number of swirl channels	3, 4
Swirl angle (°)	25, 28, 30, 31
Height of swirl insert (mm)	28, 31.5, 33

Table 5-14 lists results of parametric simulation for studying the effects of different design parameters on nozzle performance. The results are highlighted in red if finer droplets or higher flow rates are produced by the increasing parameter. While for larger droplets or lower flow rates are generated with increasing parameter, the results are highlighted in green. There are still some parameters that are not closely related to nozzle performance and they are highlighted in grey. By analysing all these data, it can be seen that the nozzle orifice has an effect on both produced droplet size and flow rate. Higher flow rates can be obtained with a larger gap between the nozzle inner and outer diameter while droplet size will also increase. The produced droplet is

also sensitive to the design of swirl while flow rate is more strongly affected by the design of the chamber and channel.

Table 5-14 List of numerical results studying the effect of design parameters on nozzle performance

Design Parameters (DPs)	Simulation points	SMD Drop Size (μm)	Water Flow Rate (kg/s)
Orifice inner diameter (mm)	4	10.7	0.878
	5	10.6	0.875
	5.6	8.8	0.873
	7	7.8	0.867
	8	5.2	0.862
Orifice outer diameter (mm)	12	3.8	0.844
	13	5.7	0.864
	14	8.8	0.873
	15	9.1	0.876
	16	13.7	0.887
Height of 2nd chamber (mm)	15	9.0	0.871
	18	8.1	0.873
	20	9.8	0.870
	22	9.2	0.873
	25	9.2	0.873
Diameter of 2nd chamber (mm)	25	8.1	0.870
	28	9.4	0.872
	29	9.2	0.873
	29.2	8.8	0.873
	30	8.9	0.876

	32	8.7	0.887
Number of swirl channels	3	8.8	0.873
	4	8.8	0.933
Swirl angle (°)	25	10.0	0.877
	28	9.8	0.871
	30	8.8	0.873
	31	7.9	0.872
Height of swirl insert (mm)	28	9.1	0.879
	31.5	8.8	0.873
	33	6.3	0.872

The numerical results of flow rates and droplet sizes from different nozzle parameters are plotted in Figure 5.16. From the bottom left to the top right corner of the graph, droplet size increases with increasing water flow rate. The goal of this parametric study is to select design parameters for nozzle performance locates at the top left corner of the graph which represents fine droplet and high flow rate. According to the optimized performance zone in the figure, orifice inner diameter, diameter for the 2nd mixing chamber, and swirl angle are selected as 8 mm, 32 mm and 31°. The orifice outer diameter is selected as 14 mm because the nozzle insert has a tip with a diameter of 13 mm. It will cause problem in nozzle assembling if the orifice outer diameter is too small. The height of the swirl insert is designed as 31.5 mm. With a height of 33 mm, the top part of the swirl channels will extend to outside the mixing chamber, which makes it not possible for machining. After analysing these parametric results and the machining capability, a set of optimized dimension values have been selected and listed in Table 5-15.

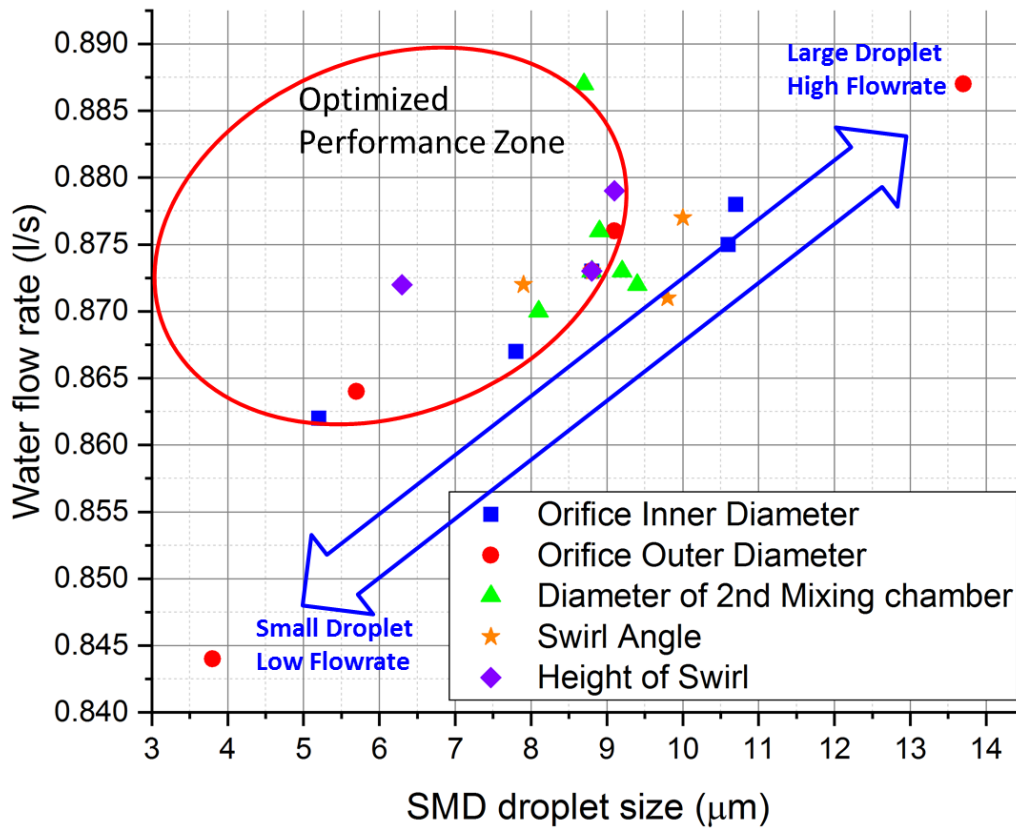


Figure 5.16 The numerical results of the parametric study

Table 5-15 Optimized parameters for nozzle design

Orifice inner diameter (mm)	Orifice outer diameter (mm)	Diameter of 2 nd chamber (mm)	Number of swirl channel	Swirl angle (°)	Height of swirl insert (mm)
8	14	32	3	31	31.5

From Figure 5.17 and Table 5-16, it can be seen that with optimized parameters, the nozzle is able to reduce the droplet size without having too much influence on flow rate. However, the water flow rate is still quite low compared to requirements for advanced nozzle design. Structural analysis and optimization has to be done to improve the nozzle performance on flow rate.

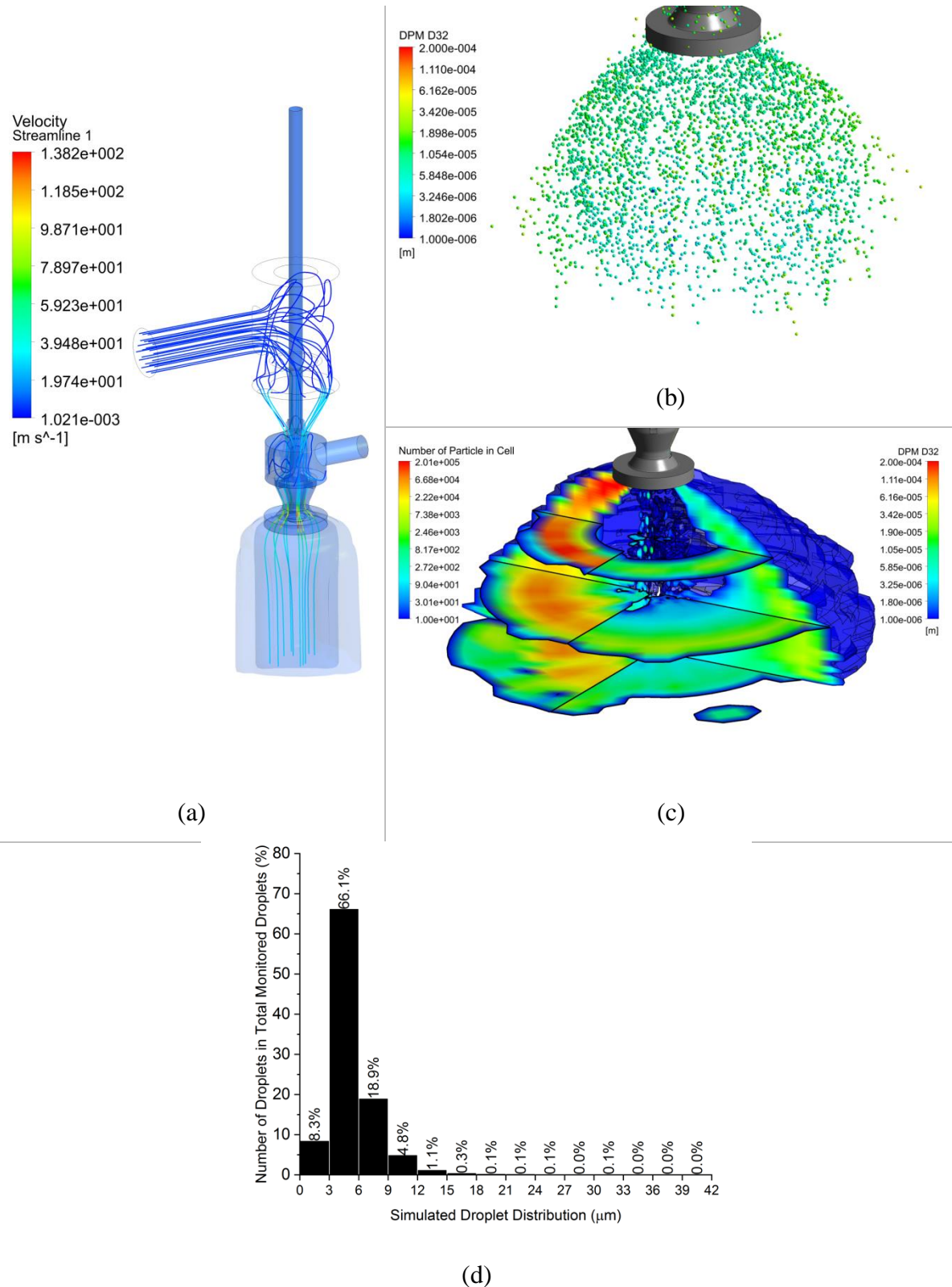


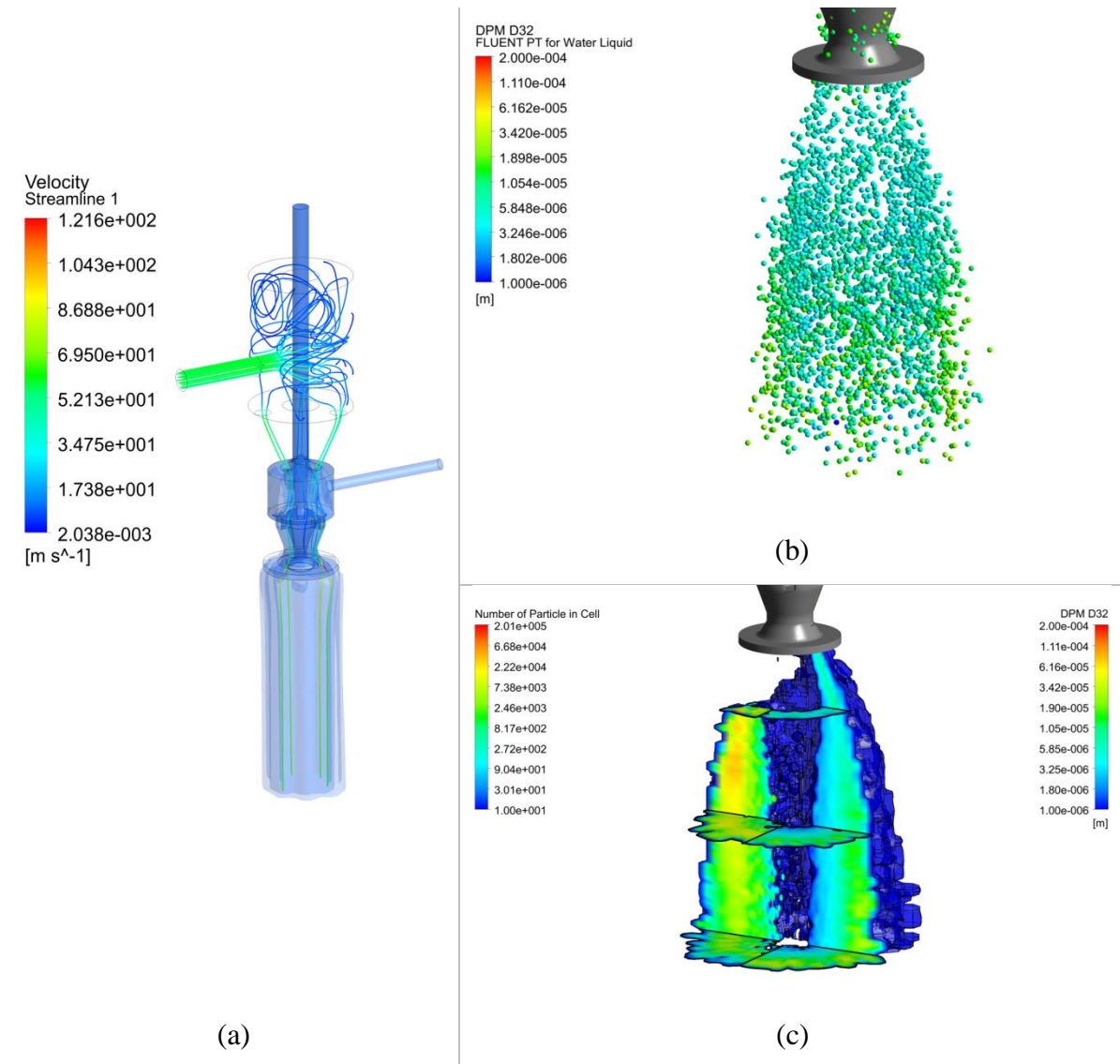
Figure 5.17 Numerical results of design with optimized parameter: (a) volumetric distribution of water and streamlines of air velocity; (b) tracking of water droplets and their SMD values; (c) spatial distribution of water droplet number and mean droplet size; (d) histogram presenting diameter of droplets exiting the outlet of calculation domains.

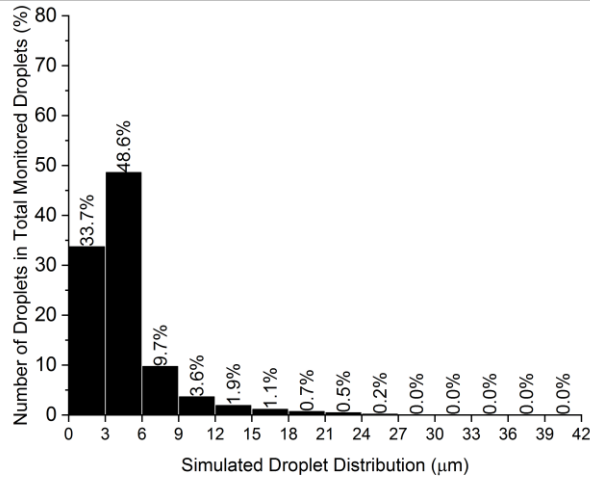
Table 5-16 Statistics information of spray generated by design with optimized parameter

Water Flow Rate (kg/s)	Cone Pattern	Drop Size Range (μm)	Sauter Mean Diameter (μm)
0.854	Full cone, wide angle	1.2 – 29.4	8.1

5.7 Numerical Investigation of Nozzle Size Effect

Another aspect affecting the performance of the nozzle is its scale. Obviously, designs with exactly the same structures perform differently if their sizes are different. Smaller nozzles with more narrow flow channels are expected to provide less water flow over the same period of time compared to their larger counterparts. This section is designed to present the effect of nozzle size on spraying performance. Sprays produced by the nozzle having half of the original size is numerically studied (Figure 5.18).





(d)

Figure 5.18 Numerical results of half size nozzle: (a) volumetric distribution of water and streamlines of air velocity; (b) tracking of water droplets and their SMD values; (c) spatial distribution of water droplet number and mean droplet size; (d) histogram presenting diameter of droplets exiting the outlet of calculation domains.

Parts in the 1st detail design are scaled to half of its original sizes individually. Then these scaled parts are assembled together. The internal volume of this assembly is obtained for CFD modelling. Setting and boundary conditions are defined the same as they are in previous studies.

From these numerical results (Table 5-17) it is noticed that by scaling down sizes of the nozzle by half, flow through the nozzle is reduced to ¼ of the original nozzle, while the scale effect on droplet size is not significant. Nozzle flow rate can be increased by scaling up nozzle dimensions. However, it would be difficult to install a nozzle which is too large in size.

Table 5-17 Statistics information of spray generated by half size nozzle

Water Flow Rate (kg/s)	Cone Pattern	Drop Size Range (µm)	Sauter Mean Diameter (µm)
0.232	Full cone, wide angle	0.6 – 25.0	11.4

After all the nozzle investigations, simulations, and optimizations, details of the nozzle flow path have been integrated into the modular design concept. Figure 5.19 shows the detail design for the optimized multi-fluid atomizing nozzle.

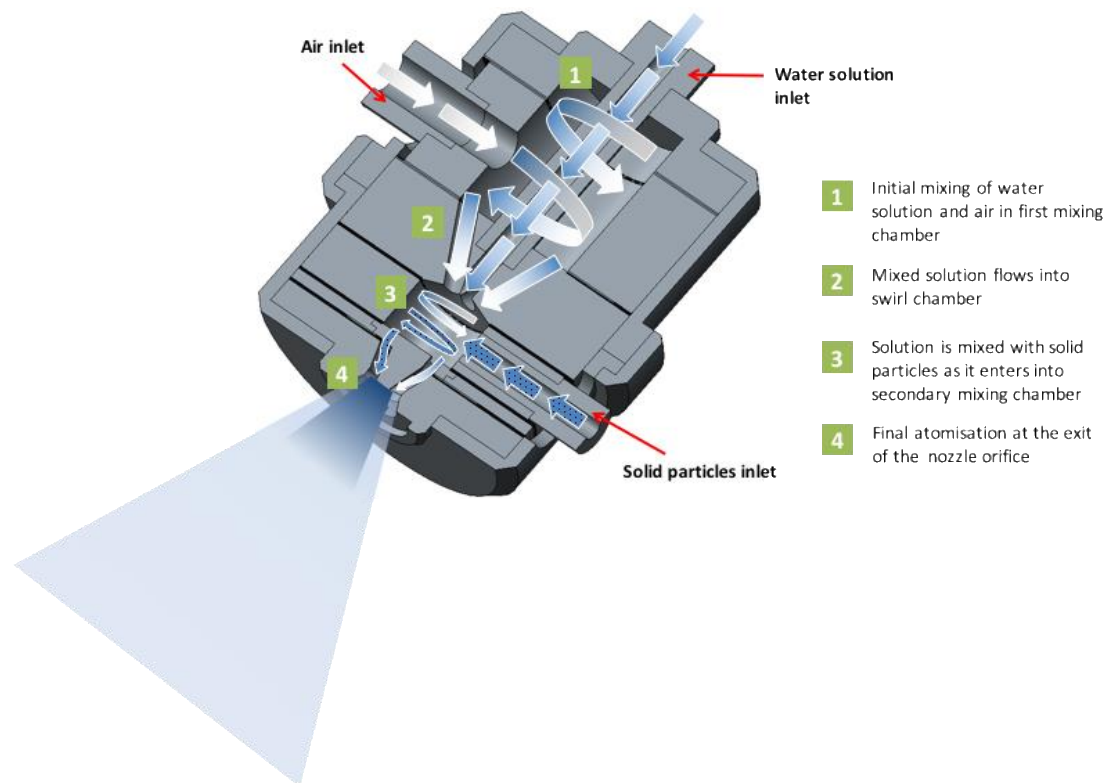


Figure 5.19 Detail design of multi-fluid atomization nozzle

5.8 Summary

This chapter presents the nozzle development process in great detail. For developing the advanced nozzle design:

- Concept generation has been achieved by considering 6 different nozzle designs featuring different configurations.
- Concept evaluation has been achieved by using the proposed CFD simulation system to calculate flow conditions, spray patterns, flow rates, droplet sizes and droplet distributions generated by the 6 nozzles. A weighted evaluation matrix has been used to select the design for conducting further design optimization.
- Initial nozzle design has been developed using the concept of modular design. In this case the design can be changed easily if further modification is required.
- For the third-component mixing concept, two different designs have been considered which are internal mixing and external mixing. These two concepts have been evaluated by a proposed CFD calculation system. In regards of better third-component mixing the internal mixing concept has been adopted;

- Nozzle dimension optimization has been finished with the aid of a proposed CFD calculation system combined with parametric simulation. About 30 simulations have been finished to investigate the effect of selections of different swirl, chamber, and orifice dimensions on the performance of the nozzle. Final dimensions for an optimized nozzle have been selected and nozzle performance has been predicted;
- The effect of nozzle size has been studied to investigate performance of a scaled nozzle. It is noticed that by scaling the nozzle design by half the produced flow rate will be reduced to a quarter of the original value while the effect on generated droplet sizes is not significant.

Chapter 6

Atomization Tests and Model Validation

Although detailed functional dimensions for the nozzle design have been decided, the nozzle is still lacking in details with regard to assembly, fabrication, and connection with test rig. In this chapter, focus will be put on:

- Detail design and redesign of components for assembly and fabrication.
- Setup of test rig for fog dynamic experiments.
- Experimental results which study the angle, flowrate, and droplet size produced by the manufactured nozzle.
- CFD model validation and error analysis.

6.1 Detailed Design of the Atomizer

6.1.1 Design for Manufacturing and Assembly

As was described in the previous chapter and shown in Figure 5.9, the designed nozzle features a modular configuration. For flow channels obtained through the assembly of a number of components, one key detail design consideration is the sealing and joining of internal components and assembly interfaces within the nozzle housing. This is important to prevent drops in the pressure due to leakage of the fluid

and air during operation and also seal any crevices between the modules which could cause long-term of corrosion of the nozzle.

For sealing of the nozzle, static O-ring seals are considered due to no relative motion between mating surfaces of the internal components. As the nozzle design will experience internal pressure during operation, it is proposed to apply static axial seals at each mating component interface. Figure 6.1 shows the general O-ring design for static axial internal pressure sealing, in which A specifies the O-ring diameter, G is the gland width and H is the gland depth [84].

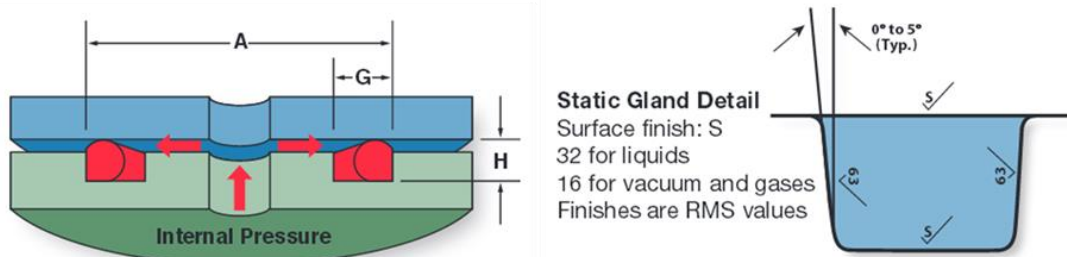


Figure 6.1 Static axial internal pressure design of O – Ring [84]

For sealing the nozzle insert and inlet components which are inserted to the main body of the nozzle, static radial O-ring seals are considered. A bore (piston) type O-ring seal is used for the radial sealing of these components. Figure 6.2 shows the different locations of static axial and radial O-Ring sealing on the cross-section of nozzle design.

One important reason for designing the nozzle as modular architecture is that the nozzle can be easily assembled and disassembled to support different nozzle design configurations. In the detailed design, the cylindrical internal components are assembled along a main vertical axis based on the upper and lower housing of the nozzle. To enable accurate location and permit ease of assembly/disassembly, a location/transitional fit is considered for the assembly interface between the upper/lower housing (H6) and the individual internal components (h6).

To join and secure the nozzle assembly, the flange interface of the upper and lower housings is fastened by 4x M8 nuts and bolts as shown in Figure 6.2.

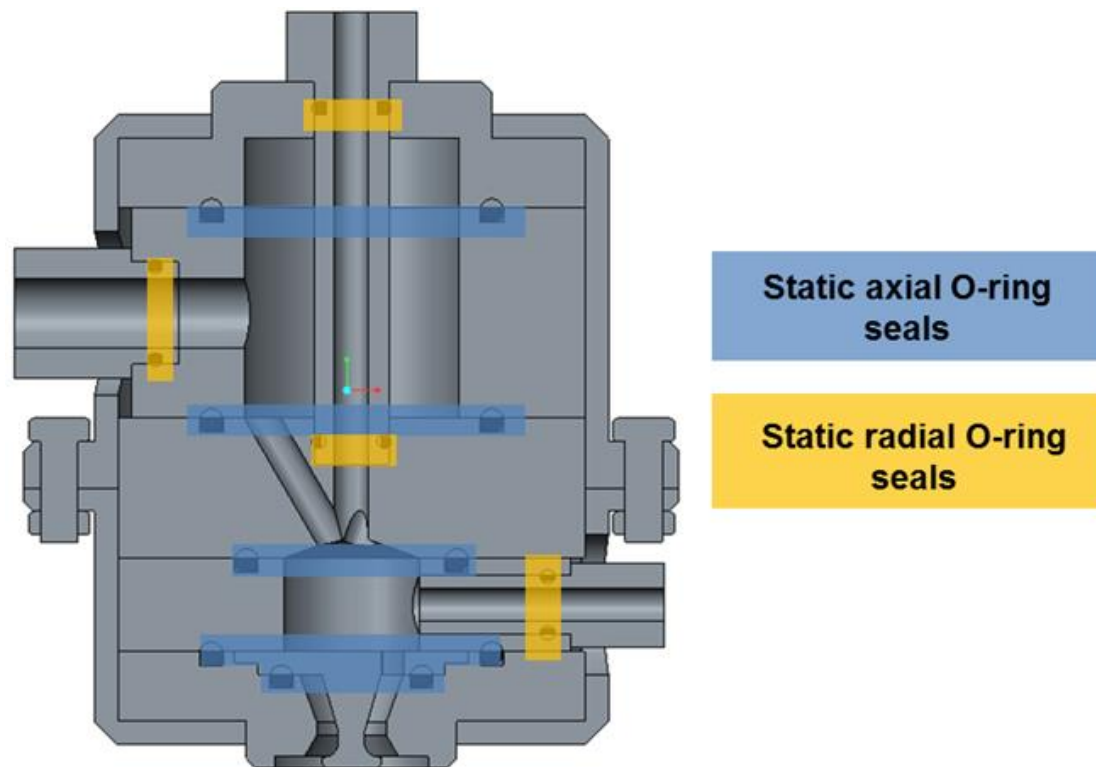


Figure 6.2 Selections of static axial seals and radial seals in the nozzle design

The material selection for different nozzle components is influenced by various factors from the temperature range, corrosion, and manufacturability. Common materials for nozzles include brass, bronze, cast iron, stainless steels, nickel-based alloys to a wide range of plastics (PTFE, PVC, ABS etc.). Aiming at producing sprays of fine droplet, high flow rate, and multiple components, the most important consideration for material selection is abrasion from the effect of the high-pressure and high-velocity flow stream mixing of solid particles. Abrasion is expected to affect the mixing chamber 2, nozzle outlet, nozzle insert, swirl insert, and solid particle inlet more significantly. Based on the abrasion resistance requirements, the following potential nozzle materials are considered for nozzle components:

- Hardened stainless steel
- Hard alloys – Cobalt alloy, Tungsten carbide
- Ceramics – Silicon carbide, Boron carbide

Whilst providing excellent resistance to abrasion, hard metal alloys and ceramic materials are also difficult to manufacture, especially if complex geometric features are required in the nozzle.

For the manufacture of the nozzle for testing, it is proposed to select stainless steel as the main material for the nozzle components to enable ease of manufacture. This would enable an initial prototype of the nozzle to be manufactured easily to support early testing and validation of the nozzle. Table 6-1 provides a summary of the material selection considerations for nozzle detailed design.

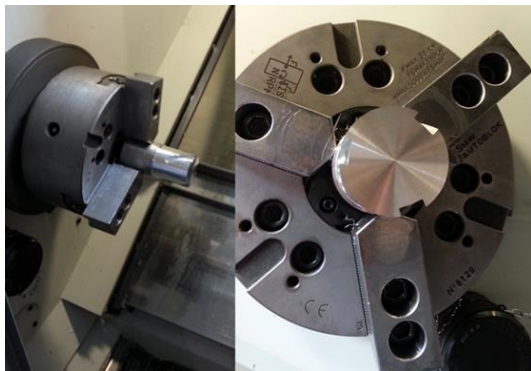
Table 6-1 Material selection for different nozzle components

Module	Component	Material	Remarks
Nozzle Housing	Upper housing	Stainless Steel	The outer surface of the upper and lower nozzle should be resistant to chemical corrosion during operation
	Lower housing	Stainless Steel	
1	Inlet insert	Stainless Steel	The inner and outer cylindrical surface will experience some abrasion and wear from the flow of fluid / solutions
	Inlet ring	Stainless Steel	The internal walls will experience some abrasion and wear from the mixing of solutions
2	Mixing chamber 1	Stainless Steel	The internal walls will experience some abrasion and wear from the mixing of solutions
3	Swirl insert	Stainless Steel	The small swirl channels of the insert will be subjected to abrasion and wear from the flow of fluid / mixed solutions
4	Mixing chamber 2	Stainless Steel	The internal walls will be subjected to abrasion and wear from solid particles from internal mixing nozzle configuration.
5	Nozzle outlet	Ceramic	Expected area of highest abrasion and wear in the nozzle from the atomisation and mixing of solution and solid particles
	Nozzle insert	Ceramic	The outer surface of the nozzle insert will be subjected to high levels of abrasion and wear from the resulting atomisation process

Inlet	Water inlet	Stainless Steel	The inner and outer surfaces should be resistant to chemical corrosion during operation
	Air inlet	Stainless Steel	
	Solid particle	Ceramic	The inner channel of the inlet will be subject to abrasive wear from the supply of solid particles

6.1.2 Manufacturing of Nozzle Components

After the detailed design of the nozzle was completed and material for each component was selected, the nozzle parts were manufactured as designed using the selected materials. Figure 6.3 shows the production of the swirl insert with stainless steel and the nozzle insert with ceramic. However some problems relating to manufacture occurred when the parts were produced. Figure 6.4 shows some of the problems on specific nozzle components. It is indicated that the initial detail design was not considerate enough for the nozzle assembly process, the machining process and available machine tools.



(a)



(b)

Figure 6.3 Manufacture of swirl insert and nozzle insert

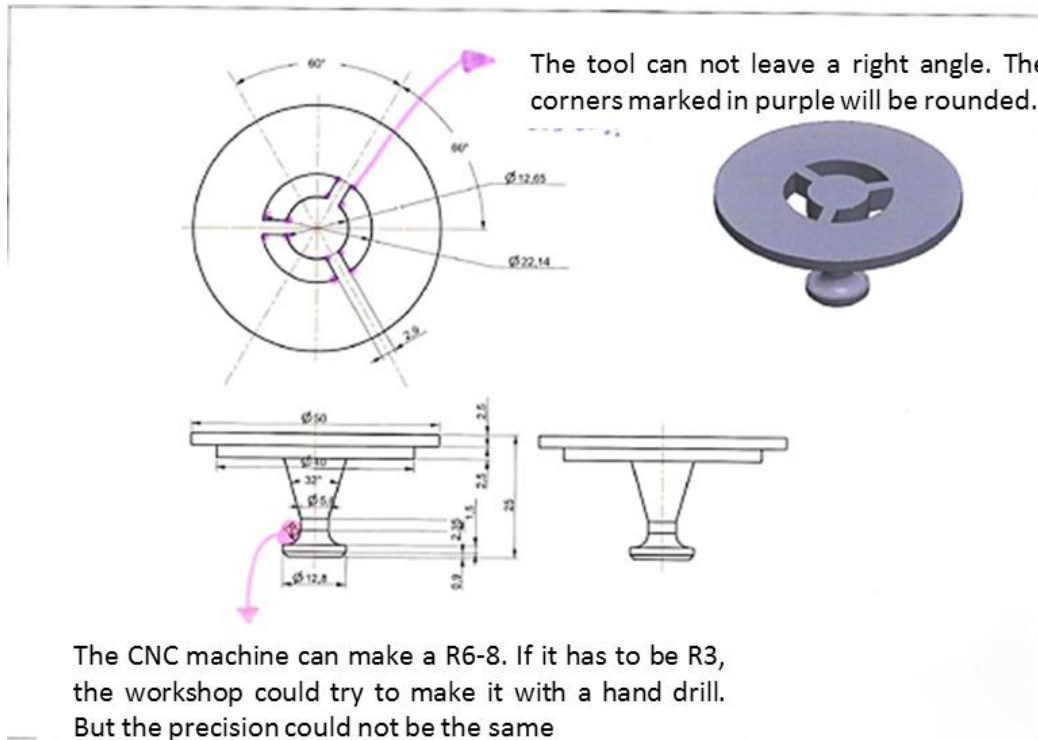


Figure 6.4 Problems occurred when producing nozzle components

A list of requirements for component modifications has been generated as following:

- In order to make the parts assembly process easier, the nozzle should have a housing with a cylinder and a cap which are connected by screws and nuts.
- Enough space should be ensured for the screw and nuts to be assembled especially when a hexagonal shape screw head is used.
- O-rings in radial positions in threaded parts and thin walls which can be weakened should be avoided in the nozzle design.
- Rounded corner features should be considered to avoid interference between parts when assembled.
- Radius for rounded corner should consider the machining capability of the CNC machine. The Radius on the nozzle insert should be increased from R3 to R6 – 8.
- The corners with right angle at the slots of nozzle insert are not achievable by milling. Rounded corners should be included in the design.

6.1.3 Redesign of Nozzle Components

According to the advice on modifying nozzle components, updates were made to improve the nozzle design. The first modification on nozzle design was to redesign

the method for sealing the nozzle insert and inlet components. In order to avoid grooves in threaded parts which can weaken the parts, static crush seals were introduced to replace the design of static radial O-ring seals. Figure 6.5 shows the updates in the nozzle design for sealing between components.

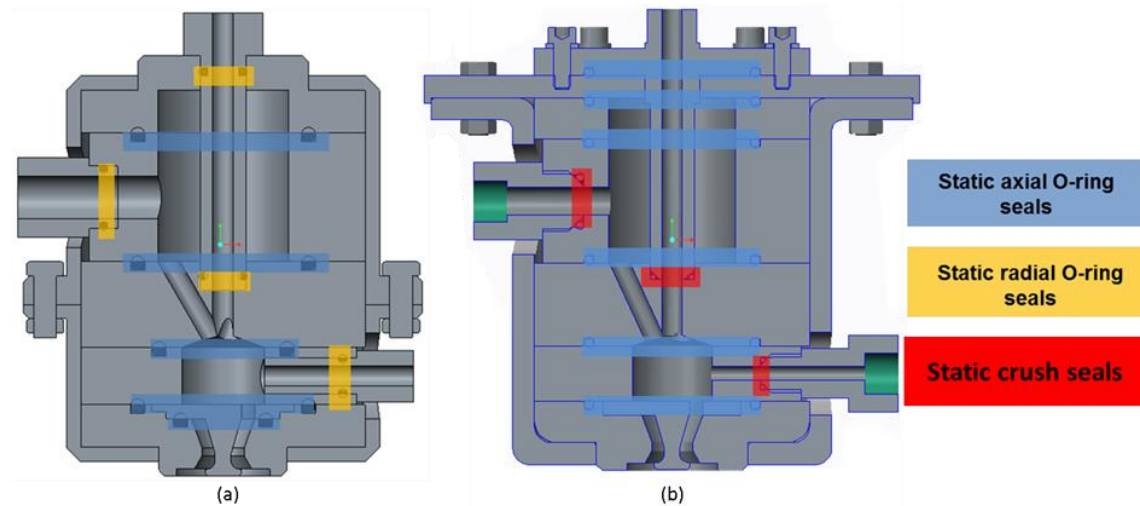


Figure 6.5 Updates of sealing mechanism and housing design in the nozzle design

In addition to the redesign of nozzle sealing, Figure 6.5 also shows the redesign of the nozzle housing. In the original detailed nozzle design, a doubled ‘U-Cup’ housing design was used, Figure 6.5 (a). However, regarding this configurations, assembly of the internal components within the housing are difficult. From the feedback, it was suggested that a housing with a cylinder and a cap is more reasonable for nozzle assembly and internal-component alignment, which helps with the redesign of the housing shown in Figure 6.5 (b).

Design of the nozzle insert was also modified considering the machinability (Figure 6.6). The radius of curvature on the nozzle tip is adjusted to fit the manufacturing method. Also rounded corners are added to every slot located at the bottom base of the nozzle insert. When considering assembly issues, steps on the edge of the insert base are removed and replaced by a straight plate, which reduces the requirement for fit tolerance.

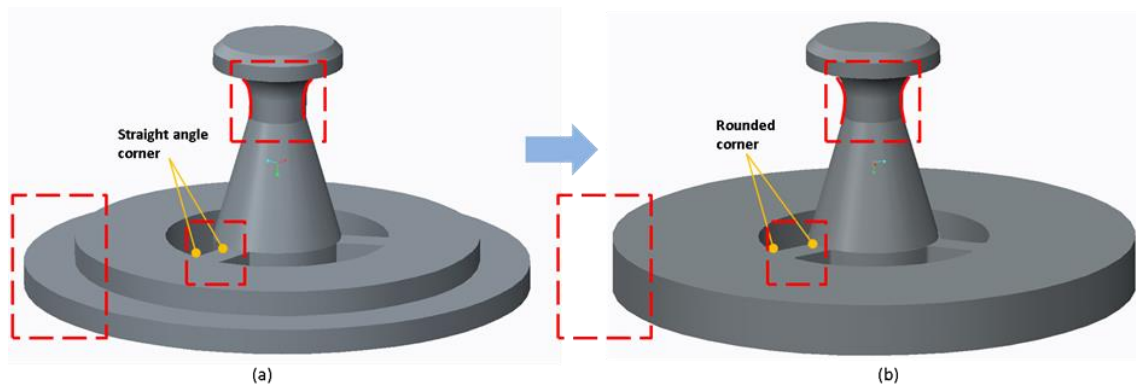


Figure 6.6 Design modification made on nozzle insert

Apart from the mentioned design modifications, other component redesigns such as radii on rounded corners to avoid part interference and inlet channel redesign to make the assembly more convenient were also conducted. Figure 6.7 shows the assembly of the designed nozzle.



Figure 6.7 Assembly of the designed nozzle

6.2 Spray Dynamic Experiments of Atomizer

6.2.1 Experimental Setup

After the parts of the finalized nozzle design were manufactured and assembled, functionality of this modular nozzle was tested in a fog dynamics lab at the Centre for Energy, Environmental and Technological Research (CIEMAT) in Madrid, Spain. The lab is built in two portable standardized containers. One container is used as a test room with air pipes, water pipes, valves, flowmeters, sensors, particle counter, camera, and extractor installed (Figure 6.8 (a)). Spray is generated and measured in this room. While in the other container, compressors, air tank, water tank, water pressure booster, and manometers are installed to provide the desired working conditions for experiments (Figure 6.8 (b)).



Figure 6.8 (a) Image inside the main test room for atomization experiments; (b) auxiliary equipment for supporting fog dynamic experiments in the second container

In the main room for testing, temperature can be controlled with the water circuit of the heating/cooling system embedded into the walls, floor and ceiling. Internal surfaces of the lab are covered with sheets of stainless steel in order to protect the chamber against corrosive attacks and facilitate maintenance of the room. This stainless steel has a pattern on its appearance to provide a rough surface so that operators can work inside safely even if the floor is wet. Waterproof illuminating facilities are installed. At the bottom of the test room, a waste collecting pool is built to prevent pollution. A ventilation and filtering system is built with the capability to extract and filter $200 \text{ m}^3/\text{h}$ of air out from the testing chamber. All the installed components can be categorized into 3 groups according to their main functions, which are:

Components for water/air supply:

- Compressor and small air tank for pneumatic valves: The small compressor and air tank provide sufficient pressure for pneumatic valves.
- Main compressor for supplying air for experiments: The main compressor works at maximum working pressure of 30 bar with an air flow rate of 2.5 l/s. This compressor provides required air and water pressures in the experiments.
- Air tank: This air tank is for storing air and pressure build-up. It has an internal volume of 500 l and a maximum working pressure of 30 bar.
- Water pressure booster: The 5 l water pressure booster is used to increase the pressure inside the water tank. It can work at pressure up to 30 bar.
- Pipes for water and air supply: Pipes used for connection between operating room and test room to secure air and water supply from source to atomizer for experiments.

Components for controlling operating conditions:

- Control panel: The control panel can be used to control the status of valves, on/off of the compressors, and the starting and stopping of experiments.
- Pressure regulator: Pressure regulators are used to adjust pressures for air and water for experiments.
- Pneumatic valves: Opening/closing of the valve determines starting/ending point of fog experiment. Status of the valve is controlled by the control panel located in the operating room.
- Manual valves: Manual valves are included in the pipeline in the tests rooms for the consideration of safety while nozzle required installation or manipulation.

Components for monitoring and measurement:

- Manometers: The pressure manometers are used to indicate the operating pressures for water and air.
- Flowmeter for water: Flowmeter collects information of water flow rate for atomization.
- PARTICLES PLUS 8306 particle counters for droplet measurement: Particle counter is used to measure sizes of droplets produced at different pressures by

the designed nozzle. It can measure droplet sizes from 0.3 – 25.0 μm with a flow rate of 2.83 l/min . The device measures droplet sizes by using the Dynamic Light Scattering (DLS) method. A laser light source in the device is shot through a polarizer and into the sample with suspending particles. The particles in the sample are hit with the light and diffract the light in all directions. The scattered light is collected by a sensor and the random changes in the intensity of light scattered are used for calculating the particle sizes.

The component selections aim to support nozzle atomization for at least 30 seconds at any combinations of pressures up to 30 *bar*.

6.2.2 Experimental Investigation

A series of experiments were conducted in the fog dynamics lab to investigate the performance of the designed nozzle. The nozzle in its original size and also in half size was manufactured. However considering the handling capacity of the fog dynamics lab, only the half size nozzle was tested inside the lab for the measurement of different nozzle performances. Different combinations of air and water pressures were applied to the nozzle to define its capabilities. Spray characteristics like water flow rates, spray angles, and droplets sized were monitored and recorded.

Based on the knowledge gained from initial tests for the functionality of the fogging system, 30 s of testing period was set for all experiments. In this case, experiments would not be long enough to exhaust the water in the pressure booster but long enough for monitored parameters to get settled. To set the desired pressures for experiments the valve for the water pressure booster must be turned off first. Then water is fed into the tank. Once the tank is full the water inlet is closed and the valve for the booster is turned on. Water pressure can be adjusted manually based on the reading on the manometer by tuning the regulator located next to the water tank. Air pressure can be adjusted directly by the regulator for air. When pressures are set, the control panel is used to activate valves to start fog dynamic experiments and also stop the experiments when 30 s of the experiment period has been reached. Results of fog dynamic experiments with different operating conditions are presented below.

Water flow rates are measured by a flowmeter installed on the pipeline. Table 6-2 lists raw data of generated water flows. At each air pressure condition, different water

pressures were used to investigate the relationship between input pressures and generated flow. All the data from the experiments is plotted in Figure 6.9. It can be noticed that, at a fixed air pressure, flow rate increases as input water pressure increases. While a decrease in flow is observed when air pressure is increased. In this case the nozzle can produce the highest flow when air pressure is 0 *bar*. In the experiments the highest flow rate obtained is 0.49 *l/s* when the nozzle is working at a water pressure of 22 *bar*.

Table 6-2 Flow rates of water generated at different combinations of operating pressures

Water Pressure (bar)	1	5	6	12	22	3	10	13
Air Pressure (bar)	0	0	0	0	0	3	3	3
Flow Rate (L/s)	0.05	0.15	0.22	0.34	0.49	0.04	0.23	0.29

Water Pressure (bar)	19	5	9	16	19	6	9	12
Air Pressure (bar)	3	6	6	6	6	10	10	10
Flow Rate (L/s)	0.41	0.01	0.20	0.30	0.34	0.001	0.07	0.12

Water Pressure (bar)	14	20	8	10	13	16	22	11
Air Pressure (bar)	10	10	13	13	13	13	13	17
Flow Rate (L/s)	0.19	0.33	0.00	0.03	0.10	0.16	0.29	0.00

Water Pressure (bar)	13	15	18					
Air Pressure (bar)	17	17	17					

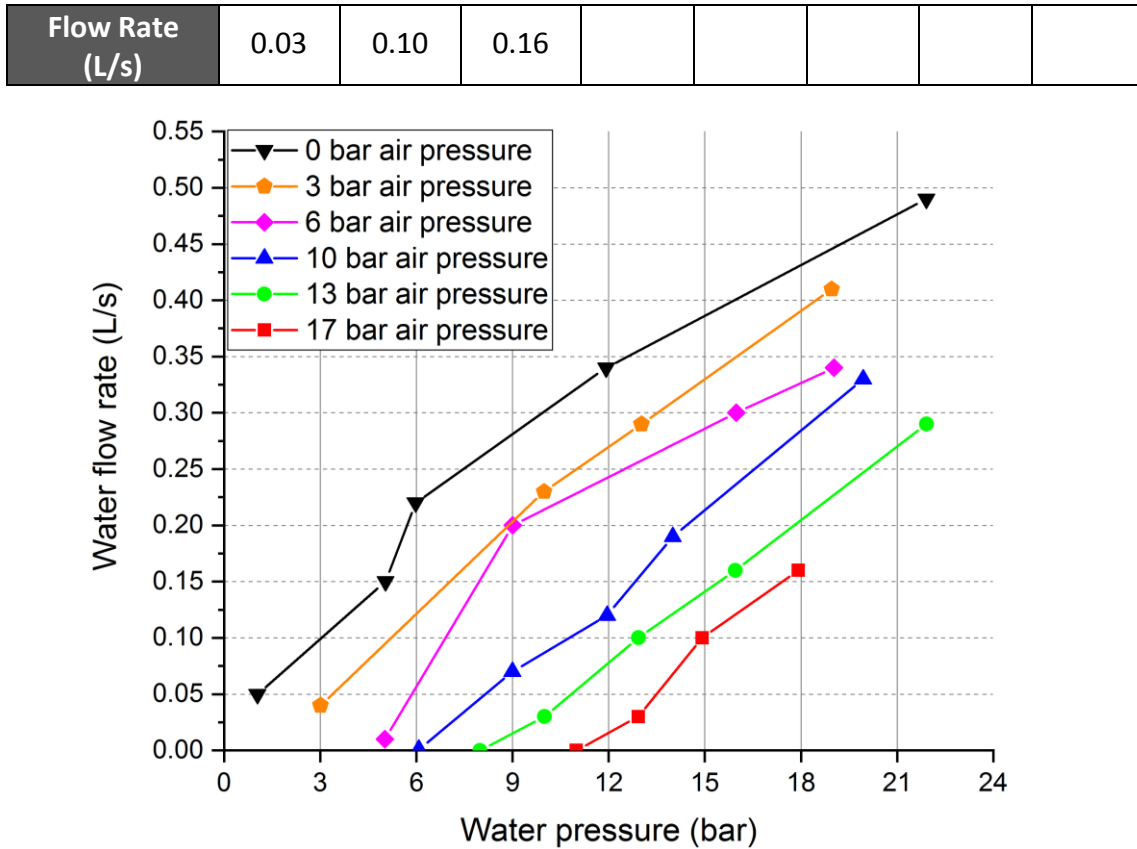
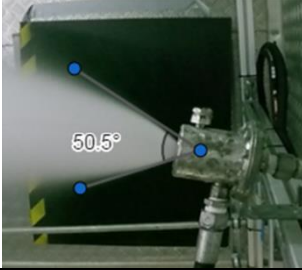
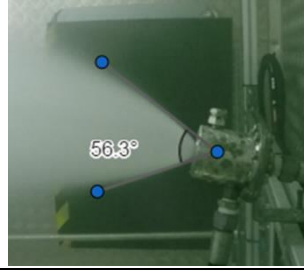
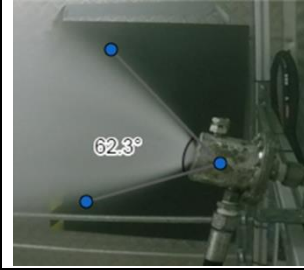


Figure 6.9 Graph showing the relationship between water pressure and water flowrate at different air pressures

Spray angles are measured manually on graphical records of spray experiments. Table 6-3 shows the graphical records for some of the experiments. Analysing these experimental results for spray angles, it can be seen that a wide range of spray angles can be achieved by this nozzle design with different combinations of operating pressures. The smallest generated spray angle is 27° at 19 *bar* air pressure and 4 *bar* water pressure. While the larger spray angle is about 89°. By analysing the results, larger spray angles can be achieved by increasing water pressure or decreasing air pressure.

Table 6-3 Graphical records for spray angles

Air pressure (bar)	5	5	10

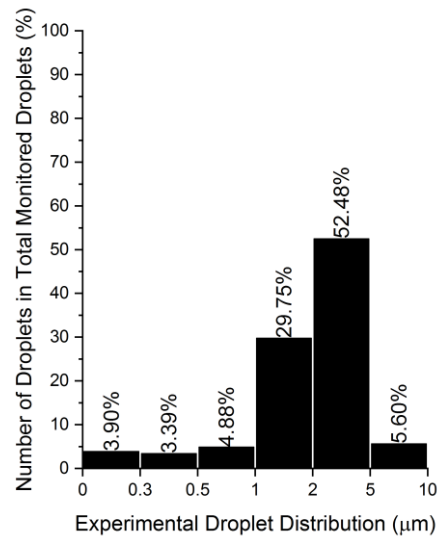
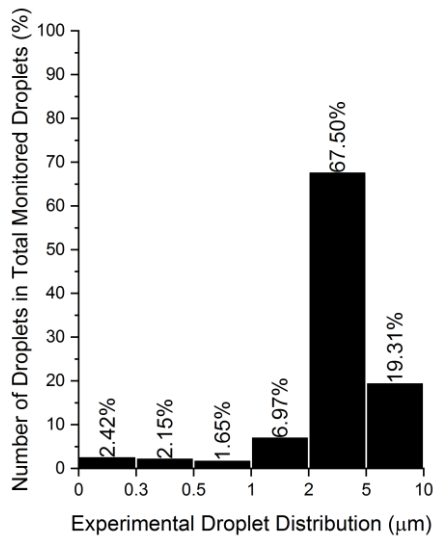
Water pressure (bar)	5	10	5
			
Air pressure (bar)	10	10	12
Water pressure (bar)	10	15	3

Droplet size distribution is recorded by a particle counter. A small amount of air is absorbed by the counter and it analyses the composition for size of droplets entrained by absorbed air. Raw data for particle distributions are presented in Appendix B. At each experiment, the counter records sampling rate, sampling duration, and number of droplets in different size ranges. Based on these data the total volume of sample air (m^3) can be obtained by multiplying the sampling rate (m^3/s) by the sampling duration (s). Then numbers of particles are normalised by dividing the values with total volumes. By summing up normalised numbers of particles in different ranges the results of particle distributions are obtained. Table 6-4 shows results of the normalised number of droplets and the proportional amount of droplets in the sampled air.

Figure 6.10 shows histograms for particle distributions based on the experimental results shown in Table 6-4. Most of the droplets produced by this nozzle fall into the range from $2 \mu m$ to $5 \mu m$. If pressures for air and water are comparable, droplets from $5 \mu m$ to $10 \mu m$ occupies the second-largest portion of the droplet range. When air pressure is much higher than water pressure, less droplets are in this range and it is noticed that most droplets have sizes between $1 \mu m$ to $5 \mu m$. Based on the results of droplet distributions, it can be concluded that the nozzle is able to produce fine droplets while the sizes of droplets are variable with different operating pressures. Smaller droplets are generated at higher air pressure.

Table 6-4 Results of particle distributions

Experimental Results							
Water Pressure (bar)	Air Pressure (bar)	Number of Droplets					
		Percentage					
		0-0.3 μm	0.3-0.5 μm	0.5-1 μm	1-2 μm	2-5 μm	5-10μm
5	6	13477.88311	11966.07355	9162.335824	38800.146	375629.4756	107487.2442
		2.42%	2.15%	1.65%	6.97%	67.50%	19.31%
3	8	19876.21105	17263.13874	24890.47898	151590.168	267414.6417	28533.71631
		3.90%	3.39%	4.88%	29.75%	52.48%	5.60%
4	10	22291.75882	19639.19847	17454.58659	68038.07456	458071.9418	59057.40342
		3.46%	3.05%	2.71%	10.56%	71.07%	9.16%
10	10	22529.02635	19826.45946	15550.58513	34183.09682	506665.805	78234.15876
		3.33%	2.93%	2.30%	5.05%	74.84%	11.56%
6	12	27422.6825	26915.58044	22707.24691	78454.1023	421653.3922	130638.0499
		3.87%	3.80%	3.21%	11.08%	59.57%	18.46%
14	14	21275.26135	19369.4403	15588.35482	69660.98505	463739.5439	74704.21609
		3.20%	2.92%	2.35%	10.49%	69.80%	11.24%



Air (bar)	6	8
Water (bar)	5	3

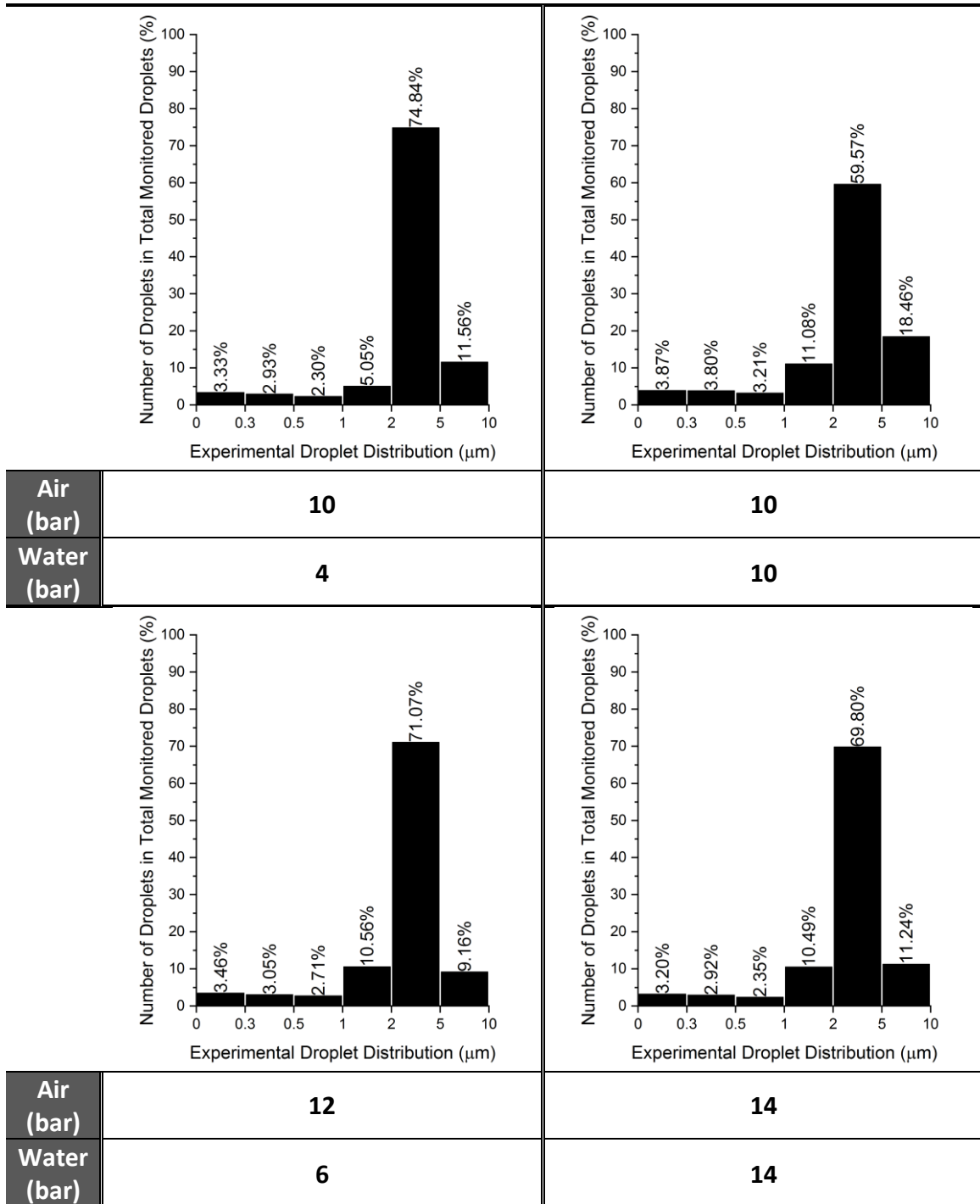


Figure 6.10 Histograms for particle distributions

6.3 CFD Model Validation and Error Analysis

In order to validate the proposed simulation system, pressure combinations used in experiments described above are used as pressure boundary settings for predicting water flow rates, spray angles, and droplet distributions. Numerical results are collected and presented as below:

Table 6-5 shows the numerical results of water flow rates generated at pressures used in the experiments. All these data are plotted together with experimental results in Figure 6.11 so that a direct comparison can be made. As it can be clearly seen, numerical results can correctly and reliably predict the trend of changes in water flow rate with different water pressures. At a fixed air pressure, water flow increases as increasing water pressure. For all cases the differences between numerical and experimental results are less than 0.09 L/s. The maximum difference happens when the nozzle is working at 19 bar water pressure and 6 bar air pressure

Table 6-5 Flow rate predicted by proposed simulation system

Water Pressure (bar)	1	5	6	12	22	3	10	13
Air Pressure (bar)	0	0	0	0	0	3	3	3
Flow Rate (L/s)	0.05	0.10	0.16	0.30	0.53	0.05	0.31	0.32

Water Pressure (bar)	19	5	9	16	19	6	9	12
Air Pressure (bar)	3	6	6	6	6	10	10	10
Flow Rate (L/s)	0.48	0.02	0.21	0.38	0.43	0.00	0.06	0.18

Water Pressure (bar)	14	20	8	10	13	16	22	11
Air Pressure (bar)	10	10	13	13	13	13	13	17
Flow Rate (L/s)	0.21	0.38	0.00	0.02	0.11	0.22	0.36	0

Water Pressure (bar)	13	15	18					
Air Pressure (bar)	17	17	17					
Flow Rate (L/s)	0.02	0.08	0.17					

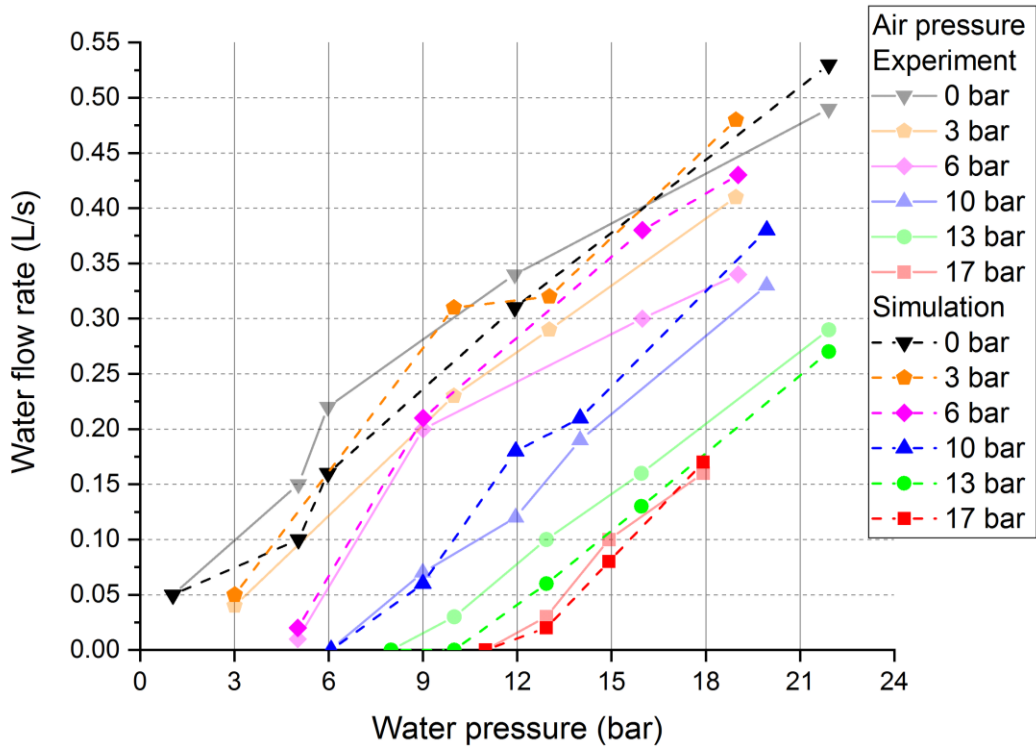
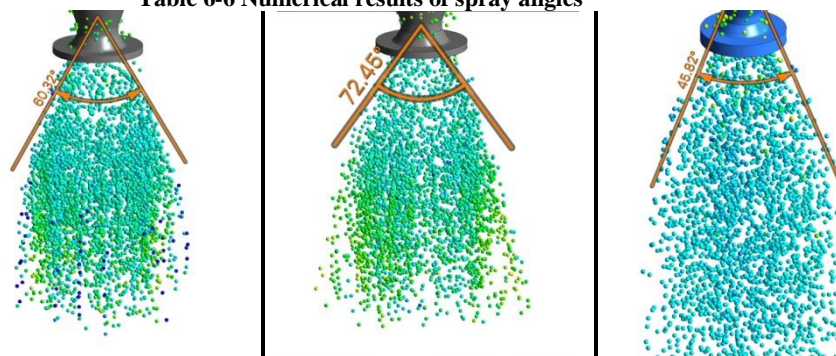


Figure 6.11 Direct comparison between experimental and numerical results of water flowrates

Table 6-6 shows angles of sprays generated at different combinations of pressures. The numerical results match well with the spray angles observed in experiments. The maximum difference between numerical and experimental results is 6.4°. This shows the reliability of the CFD system for modelling droplet dynamics in the spray. The experimental and numerical results for spray angles at different operating conditions are plot in Figure 6.12 for model validation.

Table 6-6 Numerical results of spray angles



Air pressure (bar)	5	5	10
Water pressure (bar)	5	10	5

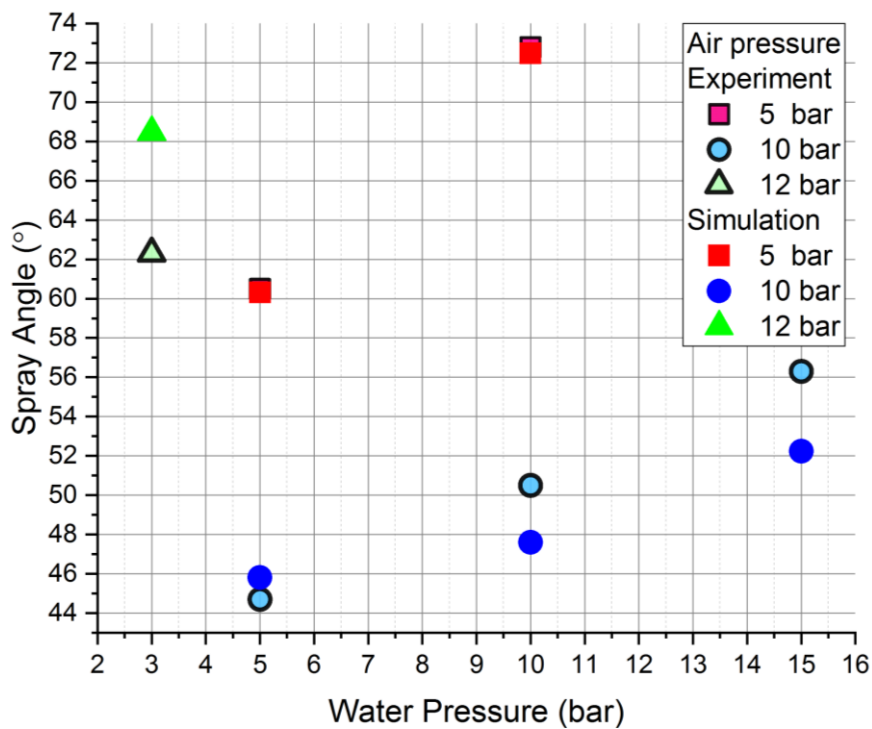
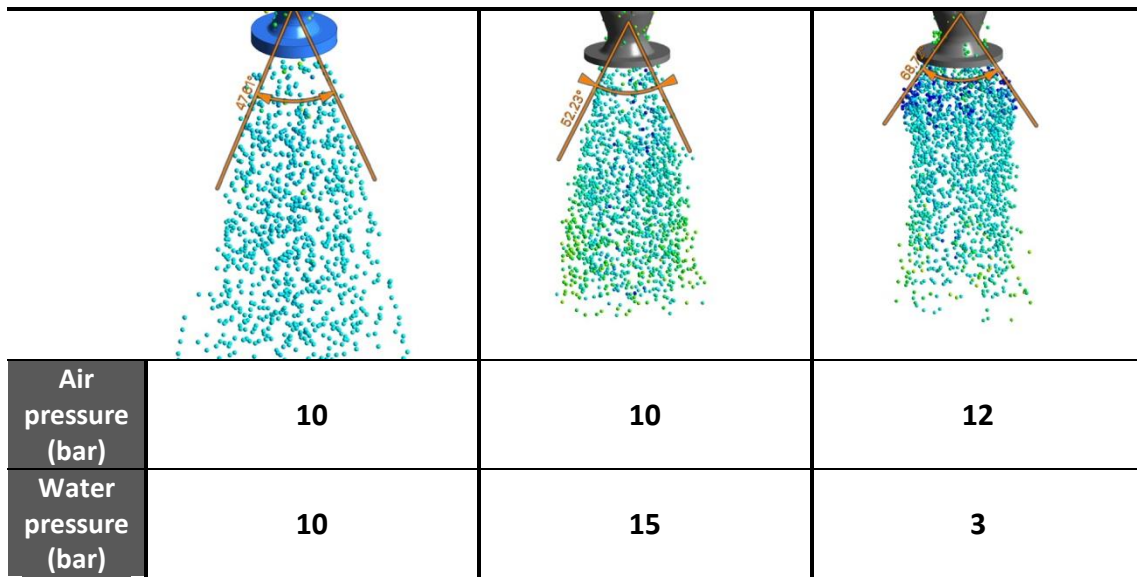


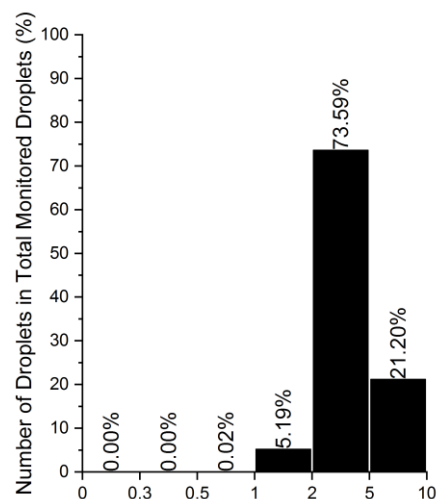
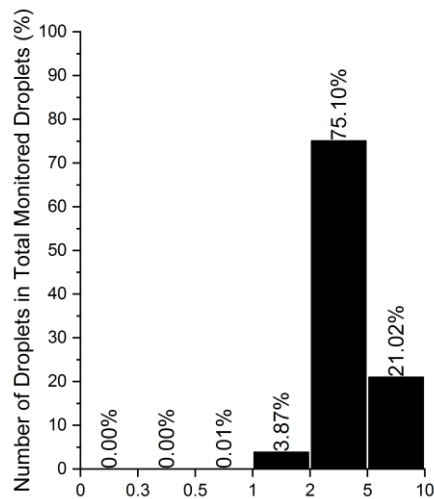
Figure 6.12 Direct comparison between experimental and numerical results of spray angles

Table 6-7 lists collected data for droplet diameter at the outlet of the calculation domain. Ranges of droplet sizes are defined as they were used in experiments. Pressure boundary conditions are selected as they were used for generated sprays. Good agreement has also been found between the numerical results and experimental results on generated sizes of droplets (Figure 6.13). As it is observed in both experiments and simulations, most droplets in experiments fall into the range from 2 μm to 5 μm. This indicates the outstanding performance of this nozzle for

producing fine droplets. When the air pressure is much higher than water pressure, an increased proportion of droplets in the range from 1 μm to 2 μm has been observed, this is also consistent with the experimental results.

Table 6-7 Numerical results of droplet distribution

Numerical Results							
Water Pressure (bar)	Air Pressure (bar)	Number of Droplets					
		Percentage					
		0-0.3 μm	0.3-0.5 μm	0.5-1 μm	1-2 μm	2-5 μm	5-10 μm
5	6	0	0	8	2130	41336	11567
		0%	0%	0.01%	3.87%	75.10%	21.02%
3	8	0	3	17	4377	66186	83991
		0%	0%	0.02%	5.19%	73.59%	21.20%
4	10	0	0	125	5514	66057	90606
		0%	0%	0.0756%	3.68%	57.76%	38.48%
10	10	0	0	40	1988	32550	52910
		0%	0%	0.08%	3.68%	57.76%	38.48%
6	12	1	6	173	10568	129421	3420
		0%	0%	0.12%	7.36%	90.1%	2.38%
14	14	0	9	209	3772	42268	59799
		0%	0.02%	0.33%	5.96%	64.38%	29.32%



Air (bar)	6	8
Water (bar)	5	3

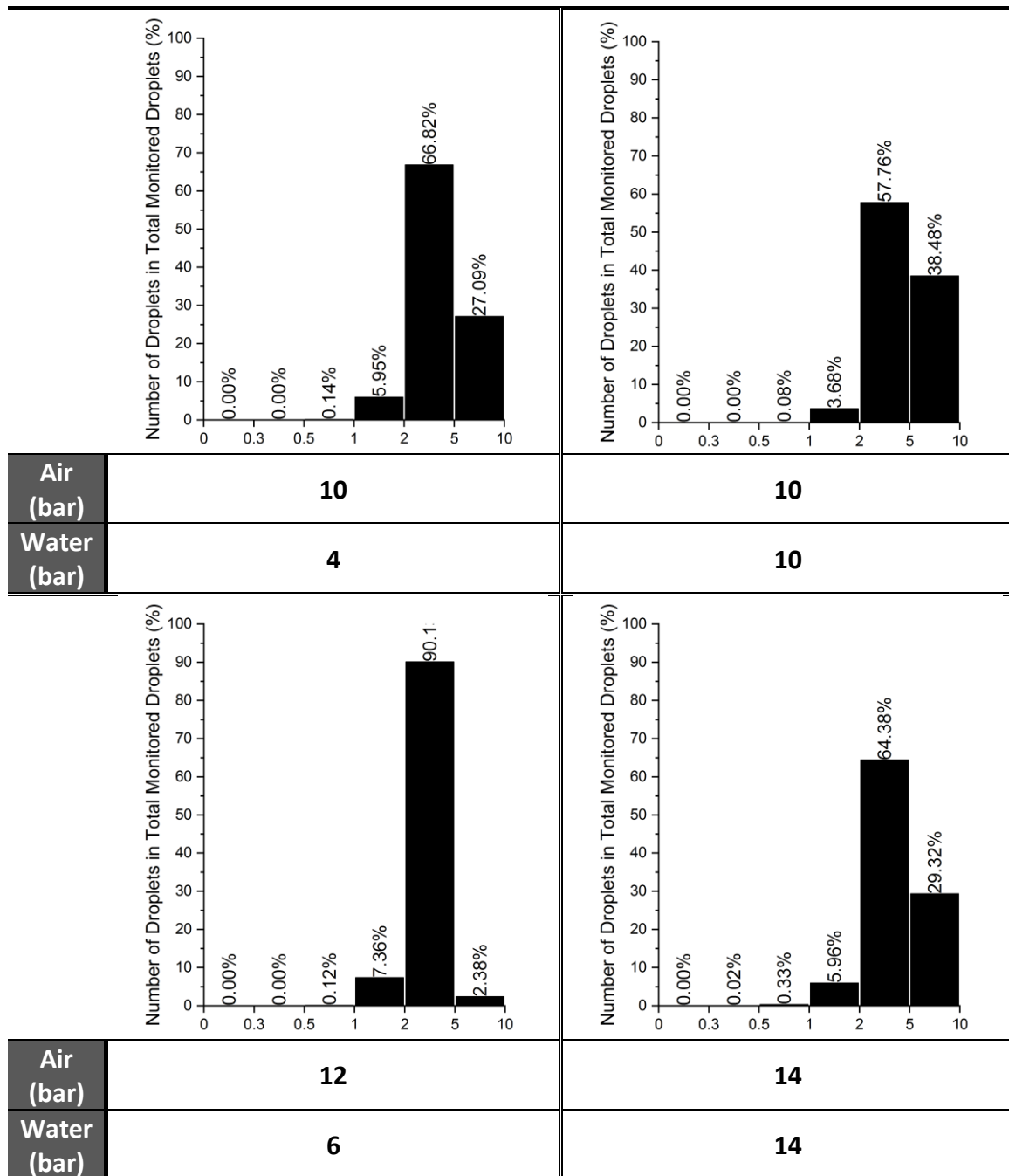


Figure 6.13 Histogram for numerical results of droplet distributions

Although in general the CFD calculating system is performing well in predicting the flow rate, spray angle, and droplet size produced at different operating conditions, errors still exist in numerical results. By analysing the differences between the calculated and the experimental results the causes of error can be proposed as follows:

- Process complexity.** As the multiphase atomization involving internal nozzle flow and external droplet deposition is affected by several complicated fluid dynamic processes such as turbulent flow, multi-phase interaction, flow oscillation, and phase change, it is still not possible to solve the problem

directly. To enable an engineering calculation it is necessary to adopt hypotheses and variable averaging into the model which at the same time introduces numerical errors.

- **Time dependence.** Atomization is a highly time dependent process that is constantly changing. Oscillation generated at inlets by compressors, small changes in fluid properties, or even a change in the ambient environment may introduce change in the characteristics of sprays. In addition, by observing the numerical results of flow rates, it is noticed that most of the results are higher than the flows actually produced by experiments. In experiments when the monitored parameter gets stable parts of the compressed air and water have been consumed and the operating pressures are not as high as they were set. While in simulations ideal boundary conditions with constant values are used.

Although numerical error exists in the numerical process, by comparing the numerical results with experiments enough accuracy has been achieved by this CFD system for predicting flow rate, spray angle, and droplet size. What is more, the excellent performance of this model for predicting spray characteristics generated by the nozzle working at different operating pressures has shown its capability for virtual testing. This reduces the development cycle and cost for new product design and provides guidelines for achieving optimum performance.

6.4 Summary

In this chapter in order to verify the study conducted and presented in the previous chapter:

- Detail designs of the modular nozzle design regarding fabrication and assembly have been presented. Some of the nozzle components have been redesigned after the first trial of fabrication.
- Setup of the fog dynamic lab has been described. The lab is able to support continuous nozzle atomization for at least 30 s at any combination of pressure up to 30 bar. It can also record data on flow rate, spray angle and droplet size.
- Experimental results have been presented regarding flow rate, spray angle and droplet distribution. These data show the capability of this nozzle to generate spray with small droplets and relatively high flow rates.

- Model validation for the proposed CFD calculating system has been finished by comparing the experimental and numerical results. It is validated that the CFD calculating method can correctly predict the flow of spray, its angle and droplet distribution. Only a small error has been found between simulation and experiment. This can be due to process complexity and time dependence of the atomization process.

Chapter 7

Design Optimization and Virtual Testing

By the results from fog dynamic experiments, it is proved that the nozzle design is able to produce spray with a fine droplet size. However, the flow rate is still not high enough. With the numerical results from the validated CFD modelling system, a requirement-driven design optimization is conducted. This chapter presents details and results of the optimization process which includes:

- **Structural analysis** studying flow conditions inside the enclosed nozzle body with the help of the validated CFD modelling system.
- **Requirement-driven design optimization** intending to improve performance of the nozzle based on the results from functional analysis. A feature is modified if it shows benefits for improving the desired nozzle performance;
- **Virtual testing** which tests the performance of the optimized nozzle design virtually with the validated CFD modelling system.

7.1 Nozzle Design Optimization

Based on the results obtained from experiments and CFD simulations, the nozzle design is capable of generating sprays with a small droplet size under 10 microns and with a water flow rate from 0.01 kg/s to 0.49 kg/s. Targeting a small droplet size and high water-flow-rate the nozzle design is achieving well on generating spray with

small drops however there is still a gap to generate a high flow rate. Thus the focus for design optimization is on redesigning the nozzle for a much higher mass flow rate while maintaining the small droplet size.

The architecture of the original full-size nozzle is used as the basic model for design optimization. A structural analysis has been carried out to identify the function of different parts of the nozzle structure.

Figure 7.1 shows that, in the modular nozzle design, the air inlet, first mixing chamber, water solution inlet and particle inlet are mainly used for feeding the fluid into the second mixing chamber. Although initial atomization happens at the end of the water solution inlet channel, only very large droplets are generated in this area. The most severe droplet breakup happens when the liquid flow together with large droplets encounter the air stream at the second mixing chamber and become fully mixed with it. The droplets will then flow along with the air out of the nozzle through the orifice which can further breakdown the drops. This structural analysis is also confirmed by the numerical results from parametric simulations in Section 5.6. Dimensions of features close to the nozzle orifice affect sizes of generated droplets the most while there is no clear relationship between the dimensions of the 2nd chamber and droplet sizes.

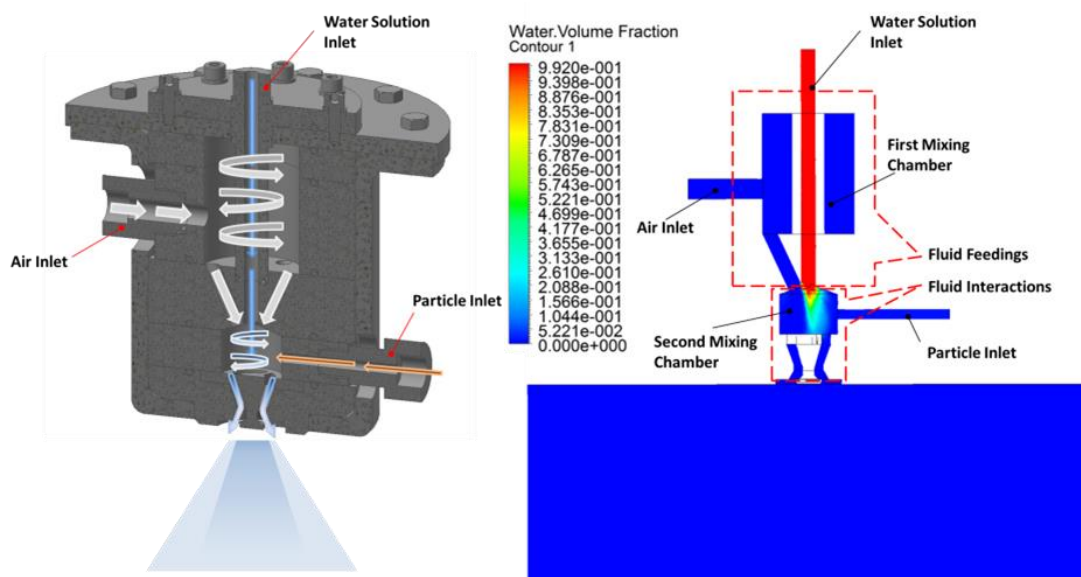


Figure 7.1 Structural Analysis of the Original Nozzle

According to the structural analysis above, the nozzle parts are separated into two groups according to their main functions. The water solution inlet, air inlet, first

mixing chamber and particle inlet are mainly used for feeding different fluids. Tasks of fully mixing different fluids and atomizing the liquid lie in the nozzle orifice. In this nozzle optimization process, the primary aim is to adjust the existing design so that the generated spray can have a similar droplet size but much higher flowrate. The structures for mixing different fluids and breaking water into small droplets are kept the same as much as possible and the cross-sectional area for feeding is increased by adding more feeding channels. Figure 7.2 presents the water and air feeding channels in the optimized nozzle.

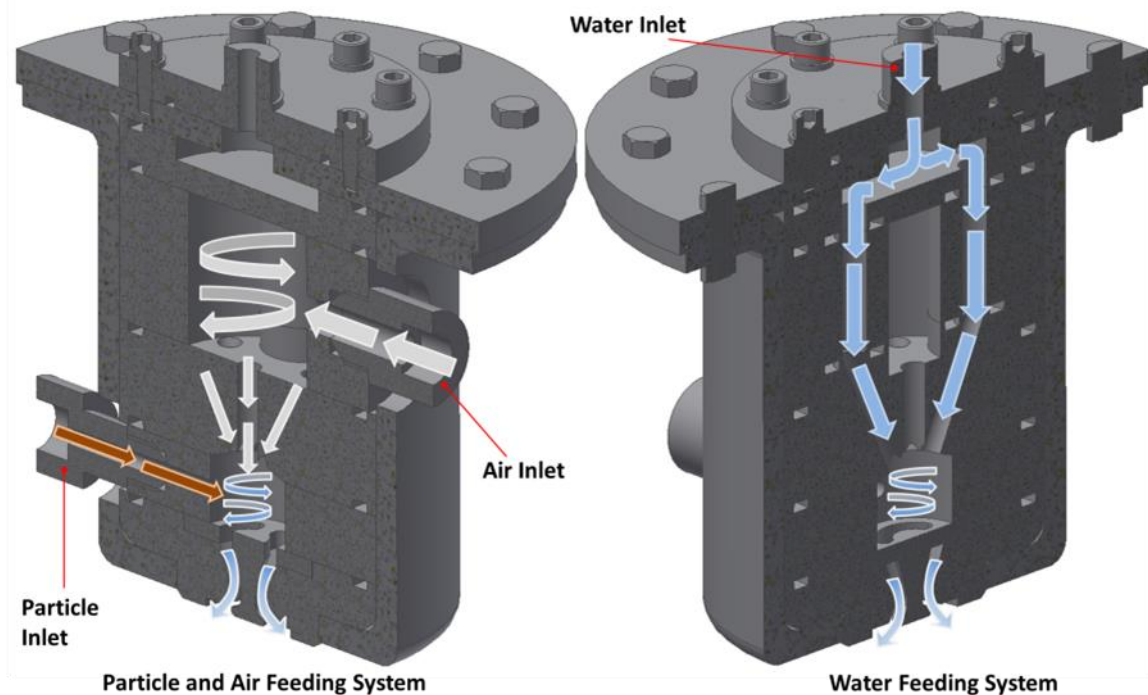


Figure 7.2 Internal structure of the optimized nozzle design

Similar to the original nozzle design, liquid, compressed air, and particles are fed into the nozzle through three separate inlets. Compressed air entering the nozzle through the air inlet firstly reaches a chamber. Then the air stream is separated into 5 and enters the mixing chamber through channels of designated angles. Supplied water is diverged into 2 branches after it passes through the inlet. After that the 2 water flows are fed into the mixing chamber. Entrained by a carrier fluid, solid particles are fed into the mixing chamber directly through the particle inlet. Compressed air, water, and particles inside the same chamber interact and mix with each other. Then the strong air flow carries all the liquid drops and particles out of the nozzle from the orifice.

Figure 7.3 shows the redesign of the swirl insert. This is a very important part in the nozzle since it connects the feeding system and the mixing system in the nozzle. In order to imitate the flowing situation in the original nozzle as much as possible, each of the water channels leading to the second mixing chamber is surrounded by 3 air channels. The performance of the redesigned nozzle is virtually tested by using the validated CFD simulation.

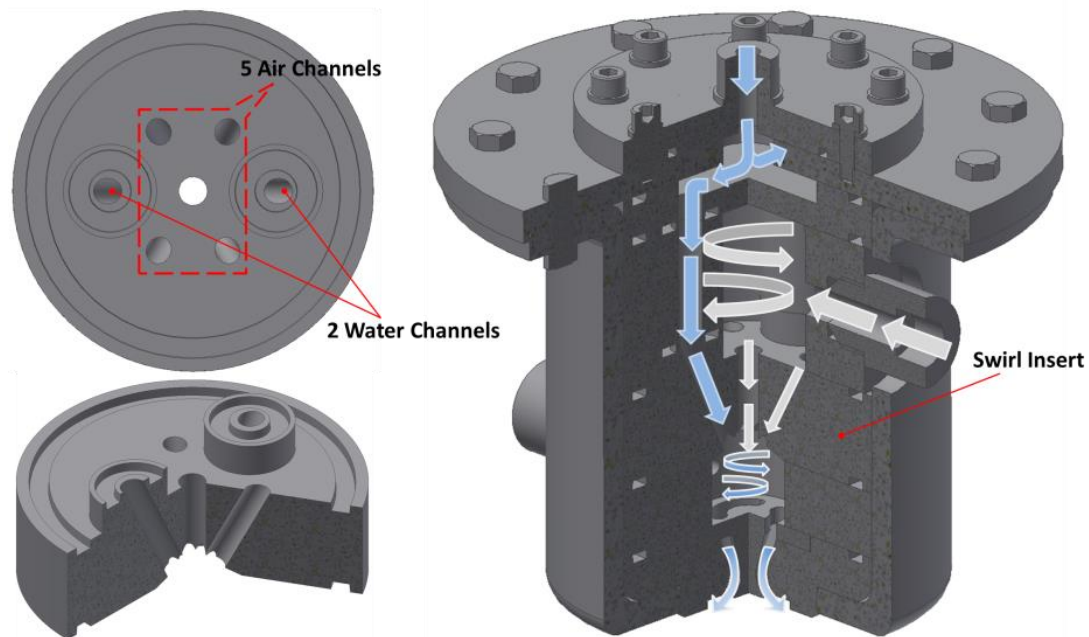


Figure 7.3 Redesign of the swirl insert

7.2 Virtual Testing of Optimized Nozzle Design

Figure 7.4 presents the numerical results of this optimized nozzle for a higher rate of flow. It can be seen from Figure 7.4 (a) that water entering from water inlet is firstly separated into two as designed and fed into the mixing chamber. Air, on the other hand, flows into the first chamber and is then separated into 5 streams by the newly designed swirl insert. Interaction and mixing happens between the two phases in the mixing chamber before they flow out from the nozzle orifice and produce a full-cone spray. Figure 7.4 (b) highlights the droplets in the spray and their sizes. Judging from the colour, nearly all the droplets in the spray are smaller than $35\ \mu\text{m}$. Figure 7.4 (c) shows the distributions of droplets and mean droplet size. The droplet number in a cell is greater close to the outer edge of the spray. It is diluted when the spray travels downstream. No big change of mean droplet size is observed. Droplet collisions and coalescence are revealed at the edge of the spray, which causes an increment in droplet diameter. Figure 7.4 (d) clearly shows the proportion of droplets with different

diameters reaching the outlet of the calculation domain. 99% of droplets have diameters less than 30 μm .

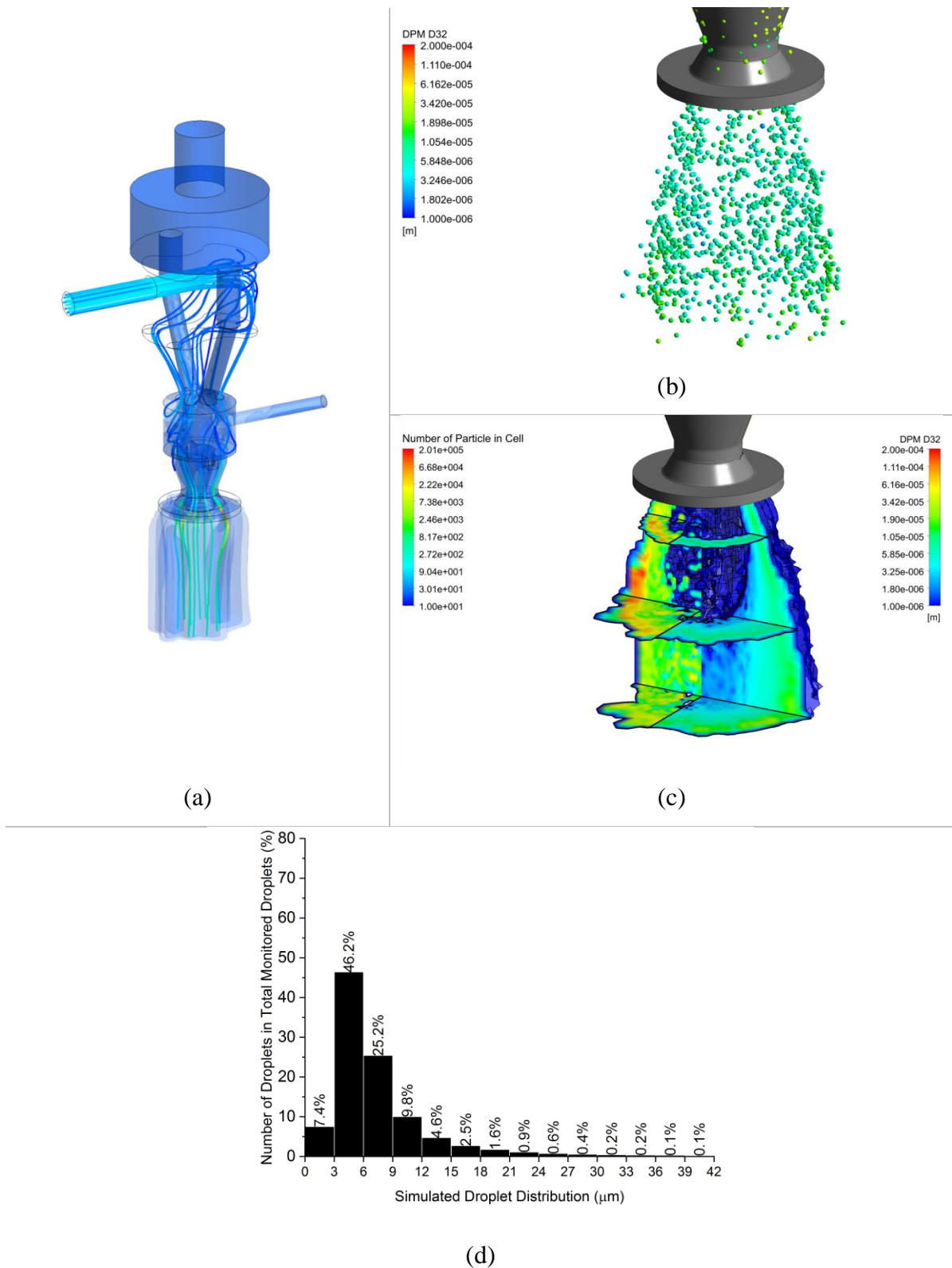


Figure 7.4 Numerical results of optimized nozzle: (a) volumetric distribution of water and streamlines of air velocity; (b) tracking of water droplets and their SMD values; (c) spatial distribution of water droplet number and mean droplet size; (d) histogram presenting diameter of droplets exiting the outlet of calculation domains

Table 7-1 shows the parameters of the spray produced by the optimized nozzle design. This nozzle is able to generate spray with a water flow rate of 1.47 kg/s which is nearly double the flow rate produced by the original nozzle. The produced spray has a full-cone pattern. Sizes of the produced droplets range from 1.1 μm to 69 μm and the SMD value at the outlet of the calculation domain is 16.7 μm. Sizes of droplets are inevitably affected by the dramatically increased flow rate. However, from the histogram presented in Figure 7.4 (d), a large number of produced droplets are smaller than 9 μm. Additionally, by adjusting the air inlet pressure to let more air mix with the water, the optimized nozzle should be able to produce high flow rates with finer droplet size.

Table 7-1 Statistics information of spray generated by optimized nozzle design

	Water Flow Rate (kg/s)	Cone Pattern	Drop Size Range (μm)	Sauter Mean Diameter (μm)
Original Design	0.845	Full cone, wide angle	1.2 – 29.4	8.1
Optimized Design	1.47 <i>(172.13%)</i>		1.1 – 69	16.7 <i>(206.17%)</i>

Figure 7.5 plots the performance of the optimized nozzle in the figure for nozzle flow rate and droplet size. It can be directly seen from the figure that the optimized nozzle design can achieve fine droplets and high rate of flow at the same time, which cannot be produced by other nozzle designs.

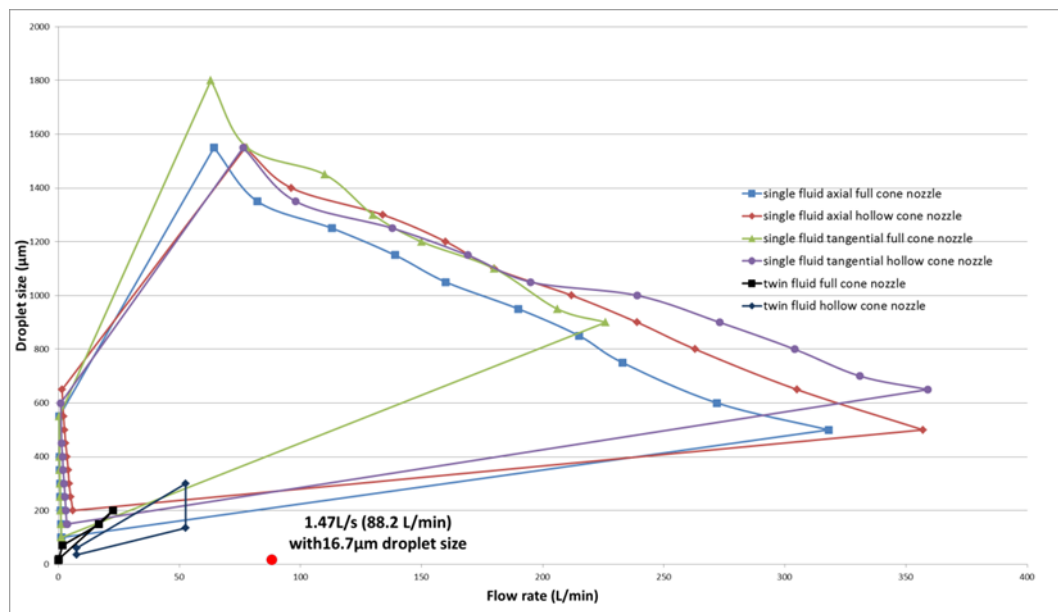


Figure 7.5 Performance of optimized nozzle in the map of flow rate vs droplet size

7.3 Summary

This chapter focuses on nozzle design optimization for higher flow rate. In order to achieve the goal for improving nozzle design:

- Functional analysis has been conducted based on numerical results to identify the function of different parts of the nozzle structure. In this nozzle design, it has been shown that the air inlet, first mixing chamber, water solution inlet and particle inlet are mainly used for feeding the fluid into the second mixing chamber. The second mixing chamber and nozzle orifice are mainly responsible for breaking up droplets;
- Design features that are beneficial for improving the desired nozzle performance have been modified. The structures for mixing different fluids and breaking water into small droplets are kept the same as much as possible and the cross-sectional area for feeding is increased by adding more feeding channels.
- Virtual testing on nozzle performance has been conducted based on the proposed CFD modelling system. The optimized nozzle is able to generate spray with a water flow rate of 1.47 l/s which is nearly double the flow rate produced by the original nozzle. The droplet size is slightly affected with an averaged value of 16.7 μm .

Chapter 8

Conclusions and Future Work

8.1 Conclusions

The primary goal of this study was to overcome challenges in advanced nozzle design for achieving small droplet size and high rate of fluid flow. Step-by-step design optimization has been performed with the aid of numerical simulation based on a newly developed CFD modelling system. This calculation system can study the whole spraying process from internal nozzle flow to external droplet distribution. In order to realize the final goal of this study the following objectives have been met:

1. CFD modelling methods for multiphase atomization especially on theories and drawbacks for turbulence, multiphase flow, and droplet dynamics have been studied in detail. Suitable models have been selected for studying internal nozzle flow and external droplet dynamics. Self-developed User-Defined-Functions and schemes have been integrated into the calculation process for building communications and transferring data between the two models. Establishment of a CFD modelling system for studying far-field spray dynamics affected by internal nozzle flow and initial breakup has been achieved.

2. Based on investigations conducted during the literature review, 6 nozzle concepts featuring different configurations have been generated. Concept evaluation and justification have been accomplished based on CFD simulations. One selected nozzle design among these 6 concepts has been further optimized with the help of combined CFD modelling with parametric simulation. More than 20 simulations have been done before the final functional details for the nozzle design are decided.
3. After the functional design of the nozzle was decided, detailed nozzle components design started, which considered sealing, connection between components and design for manufacture. Then parts for the nozzle design were manufactured and assembled. Fog dynamic experiments have been conducted to study the performance of the nozzle. The nozzle is able to produce flows up to 0.49 l/s. Spray angle can change from 44.7° to 72.8° depending on operating pressure. For all the experiments, most of the produced droplets are in the range from 2 μm to 5 μm .
4. A series of numerical simulations have been conducted and results have been compared to fog dynamic experiments. It has been shown that the proposed CFD modelling system is capable of giving reliable predictions on water flow rate, spray angles, and droplet sizes. Only small errors have been observed in the numerical results, which may be due to the nature of process complexity and time dependence of atomization.
5. Structural analysis has been carried out for further optimizing the design towards a higher produced flow rate. Parts such as the air inlet, first mixing chamber, water solution inlet and particle inlet are recognized as mainly used for feeding the fluid while the second mixing chamber and nozzle orifice are mainly responsible for breaking up droplets. The cross-sectional area of the structure for feeding fluid is increased by adding more feeding channels. Virtual testing has been done for studying the performance of the optimized nozzle. It has been predicted that the nozzle is able to generate spray with a water flow rate of 1.47 l/s with an averaged value of 16.7 μm .

By achieving these objectives, the final goal of this project for designing an advanced nozzle which can overcome challenges for producing spray with high flow rates and small droplet sizes has been accomplished. The optimized nozzle design is able to

generate spray with 1.47 l/s flow rate and 16.7 μm averaged droplet size which can hardly be achieved by any other nozzles. Concurrently a CFD modelling system has been developed for simulating the whole atomization process from internal nozzle flow to external droplet distribution. It has been validated by comparing the numerical results of flow rate, spray angle, and droplet size to experiments. Good agreement can be found between numerical and experimental results indicating the reliability of the proposed CFD modelling system for simulating the atomization process.

8.2 Summary of Contributions to Knowledge

8.2.1 CFD Models for Multiphase Atomization

One of the contributions to knowledge from this study is the establishment and validation of a new CFD modelling system which can simulate the whole atomization process from internal nozzle flow to the external spray region. The volume fraction of water changes dramatically from 100 % at water inlet to less than 1 % at the far-field spray region. Traditional multi-phase simulations are mainly based on a Eulerian-Eulerian framework which requires the dispersed-phase volume fraction to be more than 10 %, or a Eulerian-Lagrangian framework for dispersed-phase volume fractions less than 10 %. Neither of the methods are capable of simulating the whole atomization process and this remains an academic problem. In this study, a CFD modelling system has been established with a self-developed module for automated data analysis and transfer. This data handling module intends to build communications between the two models and to bridge the knowledge gap between separated flow theories in order to establish a practical systematic simulation for engineering calculations. Model validation has been done by comparing numerical results with experiments. It has been proved that the model is feasible for predicting nozzle performance.

Apart from the model itself, with the help of reliable CFD modelling, virtual testing can be achieved which significantly reduces the cycle time and cost for nozzle development. It also provides useful guidelines for selecting optimum operating conditions for desired nozzle performance.

8.2.2 Nozzle Design and Design Approach

Based on the design review which investigated a large amount of data relating to nozzle performance, there is no existing nozzle design that can produce spray with a high flow rate and small droplet size. This type of nozzle has great potential for wide application in firefighting, pest management, and pollution control. It has always been a challenge for atomizer designers to develop such a nozzle since the characteristics of the spray are largely affected by internal nozzle flow which happens inside the enclosed nozzle body. Non-intrusive measurement of internal flow conditions is extremely difficult which makes it hard to optimize the internal flow path for better nozzle performance. In this study, with the aid of a newly developed CFD modelling system, nozzle performance can be predicted and at the same time internal nozzle flow can be easily analysed, which aids the development of advanced nozzle design. At the end of the study a completely new nozzle design has been achieved which is virtually tested. Its high performance on flow rate and droplet size has never been reported as being achieved through any other nozzle designs.

This study also investigated a new approach for nozzle design, which starts from design review, concept generation and evaluation, computer-aided design optimization, fog dynamic testing until the development of the optimized nozzle. Conventionally, nozzles are developed using the empirical formula and experiment method. Large amount of experiments are required for establishing correlations between design parameters and nozzle performances. This method is usually time consuming and high-cost. The new approach uses the validated CFD model. Together with parametric modelling, the approach is able to evaluate large amount of nozzle designs automatically, which reduces the development cycle and costs. The achievement in this study for developing a new fogging nozzle design supports the new CFD-aided design approach for nozzle.

8.3 Future Work

8.3.1 To Improve the Optimization Approach

In this study a single parameter optimization process has been adopted. One design parameter was changed at a time to study its effect on the performance of the nozzle. However, this optimization process is rather time-consuming. For highly efficient

design optimization and development a systematic optimization approach such as the Monte Carlo method could be applied.

8.3.2 To Optimize the Third Component Mixing Concept

The third component mixing concept has been developed and tested in the advanced nozzle design. However in experiments the dose for the third component cannot be accurately controlled by varying input pressure. Further design optimization is required for third component mixing so that the required amount of third-phase particles can be distributed.

8.3.3 To Reduce the Nozzle Components

For the purpose of research, the advanced nozzle design adopted a modular architecture which enabled part, material, or design replacement. However, this also made the nozzle relatively large with too many components. After the design of nozzle is fixed, a structural optimization can be done to reduce the number of parts for nozzle.

References

- [1] X. Jiang, G. a. Siamas, K. Jagus, and T. G. Karayiannis, "Physical modelling and advanced simulations of gas–liquid two-phase jet flows in atomization and sprays," *Prog. Energy Combust. Sci.*, vol. 36, no. 2, pp. 131–167, Apr. 2010.
- [2] J. Ishimoto, H. Hoshina, T. Tsuchiyama, H. Watanabe, A. Haga, and F. Sato, "Integrated Simulation of the Atomization Process of a Liquid Jet Through a Cylindrical Nozzle," *Interdiscip. Inf. Sci.*, vol. 13, no. 1, pp. 7–16, 2007.
- [3] B. G. M. van Wachem and A. E. Almstedt, "Methods for multiphase computational fluid dynamics," *Chem. Eng. J.*, vol. 96, no. 1–3, pp. 81–98, 2003.
- [4] Inc. ANSYS, "ANSYS FLUENT theory guide V14.5," 2012.
- [5] Inc. ANSYS, "ANSYS Fluent 12.0 user's guide," 2009.
- [6] J. Zhao and L. Yang, "Simulation and Experimental Study on the Atomization Character of the Pressure-Swirl Nozzle," vol. 2012, no. December, pp. 271–277, 2012.
- [7] D. I. Kolaitis and M. A. Founti, "A comparative study of numerical models for Eulerian-Lagrangian simulations of turbulent evaporating sprays," *Int. J. Heat Fluid Flow*, vol. 27, no. 3, pp. 424–435, 2006.
- [8] J. V. Farman, "Sprays," *Anaesthesia*, vol. 22, no. 4, pp. 703–704, 1967.
- [9] G. G. Nasr, A. J. Yule, and L. Bendig, *Industrial Sprays and Atomization*, vol. 33. Springer London, 2013.

- [10] S. Terminology and S. Terminology, "Relating to Liquid Particles and Atomization 1," *Annu. B. ASTM Stand.*, vol. i, no. Reapproved, pp. 1–7, 2004.
- [11] N. Ashgriz, *Handbook of atomization and sprays: theory and applications*. 2011.
- [12] Spraying system CO., *Technical Reference Spray Performance Considerations Technical Reference*. .
- [13] E. D. Hirleman, W. D. Bachalo, and P. G. Felton, *Liquid Particle Size Measurement Techniques*, no. v. 2. ASTM, 2008.
- [14] H.-E. Albrecht, M. Borys, N. Damaschke, and C. Tropea, *Laser Doppler and Phase Doppler Measurement Techniques*. Springer Berlin Heidelberg, 2013.
- [15] A. Lefebvre, *Atomization and Sprays*. Hemisphere Publishing Corporation, 2018.
- [16] A. Rashkovan, V. Kholmer, and E. Sher, "Effervescent Atomization of Gasoline Containing Dissolved Co₂," *At. Sprays*, vol. 14, no. 4, pp. 341–354, 2004.
- [17] S. D. Sovani, P. E. Sojka, and A. H. Lefebvre, "Effervescent atomization," *Prog. Energy Combust. Sci.*, vol. 27, no. 4, pp. 483–521, 2001.
- [18] Z. Chen, Z. He, W. Shang, L. Duan, H. Zhou, G. Guo, and W. Guan, "Experimental study on the effect of nozzle geometry on string cavitation in real-size optical diesel nozzles and spray characteristics," *Fuel*, vol. 232, no. June, pp. 562–571, 2018.
- [19] N. Hampel, E. Roydeva, A. Bück, and E. Tsotsas, "Coating of finely dispersed particles by two-fluid nozzle," *Particuology*, vol. 38, pp. 80–93, 2018.
- [20] J. Chen, Y. Li, W. Chen, X. Luo, Y. Chen, Z. Yang, and I. W. Eames, "Investigation of the ejector nozzle in refrigeration system," *Energy*, vol. 157, pp. 571–587, 2018.
- [21] Y. Zhang, B. Zhu, G. Wittstock, D. Li, Y. Liu, and X. Zhang, "Generating ultra-small droplets based on a double-orifice technique," *Sensors Actuators, B*

- Chem.*, vol. 255, pp. 2011–2017, 2018.
- [22] M. Zaremba, J. Kozák, M. Malý, L. Weiß, P. Rudolf, J. Jedelský, and M. Jícha, “An experimental analysis of the spraying processes in improved design of effervescent atomizer,” *Int. J. Multiph. Flow*, vol. 103, pp. 1–15, 2018.
- [23] P. X. Pham, A. Kourmatzis, and A. R. Masri, “Local characteristics of fragments in atomizing sprays,” *Exp. Therm. Fluid Sci.*, vol. 95, no. January, pp. 44–51, 2018.
- [24] B. Pizziol, M. Costa, M. O. Panão, and A. Silva, “Multiple impinging jet air-assisted atomization,” *Exp. Therm. Fluid Sci.*, vol. 96, no. March, pp. 303–310, 2018.
- [25] L. Lešnik, B. Kegl, G. Bombek, M. Hočevár, and I. Biluš, “The influence of in-nozzle cavitation on flow characteristics and spray break-up,” *Fuel*, vol. 222, no. February, pp. 550–560, 2018.
- [26] W. Zhao, F. Cao, Z. Ning, G. Zhang, Z. Li, and J. Sun, “A computational fluid dynamics (CFD) investigation of the flow field and the primary atomization of the close coupled atomizer,” *Comput. Chem. Eng.*, vol. 40, pp. 58–66, 2012.
- [27] A. Pandal, R. Payri, J. M. García-Oliver, and J. M. Pastor, “Optimization of spray break-up CFD simulations by combining Σ -Y Eulerian atomization model with a response surface methodology under diesel engine-like conditions (ECN Spray A),” *Comput. Fluids*, vol. 156, pp. 9–20, 2017.
- [28] A. Kashani, H. Parizi, and K. H. Mertins, “Multi-step spray modelling of a flat fan atomizer,” *Comput. Electron. Agric.*, vol. 144, no. October 2017, pp. 58–70, 2018.
- [29] J. Xiao, Y. Li, O. A. George, Z. Li, S. Yang, M. W. Woo, W. D. Wu, and X. D. Chen, “Numerical investigation of droplet pre-dispersion in a monodisperse droplet spray dryer,” *Particuology*, vol. 38, pp. 44–60, 2018.
- [30] A. Kastengren, J. Ilavsky, J. P. Viera, R. Payri, D. J. Duke, A. Swantek, F. Z.

- Tilocco, N. Sovis, and C. F. Powell, "Measurements of droplet size in shear-driven atomization using ultra-small angle x-ray scattering," *Int. J. Multiph. Flow*, vol. 92, pp. 131–139, 2017.
- [31] S. J. Jordan, N. L. Ryder, J. Repcik, and A. W. Marshall, "Spatially-resolved spray measurements and their implications," *Fire Saf. J.*, vol. 91, no. May, pp. 723–729, 2017.
- [32] G. M. Magnotti and C. L. Genzale, "Detailed assessment of diesel spray atomization models using visible and X-ray extinction measurements," *Int. J. Multiph. Flow*, vol. 97, pp. 33–45, 2017.
- [33] A. V. Azarov, N. S. Zhukova, and F. G. Antonov, "Water-spray systems reducing negative effects of fine-dispersion dust at operator's workplaces of machine-building industries," *Procedia Eng.*, vol. 206, pp. 1407–1414, 2017.
- [34] Y. Ru, L. Zhao, L. J. S. Hadlocon, H. Zhu, and S. K. Ramdon, "Laboratory evaluation of electrostatic spray wet scrubber to control particulate matter emissions from poultry facilities," *Environ. Technol. (United Kingdom)*, vol. 38, no. 1, pp. 23–33, 2017.
- [35] G. J. Griffin, Q. Xu, C. M. L. Preston, A. D. Bicknell, G. P. Bradbury, and N. White, "Fire behavior and mist suppression of a room lined with glass reinforced polymer (GRP) panels," *Procedia Eng.*, vol. 62, pp. 954–962, 2013.
- [36] G. LeFort, A. W. Marshall, and M. Pabon, "Evaluation of surfactant enhanced water mist performance," *Fire Technol.*, vol. 45, no. 3, pp. 341–354, 2009.
- [37] J. A. S. Bonds, "Ultra-low-volume space sprays in mosquito control: A critical review," *Med. Vet. Entomol.*, vol. 26, no. 2, pp. 121–130, 2012.
- [38] F. H. Arthur, J. F. Campbell, D. L. Brabec, G. R. Ducatte, and J. E. Donaldson, "Aerosol insecticide distribution inside a flour mill: Assessment using droplet measurements and bioassays," *J. Stored Prod. Res.*, vol. 77, pp. 26–33, 2018.
- [39] W. C. Qin, B. J. Qiu, X. Y. Xue, C. Chen, Z. F. Xu, and Q. Q. Zhou, "Droplet

- deposition and control effect of insecticides sprayed with an unmanned aerial vehicle against plant hoppers," *Crop Prot.*, vol. 85, pp. 79–88, 2016.
- [40] D. J. Rasbash and Z. W. Rogowski, "Extinction of fires in liquids by cooling with water sprays," *Combust. Flame*, vol. 1, no. 4, pp. 453–466, 1957.
- [41] T. W. Davies and M. K. Jackson, "A procedure for the design of nozzles used for the production of turbulent liquid jets," *Int. J. Heat Fluid Flow*, vol. 6, no. 4, pp. 298–305, 1985.
- [42] P. T. Lacava, D. Bastos-netto, and A. P. Pimenta, "Design procedure and experimental evaluation of pressure-swirl atomizers DESIGN PROCEDURE AND EXPERIMENTAL EVALUATION OF PRESSURE-SWIRL ATOMIZERS," *24th Int. Congr. Aeronaut. Sci.*, no. JANUARY 2004, pp. 1–9, 2004.
- [43] J. S. Chin and a. H. Lefebvre, "A Design Procedure for Effervescent Atomizers," *J. Eng. Gas Turbines Power*, vol. 117, no. 2, p. 266, 1995.
- [44] A. M. Sipatov, S. A. Karabasov, L. Y. Gomzikov, T. V Abramchuk, and G. N. Semakov, "Structural Optimization of the Air-Blast Atomizer Based on Three-Dimensional Simulation Techniques," vol. 57, no. 1, pp. 75–83, 2014.
- [45] M. Volz, L. Nittel, P. Habisreuther, and N. Zarzalis, "Numerical Study of Liquid Film Characteristics at Varying Operating Conditions in Prefilmer Airblast Atomizer," *Chemie-Ingenieur-Technik*, vol. 88, no. 1–2, pp. 192–199, 2016.
- [46] E. Dongmo, A. Killinger, M. Wenzelburger, and R. Gadow, "Numerical approach and optimization of the combustion and gas dynamics in High Velocity Suspension Flame Spraying (HVSFS)," *Surf. Coatings Technol.*, vol. 203, no. 15, pp. 2139–2145, 2009.
- [47] B. E. Launder and D. B. Spalding, "Lectures in Mathematical Modeling of Turbulence," *Acad. Press. London Engl.*, 1972.
- [48] V. Yakhot and S. A. Orszag, "Renormalization group analysis of turbulence. I. Basic theory," *J. Sci. Comput.*, vol. 1, no. 1, pp. 3–51, 1986.

- [49] T. H. Shih, W. W. Liou, A. Shabbir, Z. Yang, and J. Zhu, "A new k- ϵ eddy viscosity model for high reynolds number turbulent flows," *Comput. Fluids*, vol. 24, no. 3, pp. 227–238, 1995.
- [50] D. C. Wilcox, *Turbulence modeling for CFD*. DCW Industries, Incorporated, 1993.
- [51] F. R. Menter, "Two-equation eddy-viscosity turbulence models for engineering applications," *AIAA J.*, vol. 32, no. 8, pp. 1598–1605, 1994.
- [52] F. Chen and H. Hagen, "A Survey of Interface Tracking Methods in Multi-phase Fluid Visualization," *Vis. Large Unstructured Data Sets - Appl. Geospatial Planning, Model. Eng. (IRTG 1131 Work.)*, pp. 11–19, 2010.
- [53] G. Tryggvason, B. Bunner, A. Esmaeeli, D. Juric, N. Al-Rawahi, W. Tauber, J. Han, S. Nas, and Y. J. Jan, "A Front-Tracking Method for the Computations of Multiphase Flow," *J. Comput. Phys.*, vol. 169, no. 2, pp. 708–759, 2001.
- [54] C. W. Hirt and B. D. Nichols, "Volume of fluid (VOF) method for the dynamics of free boundaries," *J. Comput. Phys.*, vol. 39, no. 1, pp. 201–225, 1981.
- [55] J. Glimm, J. W. Grove, X. L. Li, K. Shyue, Y. Zeng, and Q. Zhang, "Three-Dimensional Front Tracking," *SIAM J. Sci. Comput.*, vol. 19, no. 3, pp. 703–727, 1998.
- [56] F. H. Harlow and J. E. Welch, "Numerical calculation of time-dependent viscous incompressible flow of fluid with free surface," *Phys. Fluids*, vol. 8, no. 12, pp. 2182–2189, 1965.
- [57] N. Ashgriz and J. Y. Poo, "FLAIR: Flux line-segment model for advection and interface reconstruction," *J. Comput. Phys.*, vol. 93, no. 2, pp. 449–468, 1991.
- [58] D. M. Anderson, G. B. McFadden, and A. A. Wheeler, "DIFFUSE-INTERFACE METHODS IN FLUID MECHANICS," *Annu. Rev. Fluid Mech.*, vol. 30, no. 1, pp. 139–165, 1998.
- [59] M. Francois and W. Shyy, "Computations Of Drop Dynamics With The

- Immersed Boundary Method, Part 1: Numerical Algorithm And Buoyancy-Induced Effect," *Numer. Heat Transf. Part B Fundam.*, vol. 44, no. 2, pp. 101–118, 2003.
- [60] H. S. Udaykumar, R. Mittal, and W. Shyy, "Computation of Solid-Liquid Phase Fronts in the Sharp Interface Limit on Fixed Grids," *J. Comput. Phys.*, vol. 153, no. 2, pp. 535–574, 1999.
- [61] L. Lee and R. J. LeVeque, "An Immersed Interface Method for Incompressible Navier--Stokes Equations," *SIAM J. Sci. Comput.*, vol. 25, no. 3, pp. 832–856, 2003.
- [62] G. I. Taylor, "The Shape and Acceleration of a Drop in a High Speed Air Stream," in *The Scientific Papers of G. I. Taylor*, ed. G. K. Batchelor, University Press Cambridge, vol. 3, Cambridge University Press, 1963, pp. 457–464.
- [63] P. J. O'Rourke and A. A. Amsden, "The Tab Method for Numerical Calculation of Spray Droplet Breakup," *SAE Tech. Pap. Ser.*, vol. 1, 2010.
- [64] D. Reitz, "Modeling Atomization Processes in High-Pressure Vaporizing Sprays," *At. Spray Technol.*, vol. 3, pp. 309–337, 1987.
- [65] A. B. Liu, D. Mather, and R. D. Reitz, "Modeling the Effects of Drop Drag and Breakup on Fuel Sprays," *SAE Tech. Pap. Ser.*, vol. 1, 2010.
- [66] M. A. Patterson and R. D. Reitz, "Modeling the Effects of Fuel Spray Characteristics on Diesel Engine Combustion and Emission," in *SAE Technical Paper Series*, 2010, vol. 1.
- [67] R. D. Reitz and J. C. Beale, "Modeling Spray Atomization With the Kelvin-Helmholtz/Rayleigh-Taylor Hybrid Model," *At. Sprays*, vol. 9, no. 6, pp. 623–650, 2014.
- [68] V. G. Levich, *Physicochemical hydrodynamics*. Englewood Cliffs, N.J.: Prentice-Hall, 1962.
- [69] S. V. Apte, M. Gorokhovski, and P. Moin, "LES of atomizing spray with

- stochastic modeling of secondary breakup," *Int. J. Multiph. Flow*, vol. 29, no. 9, pp. 1503–1522, 2003.
- [70] O. P. J, "Collective Drop Effects on Vaporizing Liquid Sprays," 1981.
- [71] D. R. Guildenbecher and P. E. Sojka, "Secondary Breakup of Electrically Charged Newtonian Drops," pp. 807–812, 2009.
- [72] A. Vallet and A. Belhadef, "Atomization modelling: A eulerian approach," *Acta Horti.*, vol. 1008, pp. 45–50, 2013.
- [73] H. S. Aly, Y. A. Eldrainy, K. M. Saqr, T. M. Lazim, and M. N. M. Jaafar, "A mathematical model for predicting spray atomization characteristics in an Eulerian-Eulerian framework," *Int. Commun. Heat Mass Transf.*, vol. 37, no. 6, pp. 618–623, 2010.
- [74] G. Anirban, R. M. Barron, and R. Balachandar, "Numerical simulation of high-speed turbulent water jets in air," *J. Hydraul. Res.*, vol. 48, no. 1 EXTRA ISSUE, pp. 119–124, 2010.
- [75] M. Maly, J. Jedelsky, J. Slama, L. Janackova, M. Sapik, G. Wigley, and M. Jicha, "Internal flow and air core dynamics in Simplex and Spill-return pressure-swirl atomizers," *Int. J. Heat Mass Transf.*, vol. 123, pp. 805–814, 2018.
- [76] Y. Sun, A. M. Alkhedhair, Z. Guan, and K. Hooman, "Numerical and experimental study on the spray characteristics of full-cone pressure swirl atomizers," *Energy*, vol. 160, pp. 678–692, 2018.
- [77] F. J. Salvador, S. Ruiz, M. Crialesi-Esposito, and I. Blanquer, "Analysis on the effects of turbulent inflow conditions on spray primary atomization in the near-field by direct numerical simulation," *Int. J. Multiph. Flow*, vol. 102, pp. 49–63, 2018.
- [78] D. J. Jiang, H. F. Liu, W. F. Li, J. L. Xu, F. C. Wang, and X. Gong, "Modeling atomization of a round water jet by a high-speed annular air jet based on the self-similarity of droplet breakup," *Chem. Eng. Res. Des.*, vol. 90, no. 2, pp.

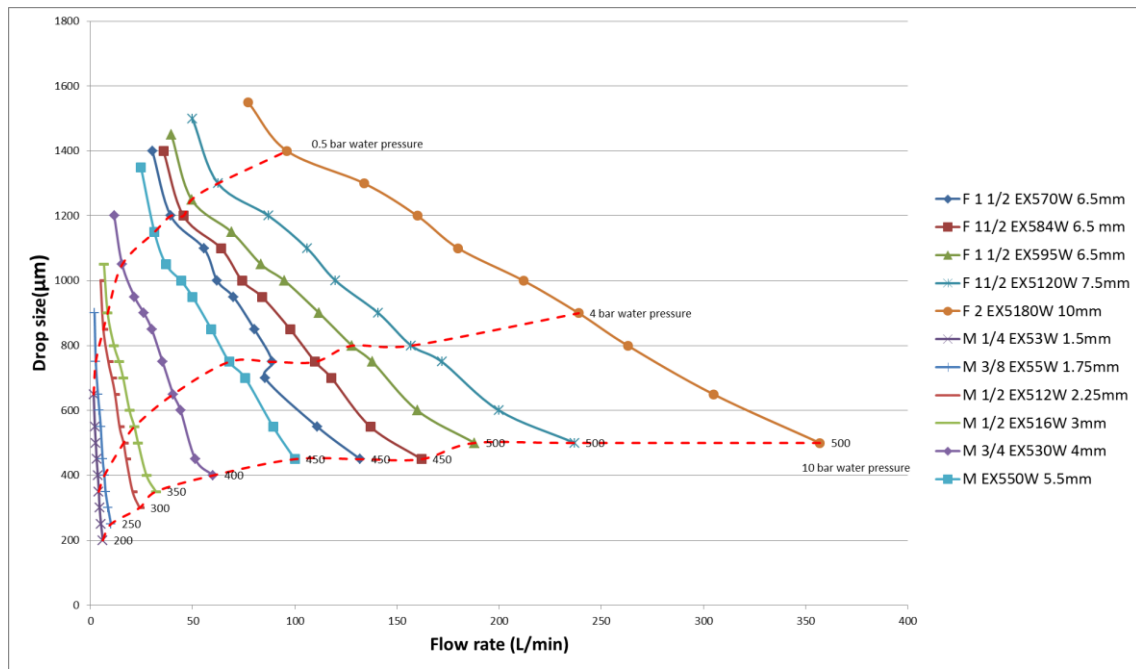
- 185–192, 2012.
- [79] Liu Huolong, “Modeling and Control of Batch Pulsed Top-spray Fluidized bed Granulation,” 2014.
- [80] W. Duangkhamchan, F. Ronsse, F. Depypere, K. Dewettinck, and J. G. Pieters, “CFD study of droplet atomisation using a binary nozzle in fluidised bed coating,” *Chem. Eng. Sci.*, vol. 68, no. 1, pp. 555–566, 2012.
- [81] P. Vittoria, “Designated Extension States,” vol. 1, no. 19, pp. 1–8, 2009.
- [82] Y. Fan, N. Hashimoto, H. Nishida, and Y. Ozawa, “Spray characterization of an air-assist pressure-swirl atomizer injecting high-viscosity Jatropha oils,” *Fuel*, vol. 121, pp. 271–283, Apr. 2014.
- [83] C. M. Varga, “United States,” no. 19, 2011.
- [84] Apple Rubber, “SEAL DESIGN GUIDE: <http://www.applerubber.com/>,” pp. 1–115, 2017.

Appendix

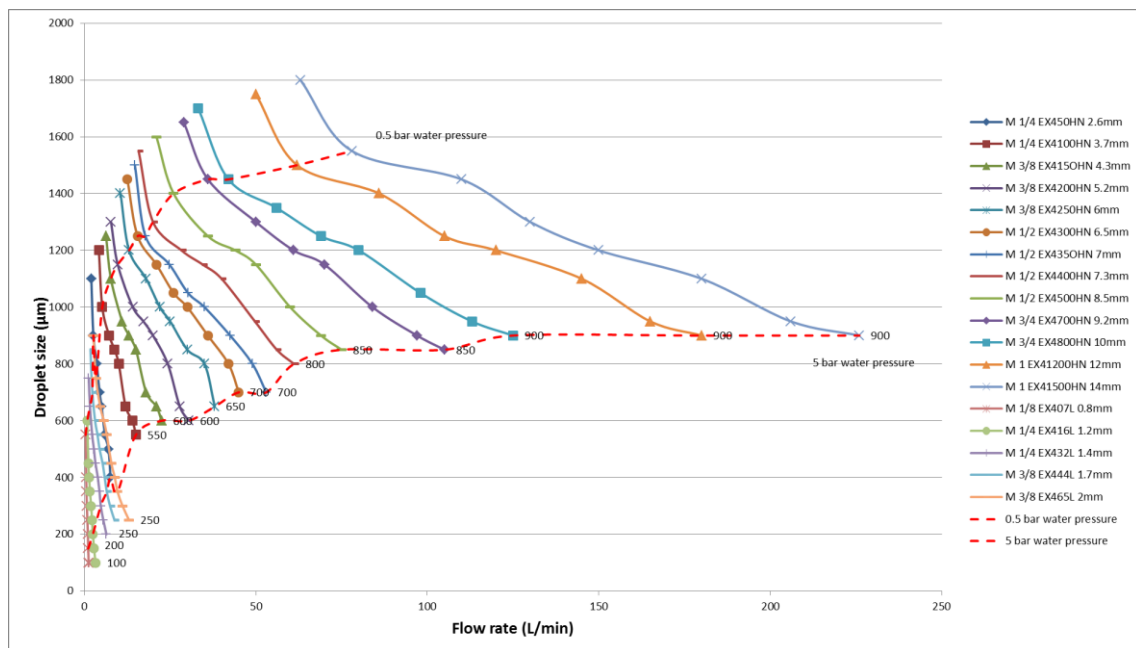
Appendix A - Additional Results from Product Review

Manufacturer	Product	Nozzle Characteristics						Design features
		Nozzle type	Droplet size range	Flow rate (l/h)	Spray angle	Spray Pattern		
BETE	Xaad	Twin-fluid nozzle	<145µm	1.7-93	70°	Hollow cone	Internal mix	
	Xapr	Twin-fluid nozzle	<145µm	250	12°-22°	Full cone	Internal mix	
	Xasr	Twin-fluid nozzle	<145µm	44	12°-22°	Full cone	Internal mix, lowest flow rate	
	Xaer	Twin-fluid nozzle	<145µm	234	10°-230°	full cone	external mix, variable atomization, allows spraying of viscous liquids	
	Xaxw	Twin-fluid nozzle	<145µm	48	180°	Hollow cone	Internal mix	
	Sa	Twin-fluid swirl nozzle	<145µm	80	20°-90°		Internal mix, effeucobt design reduces compressed air consumption	
							external mix, separate atomizing and fan air lines, variable coverage and fine control of drop size without affecting liquid flow rates	
	SAM	twin-fluid		174				
	Spraying System Co.	1/8j and 1/4j with round spray air caps	twin-fluid	10-100µm	1.4-250	12°-22°	Full cone	Internal mix
		1/8j and 1/4j with wide angle round spray air caps	twin-fluid	10-100µm	1.7-93		Hollow cone	Internal mix
1/8j with round spray air caps		twin-fluid	10-100µm	1.4-88	12°-21°	Full cone	Internal mix	
1/8j with wide angle round air caps		twin-fluid	10-100µm	1.7-74		Hollow cone	Internal mix	
1/2j with wide angle round air caps		twin-fluid	10-100µm	32-840		hollow cone	Internal mix	
1/2j with round air caps		twin-fluid	10-100µm	15.5-840		hollow cone	Internal mix	
Jj with wide angle round air caps		twin-fluid	10-100µm	6.4-33 l/min		Hollow cone	Internal mix	
Jj with round air caps		twin-fluid	10-100µm	6.4-65 l/min		Hollow cone	Internal mix	
				less than 15µm				
23412/ OJ25655		fogger spray nozzle		4.2-30			drops average fifteen microns in size and less	
HIKUCHI & CO.,LTD	03C	humidifier	7.5µm, maximi	5.2-14.4				
Lecther	136.1/166.1	twin-fluid nozzle (Pneumatic)		1.5-172.70	20°	full cone	Internal mix	
	136.2/166.2	twin-fluid nozzle (Pneumatic)		1.8-80.70	60°	full cone	Internal mix	
		twin-fluid nozzle (Pneumatic)		8.5-290 l/min	15°	full cone	Internal mix	
		170 (Pneumatic)						
		twin-fluid nozzle (Pneumatic)		0.15-63 l/min	20°-30°	full cone	external mix	

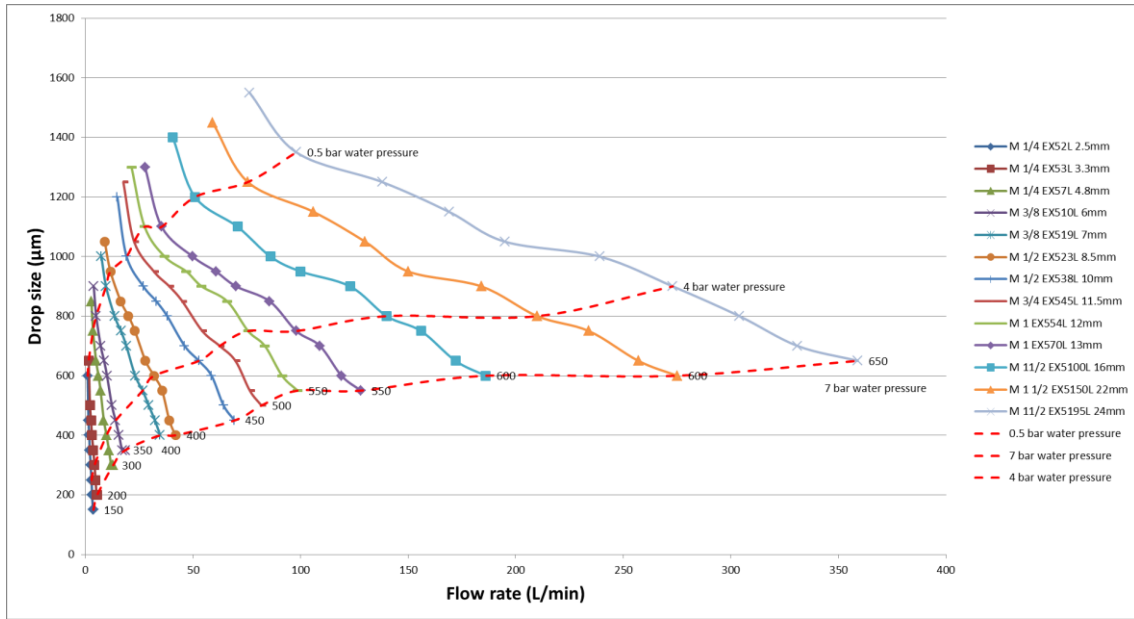
Appendix A.1 Nozzle data collected from manufacture's websites



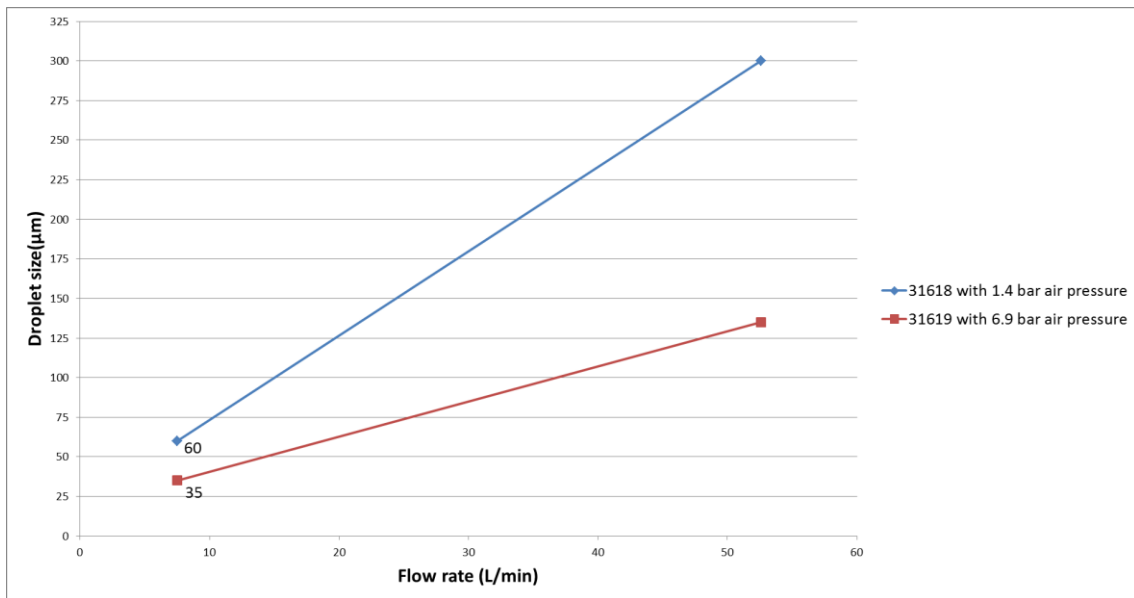
Appendix A.2 Mean droplet sizes produced by single fluid axial hollow cone nozzle with different flow rates



Appendix A.3 Mean droplet sizes produced by single fluid tangential full cone nozzle with different flow rates



Appendix A.4 Mean droplet sizes produced by single fluid tangential hollow cone nozzle with different flow rates



Appendix A.5 Mean droplet sizes produced by twin fluid hollow cone nozzle with different flow rates

Appendix B - Experimental Data for Particle Distribution

Pressure	Experiment Number	Volume Displayed in Sample (m ³ /s)	Sample Duration (s)	Total Volume Collected (m ³)	Number of Droplets in Absorbed Volume						Number of Droplets in 1 m ³					
					0.0-0.3 μm	0.3-0.5 μm	0.5-1.0 μm	1.0-2.5 μm	2.5-5.0 μm	5.0-10.0 μm	0.0-0.3 μm	0.3-0.5 μm	0.5-1.0 μm	1.0-2.5 μm	2.5-5.0 μm	5.0-10.0 μm
5 bar water pressure & 6 bar air pressure	1	0.0004795	10.035	0.00481177	14225	12530	8853	11077	357070	109903	1417.53861	1248.6298	882.212257	1103.83657	35582.4614	10951.9681
	2	0.0004795	10.169	0.00487602	13974	12350	9124	13976	359748	102739	1374.17642	1214.47537	897.2367	1374.37309	35376.9299	10103.1567
	3	0.0004795	10.205	0.00489328	14257	12544	9355	13401	358041	111835	1397.06026	1229.20137	914.747673	1313.17981	35084.8604	10958.8437
	4	0.0004795	10.036	0.00481225	12180	10732	7797	10730	330021	110885	1213.63093	1069.35034	776.903149	1069.15106	32883.7186	11048.7246
	5	0.0004795	10.172	0.00487746	11679	10502	7627	19174	330010	101075	1148.15179	1032.442	749.803382	1884.97837	32442.9807	9936.59064
	6	0.0004795	10.208	0.00489472	11302	10024	7755	30038	327702	85999	1107.17085	981.974922	759.698276	2942.59404	32102.4687	8424.66693
	7	0.0004795	10.135	0.00485972	11221	10107	7517	21380	325755	94687	1107.15343	997.237296	741.687222	2109.52146	32141.5886	9342.57523
	8	0.0004795	10.171	0.00487698	10194	9181	7228	39434	304762	83285	1002.26133	902.664438	710.647921	3877.10156	29963.8187	8188.47704
	9	0.0004795	10.205	0.00489328	9641	8523	6946	47950	288470	81622	944.732974	835.178834	680.646742	4698.67712	28267.5159	7998.23616
	10	0.0004795	10.037	0.00481273	8450	7506	6396	66534	257743	66486	841.885025	747.833018	637.242204	6628.87317	25679.2866	6624.09086
	11	0.0004795	10.025	0.00480697	9882	8688	6902	44723	289097	81368	985.735661	866.633416	688.478803	4461.14713	28837.606	8116.50873
	12	0.0004795	10.116	0.0048717	9534	8539	7346	74541	277025	58861	938.385827	840.452756	723.031496	7336.7126	27266.2402	5793.40551
3 bar water pressure & 8 bar air pressure	1	0.0004795	10.123	0.00485396	10844	10372	8988	74436	313117	54263	1071.22395	1024.59745	887.879087	7353.15618	30931.2457	5360.36748
	2	0.0004795	10.058	0.0048228	10719	9967	8741	69602	310673	51737	1065.71883	990.952476	869.059455	6920.06363	30888.1487	5143.86558
	3	0.0004795	10.094	0.00484006	27441	18443	30221	129734	158570	22326	2718.54567	1827.12502	2993.95681	12852.5857	15709.3323	2211.809
	4	0.0004795	10.131	0.0048578	34946	23507	35006	129246	171535	21330	3449.41269	2320.30402	3455.33511	12757.4771	16931.6948	2105.41901
	5	0.0004795	10.065	0.00482615	24297	20678	29606	139343	203983	20496	2414.00894	2054.4461	2941.48038	13844.312	20266.5673	2036.36364
	6	0.0004795	10.101	0.00484341	19828	9400	12765	121734	196731	21721	1962.97396	930.600931	1263.73626	12051.6781	19476.3885	2150.38115
	7	0.0004795	10.138	0.00486116	9806	10260	10716	123922	263306	29913	967.251923	1012.03393	1057.01322	12223.5155	25972.1839	2950.58197
	8	0.0004795	10.174	0.00487842	8942	9569	10713	138023	238037	20448	878.907018	940.534696	1052.97818	13566.2473	23396.5992	2009.82898
	9	0.0004795	10.109	0.00484725	9721	10550	12425	144356	244168	17499	961.61836	1043.62449	1229.10278	14279.9486	24153.5266	1731.03175
	10	0.0004795	10.145	0.00486451	13829	16017	27510	148770	215163	13551	1363.13455	1578.80729	2711.68063	14664.3667	12108.7728	1335.73189
	11	0.0004795	10.181	0.00488177	17720	19144	35203	155521	189285	8902	1740.497	1880.36539	3457.71535	15275.6114	18591.9851	874.373834
	12	0.0004795	10.116	0.00485061	12978	16790	30050	159845	201189	6312	1282.91815	1659.74694	2970.54172	15801.206	19888.1969	623.96204

Pressure	Experiment Number	Volume Displayed in Sample (m ³ /s)	Sample Duration (s)	Total Volume Collected (m ³)	Number of Droplets in Absorbed Volume					Number of Droplets in 1 m ³						
					0.0-0.3 μm	0.3-0.5 μm	0.5-1.0 μm	1.0-2.5 μm	2.5-5.0 μm	5.0-10.0 μm	0.0-0.3 μm	0.3-0.5 μm	0.5-1.0 μm	1.0-2.5 μm	2.5-5.0 μm	5.0-10.0 μm
4 bar water pressure & 10 bar air pressure	1	0.0004795	10.17	0.0048765	24965	21766	16010	19485	443509	114972	2454.76893	2140.21632	1574.23795	1915.9292	43609.5379	11305.0147
	2	0.0004795	10.206	0.00489376	21523	19135	14766	18475	450703	86096	2108.85753	1874.87752	1446.796	1810.20968	44160.5918	8435.82207
	3	0.0004795	10.135	0.00485972	22598	19971	15668	20974	472223	63962	2229.69906	1970.49827	1545.92995	2069.46226	46593.2906	6311.00148
	4	0.0004795	10.122	0.00485348	21453	18908	15467	21869	466737	61680	2119.4428	1868.01027	1528.0577	2160.54139	46111.144	6093.65738
	5	0.0004795	10.156	0.00486979	20036	17927	14907	24884	468506	43860	1972.82395	1765.16345	1467.80228	2450.17724	46130.9571	4318.62938
	6	0.0004795	10.092	0.0048391	21571	19468	15929	26377	465899	54692	2137.43559	1929.05272	1578.37891	2613.65438	46165.1803	5419.34205
	7	0.0004795	10.129	0.00485684	21688	19290	16157	26921	471771	50356	2141.17879	1904.43282	1595.12291	2657.8142	46576.2662	4971.46806
	8	0.0004795	10.166	0.00487458	17059	15459	12678	30221	433897	46234	1678.04446	1520.65709	1247.09817	2972.75231	42681.1922	4547.90478
	9	0.0004795	10.093	0.00483958	8625	8252	8643	127072	246721	19369	998.420377	968.703722	982.03179	12868.2989	26822.3912	2040.97147
	10	0.0004795	10.129	0.00485684	10113	9812	9947	130343	271684	20673	998.420377	968.703722	982.03179	12868.2989	26822.3912	2040.97147
	11	0.0004795	10.063	0.00482519	14612	14675	21067	130469	214884	19198	1452.05207	1458.31263	2093.51088	12965.2191	21353.8706	1907.78098
	12	0.0004795	10.195	0.00488849	21863	14494	15693	111777	238795	18216	2144.48229	1421.67729	1539.28396	10963.9039	23422.7563	1786.75821
10 bar water pressure & 10 bar air pressure	1	0.0004795	10.17	0.0048765	23416	20066	13849	16371	421846	125491	2302.45821	1973.05801	1361.75025	1609.73451	41479.4494	12339.3314
	2	0.0004795	10.206	0.00489376	22724	19894	15109	19021	447886	92170	2226.53341	1949.24554	1480.40368	1863.70762	43884.5777	9030.96218
	3	0.0004795	10.035	0.00481177	23228	20266	15079	18867	435925	100147	2314.69856	2019.53164	1502.64076	1880.11958	43440.4584	9979.7708
	4	0.0004795	10.172	0.00487746	20663	18153	13312	16810	450164	76289	2031.3606	1784.6048	1308.69052	1652.5757	44255.2104	7499.90169
	5	0.0004795	10.209	0.0048952	20486	18053	14540	21620	456242	61578	2006.66079	1768.34166	1424.23352	2117.73925	44690.1753	6031.7367
	6	0.0004795	10.134	0.00485924	20400	18180	14480	22970	456420	58161	2013.02546	1793.96092	1428.85336	2266.6272	45038.4843	5739.19479
	7	0.0004795	10.17	0.0048765	19071	16865	12867	17634	444816	65659	1875.22124	1658.30875	1265.19174	1733.9233	43738.0531	6456.14553
	8	0.0004795	10.207	0.00489424	19112	16751	13125	20673	441013	65765	1872.44048	1641.12864	1285.88224	2025.37474	43206.9168	6443.12727
	9	0.0004795	10.134	0.00485924	16623	14510	12487	36317	429214	35117	1640.31972	1431.8137	1232.18867	3583.67871	42353.8583	3465.26544
	10	0.0004795	10.171	0.00487698	15968	13930	11268	24736	408457	61917	1569.95379	1369.58018	1107.85567	2432.01258	40158.9814	6087.60201
	11	0.0004795	10.159	0.00487123	14030	12906	11375	63996	385058	27060	1381.04144	1270.40063	1119.69682	6299.43892	37903.1401	2663.648
	12	0.0004795	10.091	0.00483862	13071	11771	10426	67793	368488	25202	1295.31265	1166.48499	1033.1979	6718.1647	36516.4999	2497.473

Pressure	Experiment Number	Volume Displayed	Sample Duration (s)	Total Volume	Number of Droplets in Absorbed Volume						Number of Droplets in 1 m³					
					0.0-0.3 µm	0.3-0.5 µm	0.5-1.0 µm	1.0-2.5 µm	2.5-5.0 µm	5.0-10.0 µm	0.0-0.3 µm	0.3-0.5 µm	0.5-1.0 µm	1.0-2.5 µm	2.5-5.0 µm	5.0-10.0 µm
6 bar water pressure & 12 bar air pressure	1	0.0004795	10.094	0.00484006	32046	27706	16749	18539	340302	264917	3174.75728	2744.79889	1659.30256	1836.63563	33713.295	26244.997
	2	0.0004795	10.13	0.00485732	28828	24823	14718	16246	342633	249872	2845.80454	2450.44423	1452.91214	1603.75123	33823.5933	24666.535
	3	0.0004795	10.168	0.00487554	31465	26872	17493	19730	391134	210167	3094.5122	2642.80094	1720.39732	1940.40126	38467.1518	20669.4532
	4	0.0004795	10.094	0.00484006	27585	24294	16711	19919	439419	139782	2732.81157	2406.7763	1655.53794	1973.35051	43532.6927	13848.0285
	5	0.0004795	10.13	0.00485732	29527	25756	17468	20586	434865	154972	2914.8075	2542.54689	1724.38302	2032.18164	42928.4304	15298.3218
	6	0.0004795	10.165	0.0048741	26471	23367	16936	21109	459065	111241	2604.13182	2298.77029	1666.1092	2076.63551	45161.3379	10943.5317
	7	0.0004795	10.094	0.00484006	21147	18745	14375	19172	444392	84306	2095.00693	1857.04379	1423.9152	1899.34615	44025.3616	8352.09035
	8	0.0004795	10.13	0.00485732	15884	15135	12768	53550	404071	43672	1568.01579	1494.077	1260.41461	5286.27838	39888.5489	4311.15499
	9	0.0004795	10.167	0.00487506	14018	17814	20644	148244	258681	19090	1378.77447	1752.13927	2030.4908	14580.899	25443.1986	1877.64336
	10	0.0004795	10.094	0.00484006	18890	26722	34554	160543	230293	14977	1871.40876	2647.31524	3423.22172	15904.7949	22814.8405	1483.75272
	11	0.0004795	10.13	0.00485732	12785	14483	15754	138463	289487	17575	1262.09279	1429.71372	1555.18263	13668.6081	28577.1964	1734.94571
	12	0.0004795	10.164	0.00487362	19114	26926	31868	159079	236595	12274	1880.55884	2649.15388	3135.37977	15651.22	23277.745	1207.59543
14 bar water pressure & 14 bar air pressure	1	0.0004795	10.18	0.00488129	28442	24801	16337	18610	411896	175676	2793.90963	2436.24754	1604.81336	1828.0943	40461.2967	17256.9745
	2	0.0004795	10.108	0.00484677	27897	24215	16340	19322	437030	140346	2759.89315	2395.62723	1616.54135	1911.5552	43236.0507	13884.6458
	3	0.0004795	10.145	0.00486451	25163	22376	15587	19382	457452	105026	2480.33514	2205.61853	1536.42188	1910.49778	45091.3751	10352.4889
	4	0.0004795	10.182	0.00488225	19942	17816	14015	20690	447597	70867	1958.55431	1749.75447	1376.44863	2032.01729	43959.6346	6960.0275
	5	0.0004795	10.108	0.00484677	18858	16802	12787	19731	440028	67087	1865.65097	1662.24772	1265.03759	1952.0182	43532.6474	6637.02018
	6	0.0004795	10.144	0.00486403	16116	14742	13073	55717	405504	39093	1588.7224	1453.27287	1288.74211	5492.60647	39974.7634	3853.80521
	7	0.0004795	10.179	0.00488082	15456	14610	13276	75795	398096	26086	1518.42028	1435.30799	1304.25386	7446.21279	39109.5392	2562.72718
	8	0.0004795	10.109	0.00484725	13458	13132	12252	98724	353771	25056	1331.28895	1299.04046	1211.98932	9765.95113	34995.6474	2478.58344
	9	0.0004795	10.146	0.00486499	15463	14383	13000	72075	387731	33904	1524.04889	1417.603	1281.29312	7103.78474	38215.1587	3341.61246
	10	0.0004795	10.182	0.00488225	13099	12498	11435	93730	348288	28138	1286.48596	1227.46022	1123.0603	9205.46062	34206.2463	2763.50422
	11	0.0004795	10.117	0.00485109	11315	10675	9957	101945	314789	25058	1118.41455	1055.15469	984.185035	10076.6037	31114.8562	2476.82119
	12	0.0004795	10.154	0.00486883	10657	10480	10109	111046	303019	21689	1049.53713	1032.10557	995.568249	10936.1828	29842.3281	2136.00552